VIRUS-LIKE PARTICLE QB AS IMMUNOGENIC CARRIER FOR ANTIVIRIAL AND
ANTIBACTERIAL VACCINES

By

Zibin Tan

A DISSERTATION

Submitted to
Michigan State University
in partial fulfillment of the requirements
for the degree of

Chemistry—Doctor of Philosophy

2024

ABSTRACT

Virus-like particles (VLPs) are sophisticated multiprotein complexes that emulate the structural organization and conformation of authentic viruses but lack the ability to infect or replicate within host cells. VLPs inherit many immunogenic characteristics from their native viral counterpart. While replication-competent viral vectors have been utilized as vaccine carriers in both clinical and preclinical contexts, their application is often limited to those vectors capable of infecting vertebrate cells, and often raises safety concerns. VLPs are considered promising alternatives due to their favorable safety profile, the diverse array of viral strains available for exploitation and the enhanced flexibility for engineering. Qβ VLP is derived from *Escherichia coli* phage Qβ and its structure and immunogenicity have been extensively characterized. The versatility of the platform enables a broad scope of antigens, including peptides, proteins and carbohydrates. It also allows rational design and optimization of the antigen structure loaded on the carrier.

In the first chapter of this thesis, recent advances of viral vectored vaccines in cancer immunotherapy are reviewed. In the second and third chapters of this thesis mutant Qβ (mQβ) VLPs are used as vaccine carriers against some emerging human pathogens: SARS-CoV-2 and antibiotic resistant *Staphylococcus Aureus*. To develop a broad and long lasting COVID vaccine, SARS-CoV-2 Spike protein receptor binding domain (RBD) based epitopes are investigated as conjugates with mQβ. The epitope design is critical to eliciting potent antibody responses with the

full length RBD being superior to peptide and glycopeptide antigens. The full length RBD conjugated with mQβ activates both humoral and cellular immune systems *in vivo*, inducing broad spectrum, persistent and comprehensive immune responses effective against multiple variants of concerns including Delta and Omicron, rendering it a promising vaccine candidate. For *S. Aureus* vaccine development, oligosaccharides derived from poly-β-(1−6)-*N*-acetylglucosamine (PNAG), a polysaccharide expressed on the surface of numerous pathogens, are used for antigen design. A significant challenge in the development of a PNAG-based vaccine lies in the incomplete understanding of the influence of the number and positional arrangement of free amines versus N-acetylation on the antigenicity of PNAG. A divergent strategy is developed to synthesize a comprehensive library of 32 PNAG pentasaccharides. This library enables the identification of PNAG sequences with specific patterns of free amines as epitopes for vaccines against *S. aureus*. Active vaccination with the conjugate of discovered PNAG epitopes with mQβ as well as passive vaccination with diluted rabbit antisera provides mice with near complete protection against infections by *S. aureus* including methicillin-resistant *S. aureus* (MRSA). In conclusion, mQβ is a promising platform for next generation vaccine design due to its flexibility to present diverse antigens and its capacity to augment both humoral and cellular immunity.

TABLE OF CONTENTS

LIST OF ABBREVIATIONS

ABCA1/G1   ATP-binding cassette transporter A1/G1

Ac   Acetyl

ADCC   Antibody-dependent cellular cytotoxicity

AEC   3-Amino-9-ethylcarbazole

AKT   Protein kinase B

Alloc   Allyloxycarbonyl

ApoA1   Apolipoprotein AI

ARDS   Acute respiratory distress syndrome

ASV   Amplicon sequence variants

ATP   Adenosine triphosphate

BALF   Bronchoalveolar lavage fluid

Boc   tert-Butyloxycarbonyl

BSA   Bovine serum albumin

Bz   Benzoyl

CAR-T   Chimeric antigen receptor T cell

CCID   Cell culture infective doses

CCL   C-C motif ligand

CCR   C-C chemokine receptor

CD40L	CD40 ligand
CDC	Center for disease control and prevention
cDC1s	Conventional type 1 DCs
CFA	Complete Freund's Adjuvant
Cfu	Colony forming units
cGAS	Cyclic guanosine monophosphate-adenosine monophosphate adenosine synthetase
COVID-19	Coronavirus disease 2019
Cryo-EM	cryo-Electron microscopy
CP	Capsid protein
CTL	Cytotoxic T lymphocyte
CTLA-4	Cytotoxic T lymphocyte-associated protein 4
DAMPs	Damage associated molecular patterns
DCs	Dendritic cells
DMF	Dimethylformamide
dMMR	DNA mismatch repair-deficient
DLS	Dynamic light scattering
DIPEA	Diisopropylethyl amine
dpp	Days post priming

DTT	Dithiothreitol
EC50	Concentration at half maximum effectiveness
EGFR	Epidermal growth factor receptor
EGFRvIII	Epidermal growth factor receptor variant III
ELISA	Enzyme Linked Immunosorbent Assay
ELISpot	Enzyme-linked immunospot assay
ESCC	Esophageal squamous cell carcinoma
FDA	Food and drug administration
FKBP	FK506 binding protein
Fmoc	Fluorenylmethoxycarbonyl
FRB	FKBP-rapamycin binding protein
FSCs	Fibroblast stromal cells
FSP	Frameshift peptide
Gad	Gorilla Adenovirus
GBM	Glioblastoma
GM-CSF	Granulocyte-macrophage colony-stimulating factor
GMT	Geometrical mean of titer
GPI	Glycosylphosphatidylinositol
$GSDM^{NT}$	N-terminal gasdermin domain

GSDME	Gasdermin E
hACE2	Human angiotensin converting enzyme 2
hAdv	Human adenovirus
HATU	Hexafluorophosphate azabenzotriazole tetramethyl uronium
HCS	Human convalescent sera
hMUC-1	Human mucin-1
HPV	Human papillomavirus
HRP	Horseradish peroxidase
HSV-1	Herpes simplex virus type 1
HVR1	Hypervariable region 1
IACUC	Institutional animal care and use committee
ICB	Immune checkpoint blockade
ICD	Immunogenic cell death
IFA	Incomplete Freund's Adjuvant
IFNγ	Interferon γ
IL-2	Interleukin-2
IL-7	Interleukin-7
IL-12	Interleukin-12
KPB	Potassium phosphate buffer

LCMV	Lymphocytic choriomeningitis virus
LLC	Lewis lung carcinoma
LNPs	Lipid nanoparticles
M199	HEPES buffered Medium 199
mAb	Monoclonal antibody
MALDI-ToF	Matrix-assisted laser desorption/ionization time-of-flight
MEK	Mitogen-activated protein kinase kinase
MHC I	Major histocompatibility complex class I
mIFNβ	Mouse interferon β
MPLA	Monophosphoryl lipid A
mQβ	Mutant bacteriophage Qβ
mRNA	Messenger RNA
miRNA	MicroRNA
MRSA	Methicillin-resistant *S. aureus*
MS	Mass spectrometry
mTOR	mammalian target of rapamycin
MVA	Ankara strain of Vaccinia virus
MWCO	Molecular weight cut off
NDV	Newcastle disease virus

NHAc	*N*-acetamides
NK	Natural killer
NMDS	Non-metric multidimensional scaling
NSCLC	non-small cell lung cancer
NT50	Titer at half maximum neutralization
oHSV	Oncolytic herpes simplex virus type 1
OPK	Opsonophagocytic killing
ORFV	Oncolytic parapoxvirus ovis
PAMAM	Polyamidoamine
PAMPs	Pathogen associated molecular patterns
PBST	PBS pH 7.4 containing 0.5% Tween-20
PD-1	Programmed cell death 1
PD-L1	Programmed cell death ligand 1
PERMANOVA	Permutational multivariate analysis of variance
PI3K	Phosphatidylinositol-4,5-bisphosphate 3-kinase
PLGA	Polylactic Acid-Polyglycolic acid copolymer
PNAG	Poly-β-(1−6)-*N*-acetylglucosamine
pRB	Retinoblastoma protein
PSVs	Pseudovirions

PTEN	Phosphatase and tensin homolog deleted on chromosome 10
rAAVs	Recombinant adeno-associated viruses
RBC	Red blood cell
RBD	Receptor binding domain
RBM	Receptor binding motif
RLU	Relative fluorescence unit
S	Spike glycoprotein
SA	Sinapinic acid
samRNA	Self-amplifying RNA
SARS-CoV-2	Severe acute respiratory syndrome coronavirus 2
S. aureus	*Staphylococcus aureu*
SBAP	Succinimidyl 3-(bromoacetamido)propionate
SEC	Size exclusion chromatography
Siglec-10	Sialic acid binding Ig-like lectin 10
SIRPα	Signal regulatory protein α
S-PSV	SARS-CoV-2 S pseudovirions
STING	Stimulator of interferon genes
sVNT	Surrogate virus neutralization titer assay
TAA	Tumor-associated antigens

TALER	Transcription activation-like effect repression
TAMs	Tumor-associated macrophages
TBDPS	tert-Butyldiphenylsilyl
TCEP	Tris(2-carboxyethyl)phosphine
TCR	T cell receptor
TFA	Trifluoroacetic acid
Tfh	T follicular helper
TILs	Tumor-infiltrating lymphocytes
TLR	Toll-like receptor
TMB	3,3',5,5'-Tetramethylbenzidine
TME	Tumor microenvironment
Troc	2,2,2-Trichloroethoxycarbonyl
TRP2	tyrosinase-related protein 2
TT	Tetanus toxoid
TTHc	TT heavy chain
T-VEC	Talimogene laherparepvec
VEEV	Venezuelan Equine Encephalitis Virus
VLPs	Virus-like particles
VOCs	Variants of concern

VSV   Vesicular stomatitis virus

VSVg   VSV surface glycoprotein

WHO   World Health Organization

Chapter 1   Viral Vectored Cancer Vaccines

1.1   Introduction

Cancer continues to pose a significant challenge to public health care systems worldwide. In the United States alone, over 1.9 million new cancer cases and more than 600,000 cancer-related deaths were projected for the year 2022.[1] Over recent decades, innovative therapeutic approaches such as chimeric antigen receptor T cell (CAR-T) therapy and immune checkpoint blockade (ICB) have made their way into clinical practice, achieving remarkable results in treating certain types of cancer. These therapies leverage the patient's own immune cells, enhancing their efficacy either by modifying their immune receptors to target cancer cells or by blocking the receptors that lead to immune exhaustion, thereby amplifying their anti-tumor activity.

Therapeutic cancer vaccines, designed to induce anti-tumor immunity by utilizing immunogenic agents, have not seen significant progress. The reasons for this are multifaceted: many cancer patients possess an aged immune system that is insufficiently stimulated by immunogens; patients who undergo immunotherapy often have failed to control tumor growth by extensive chemotherapy and/or radiotherapy, which also impair their immune system; the fact that cancer cells originate from normal cells and share many features with them makes it challenging to overcome central tolerance; theoretically, neoantigens that arise with cancer could be recognized by T cell receptors (TCR), but a recent small-scale clinical trial revealed that only half of the pancreatic cancer patients responded to a personalized neoantigen peptide-based cancer vaccine,[2]

indicating the need for improved methods to identify immunogenic neoantigens; moreover, cancer cells can evade the host immune system by creating an immunosuppressive tumor microenvironment (TME) through various mechanisms.[3] These complexities underscore the need for continued research and innovation in this field.

Viral vectors are emerging as promising tools for cancer immunotherapy, capable of surmounting some of the challenges encountered by other methodologies. These vectors offer several advantages: they typically possess an optimal size for *in vivo* antigen trafficking and can carry substantial amounts of antigens; viral particle and viral genome can also travel within the infected cells through the body, enabling the potential to present antigens to the lymph systems far away from the primary site. They can display antigens on their surface in a multivalent manner, and for non-enveloped viruses, in a repeated and symmetrical fashion, thereby enhancing immune recognition. Viral replication can trigger innate immune responses and interferon pathways, for example, viral RNA or DNA produced in the cytosol is usually poorly capped and can be sensed by the innate immune system via receptors like cyclic guanosine monophosphate-adenosine monophosphate adenosine synthetase (cGAS), toll-like receptor 3 (TLR3), etc., triggering downstream proinflammatory signals such as stimulator of interferon genes (STING) and type I interferon (IFN) pathways. Viral replication also hijacks the cell cycles to mobilize molecular machines such as nucleic acid polymerases. Dysregulated nucleic acid synthesis and disturbed cell cycles are common features shared between virus infected cells and tumor cells, thus triggering

similar immune responses. Viral replication can modify the tumor microenvironment, recruit immune cells, resulting in immunogenic cell death (ICD), secretion of pathogen and damage associated molecular patterns (PAMPs and DAMPs), release of tumor associated antigen and enhanced antigen presentation. For instance, rotavirus used as anti-infectious disease vaccine can be repurposed to cancer immunotherapy. The virus readily replicates in mouse tumor models and induces ICD and type I interferon response.[4] Viral vectors can encode tumor-associated antigens and neoantigens. Transcription of viral genome-encoded protein is carried by host ribosomes, which is monitored by the host cell via degradation of poorly folded proteins and presentation of the product peptides to the major histocompatibility complex class I (MHC I) molecules in the ER. This antigen presentation process is crucial for inducing CD8^{+} T lymphocyte responses. Viral encoded antigens synthesized by the host cell carries the post transcriptional modifications native to the host such as glycosylation, which is important to maintain the structural integrity of the antigens. Collectively, these actions foster an inflammatory environment conducive to anti-tumor immunity. Infected cells are often recognized by the host immune system in a manner akin to cancer cells. Furthermore, they can target cancers that are caused by or associated with viral infections, such as human papillomavirus (HPV)-related cancers, by inducing antiviral immune responses that can also attack cancer cells. For instance, in HPV associated head-neck or oropharyngeal cancer, infiltrated viral-specific T and B cells recognize cancer cells;[5-8] in skin carcinoma, HPV antigen-specific T cells can prevent and suppress tumor growth.[9] HPV virus-like

particles (VLPs) have been used as prophylactic vaccines to prevent cervical cancer, but they have not demonstrated therapeutic effects;[10, 11] other types of viral vectored vaccines with potential therapeutic benefits are still under development. Here we summarize some of the key aspects regarding the development of viral vectored cancer vaccines.

Vaccine Name	Source	Clinical Stage	Cancer	Access code	Route	Specific Tumor Antigens?	Combined Therapy	Reference
T-VEC	HSV-1	approved	Unresectable metastatic melanoma IIIB/C-IVM1a		i.t.	None	NA	[12]
G47Delta	HSV-1	approved	Recurrent glioma	UMIN0000002661 UMIN000015995	i.t.	None	NA	[13, 14]
REOLYSIN	Orthoreovirus Dearing type 3	Ib	High-grade glioma with brain metastasis	EudraCT 2011-005635-10	i.v.	None	Surgery	[15]
Delta-24-RGD	Ad5	I	DIPG	NCT03178032	i.t.	None	Standard radiotherapy +/ chemotherapy	[16]
T-VEC	HSV-1	II	Resectable melanoma IIIB/C-IVM1a.	NCT02211131	i.t.	None	Surgery	[17]
NOUS-209	GAd、MVA	I/II	First/second-line metastatic dMMR/MSI-H colorectal, gastric cancer, and gastroesophageal junction adenocarcinoma	NCT04041310	i.t.	209 dMMR FSP	PD-1 ICB Pembrolizumab	[18-20]
GRANITE	ChAd68、VEEV	I/II	Various metastatic solid tumors, including NSCLC, colorectal cancer, gastroesophageal junction adenocarcinoma, and urothelial carcinoma.	NCT03639714	i.m.	Personalized Neoantigens	Standard chemotherapy, PD-1 ICB Nivolumab, CTLA-4 ICB Ipilimumab	[21]
Ad-sig-hMUC-1/ecdCD40L	Adv	I	Various advanced carcinomas, including lung, breast, ovarian, prostate and colorectal cancer.	NCT02140996	s.c.	Secretable MUC-1-CD40L	Standard chemotherapy	[22]
CAN-3110	HSV-1	I	Malignant gliomatosis, malignant astrocytoma, oligodendroglioma.	NCT03152318	i.t.	None	Standard chemotherapy	[23]
Delta-24-RGD	Ad5	I/II	Glioma, neuroendocrine tumor.	NCT02798406	i.t.	None	PD-1 ICB Pembrolizumab	[24]
T-VEC	HSV-1	II	Stage II-III triple-negative breast cancer.	NCT02779855	i.t.	None	Neoadjuvant chemotherapy, surgery	[25]

Table 1.1 A list of viral vectored cancer vaccines currently used in clinic or have reported clinical studies recently. i.t. intratumoral; i.m. intramuscular; s.c. subcutaneous; i.v. intravenous.

1.2　The balance between virulency, tropism, and fitness

Viral vectors serve as promising tools for cancer immunotherapy, capitalizing on the inflammatory environment created by viral replication. However, systemic infection of the virus may lead to uncontrolled consequences such as cytokine storm syndrome. As such, intratumorally injection of viral particles is often employed as a safer approach. Nevertheless, toxicity must be stringently controlled when utilizing live viral particles.

1.2.1 Attenuating pathogenicity

To achieve precise temporal and spatial control of viral replication, researchers have engineered genetic circuits based on gene expression regulation mechanisms. For instance, the vaccinia virus, previously employed as a vaccine against human smallpox, possesses a large genome that allows for the insertion of multiple foreign genes. Rapamycin, a Food and Drug Administration (FDA)-approved small molecule drug, can bind to FK506 binding protein（FKBP) and induce its conformational change that results in an enhance affinity between FKBP and FKBP-rapamycin binding protein (FRB).[26] Azad and colleagues split the T7 phage RNA polymerase into N-terminal and C-terminal domains and fused them to FKBP and FRB, respectively. They also positioned the T7 promoter upstream of the essential genes for viral replication. In the absence of rapamycin inside the cell, the split T7 polymerase N and C-terminal domains are unable to initiate gene transcription. Only in the presence of rapamycin does the formation of the FRB-rapamycin-

FKBP complex enable the assembly of functional T7 polymerase, leading to gene transcription and viral replication. In this scenario, rapamycin acts as an "on" switch for the virus.

Repressors are proteins that can bind to specific DNA sequences named operators and inhibit gene expression. Some small molecules can interfere with this process by binding to repressors and altering their shape or affinity for DNA. For instance, the TetR repressor normally binds to the TetO operator and blocks transcription of the downstream gene. However, when the tetracycline family antibiotic doxycycline is present, it binds to TetR and prevents it from binding to TetO, allowing downstream gene expression. Similarly, the CymR repressor binds to the CuO operator and inhibits gene expression unless cumate is added. Cumate binds to CymR and releases CuO, activating downstream gene expression. In this manner, doxycycline and cumate are used as "on" switches for viral gene expression. Researchers have used these switches to control the expression of genes responsible for viral spread, foreign antigen expression, and cytokine production. This approach has been found to improve both the safety profile and efficacy of immune responses against tumors.[27]

Existing mechanisms for gene transcription control prove challenging when applied to the modification of RNA viruses, whose replication often do not involve transcription. Consequently, Heilmann and colleagues have proposed an innovative approach that employs proteases to curtail viral replication. The replication process of the Vesicular stomatitis virus (VSV) is contingent on key proteins such as P and L. When the autocatalytic HIV protease and the C-terminal protease

cleavage site are inserted into the middle of the P or L sequence for fusion expression, the protease

can cleave the fusion protein, thereby inactivating it. Small molecule drugs used in clinical settings,

such as HIV protease inhibitors, can inhibit the function of the protease, thereby preserving the

activity of P and L proteins and facilitating viral replication. In this context, the inhibitor serves as

an "on" signal. The protease can also be fused to the N-terminus of the L virus as an "off" signal:

unlike fusion in the middle of the sequence, the presence of an N-terminal protease impairs the

function of L protein, preventing viral replication in an inhibitor environment. In the absence of

an inhibitor, however, the protease cleaves itself from the N-terminus of L protein, restoring its

normal function. Animal models have demonstrated that this system can effectively control the

replication and spread of a modified VSV virus in mice.[28]

1.2.2 Improving tumor tropism and modifying tissue fitness

Appropriate strategies can be employed to adjust viral fitness in a tissue-specific manner. For

instance, by inserting the complementary sequence of muscle tissue-specific microRNA (miRNA)

into the 3'UTR site of Coxsackievirus, viral replication within muscle tissue is inhibited. This is

due to the miRNA within the muscle tissue mediating the degradation of viral mRNA through

complementary pairing. However, in tumor tissues that lack this miRNA, the virus can replicate

normally.[29] More sophisticated "logic circuits" can also be constructed. Huang and colleagues, for

example, utilized tumor-associated promoters and transcription activation-like effect repression

(TALER) regulated by miRNA to construct a logic switch. This switch only activates when 1) the

tumor promoter is activated, 2) normal tissue-related miRNA is at a low level, and 3) tumor tissue-related miRNA is at a high level. This switch was then used to control adenovirus replication and the expression of immunomodulatory molecules. The modified adenovirus was able to specifically replicate within tumor cells and express carried immunoregulatory factors.[30]

Talimogene laherparepvec (T-VEC) is a genetically engineered variant of the Herpes Simplex Virus type 1 (HSV-1), which selectively replicates within tumor tissue. It has been approved for the local treatment of unresectable metastatic stage IIIB/C–IVM1a melanoma. The modifications to T-VEC include the addition of HSV-1 JS1 and US11, which enhance targeting and replication within tumor cells. To attenuate its pathogenicity in normal tissue, the ICP34.5 gene has been deleted. The ICP47 gene, which mediates suppression of antigen presentation, has also been removed. Furthermore, human granulocyte-macrophage colony-stimulating factor (GM-CSF) has been inserted. GM-CSF is a cytokine that promotes the recruitment and activation of dendritic cells (DCs).[12] G47Delta, which has completed Phase II clinical trials in Japan and has been approved for clinical use, is also based on HSV-1. In addition to the deletion of ICP34.5 like T-VEC, G47Delta further bears the inactivation of UL39 and the deletion of α47. These edits can restore the MHC I expression in host cells that was suppressed by the virus, which can enhance the presentation of tumor-associated antigens and reduce toxicity in normal tissues, without affecting the adaptability of tumor tissues[13, 14]. Another oncolytic virus based on HSV-1, CAN-3110, is currently in Phase I clinical studies. Unlike the aforementioned T-VEC and G47Delta,

CAN-3110 retains the functional ICP34.5 gene, but it is placed under the control of the nestin promoter. Nestin is overexpressed in gliomas and other similar tumors, yet its expression is relatively low in the adult brain and differentiated tissues. This characteristic enables CAN-3110 to be selectively enriched in tumors of the nervous system [23].

The tumor-specific adenovirus Delta-24-RGD, which is currently undergoing multiple clinical Phase I/II studies, has a deletion of 24 base pairs in its E1A gene to reduce its replication capability in normal tissues. The E1A gene in the adenoviral genome encodes an early expressed protein that can bind to the retinoblastoma protein (pRB) in the human tumor suppressor signaling pathway. The binding of the E1A protein to pRB releases the transcription factor E2F-1, which is normally inhibited by pRB, allowing the cell to enter the S phase and facilitate viral replication. The mutated E1A protein has a reduced affinity to pRB, thus this adenovirus replicates less efficiently in normal tissues. In some malignant tumors, such as gliomas, the pRB pathway is already inhibited, and E2F-1 is in an active state, so the mutated adenovirus can still replicate normally. On the other hand, adding an RGD sequence to its fiber enhanced the virus's binding affinity to integrins αvβ3 and αvβ5 on the surface of cancer cells.[16]

Guo and colleagues enhanced the tumor fitness of Alphavirus M1 through continuous passing and directed evolution in the HCT-116 colon cancer cell line.[31] Altering the protein used by the virus to invade cells can change its permissibility, thereby affecting the virus's toxicity to different

tissues. For instance, Das et al. reported that replacing VSV surface glycoprotein VSVg with Lymphocytic choriomeningitis virus (LCMV) glycoprotein could reduce its neurotoxicity.[32]

1.2.3 Intravenous viral vectored vaccines

Systemic administration, as compared to intratumorally injection, offers a wider range of applicability. Evidence from a clinical Ib window-of-opportunity trial suggests that human orthoreovirus, when administered intravenously, is capable of penetrating the blood-brain barrier and replicating within high-grade gliomas.[15] Similarly, in murine models, the Ankara strain of Vaccinia virus (MVA) has been observed to accumulate and replicate within tumors following a single intravenous injection.[33]

Ideally, live viruses introduced intravenously should exhibit tumor tropism and relatively low antigenicity and immunogenicity. This would prevent neutralization by serum antibodies and mitigate the risk of a systemic cytokine storm. For instance, human adenovirus hAdv-C5, when administered intravenously in mice, rapidly accumulates in the liver. Here it is primarily phagocytosed by Kupffer cells under the mediation by natural IgM and complement pathways. This process results in the production of inflammatory cytokines and induces acute hepatitis. Targeted mutation of the hexon hypervariable region 1 (HVR1) on the adenovirus capsid can eliminate its recognition by IgM and complement deposition, thereby reducing virus accumulation in Kupffer cells. Further modifications such as replacing the original RGD sequence in the penton of hAdv-C5 with the human laminin α1 sequence SIKVAV (which recognizes epithelial cell-

associated integrins α3β1, α6β1, and α6β4), can further reduce its macrophage tropism and enhance its ability to infect carcinoma cells. In murine models, this modified adenovirus has been shown to specifically accumulate within tumors following intravenous injection and persist for extended periods. However, it is important to note that these modifications can only evade recognition by existing natural IgM. They are unable to prevent newly induced, high-affinity IgG antibodies from neutralizing the virus post-immunization.[34]

In scenarios necessitating repeated immunization, the recurrent administration of a single virus can induce high-affinity serum neutralizing antibodies. This can potentially obscure the effects of subsequent immunizations. This issue can be partially circumvented by employing multiple distinct viruses carrying identical tumor antigens. An alternative strategy to evade the serum immune system in viral vaccine delivery involves encapsulating the virus within cells. Evgin and colleagues demonstrated this by infecting epidermal growth factor receptor variant III (EGFRvIII) directed CAR-T cells with VSV encoding mouse interferon β (mIFNβ) and delivering them to tumor-bearing mice. They observed that, compared to intravenously administered VSV alone, CAR-T cells were more effective in delivering VSV to tumors and the lymphatic system. Moreover, VSV-stimulated CAR-T cells exhibited enhanced *in vivo* proliferation and potentiated tumor-killing effects.[35] Another approach to bypass the humoral immune system involves discarding immunogenic molecules on the virus surface (such as membrane proteins and capsids) and delivering mRNA encoding viral genes via lipid nanoparticles (LNPs). Mouse studies indicate that

this strategy can successfully deliver mRNA from Seneca Valley virus and Coxsackievirus A21 intravenously to tumors, facilitating translation, assembly, and replication within the tumor. This occurs even in the presence of neutralizing antibodies against the virus in mouse serum. This strategy holds promise for situations requiring repeated systemic administration.[36] Serum antibodies against the vector may also enhance anti-tumor immunity. Ling et al. found that in the clinical phase I results regarding HSV-1-based CAN-3110, pre-existing and post-vaccination serum antibodies to HSV-1 were both associated with longer patient survival and better prognosis; in contrast, HSV-2 serum antibodies were unrelated to treatment outcomes.[23] The host's antiviral immunity against the vaccine vector can also be actively harnessed by other strategies for combating tumors. Niemann et al. discovered that in subcutaneous MC38, CMT-64 mouse lung cancers, and B16F10 mouse models with artificially high expression of poly(sialic acid), intratumorally administration of adenovirus Ad5 followed by intravenous delivery of a fusion protein composed of the Ad5 hexon DE1 antigen and a single-chain variable fragment (scFv) targeting poly(sialic acid) could label DE1 on tumor cells and make them recognizable by the host serum antiviral antibodies. This strategy increased intra-tumoral infiltration of $CD8^+$ T cells, promoted tumor elimination and long-term survival in mice, and sensitized tumors that were originally insensitive to PD-1 ICB.[37]

1.3 Viral vectored vaccines modulate TME

Viral replication, occurring *in situ*, leads to modifications of the tumor microenvironment. This effect can be further enhanced by viral vectored and/or co-administrated immune modulating signals, such as mAbs, chemokines, and cytokines.

1.3.1 Targeting dendritic cells

GM-CSF has been integrated into T-VEC to augment dendritic cell recruitment and activation. This augmentation subsequently facilitates tumor antigen presentation and promotes antigen spreading, a process that triggers the generation of *de novo* immune responses.[12]

In a mouse model, intratumorally vaccination with oncolytic Newcastle Disease Virus (NDV) was shown to activate DCs and sensitize them to dying tumor cells through the upregulation of dead-cell receptors. NDV was found to synergize with Fms-like tyrosine kinase 3 ligand (Flt3L), which mobilizes and expands intratumoral DC cells. The combined therapy led to the generation of cross-presenting conventional Type 1 DCs (cDC1s), type I IFN-dependent $CD4^+$ T helper 1 (Th1) effector cells, and neopeptide-reactive $CD8^+$ T cells in a subcutaneous murine A20 lymphoma model.[38]

Viral vectored vaccines can also encode CD40 ligand (CD40L),[22] a member of the tumor necrosis factor receptor family, which is considered a key costimulatory switch for DCs. CD40L encoded by MVA has been shown to stimulate DCs, thereby enabling them to prime tumor-specific $CD8^+$ T cells.[33]

1.3.2 Targeting macrophages

The intratumoral delivery of an oncolytic herpes simplex virus-1, which encodes a full-length anti-CD47 IgG1 mAb, was observed to enhance macrophage and natural killer (NK) cell activity in a mouse model with stereotactically implanted CT2A mouse glioblastoma (GBM) tumor. CD47, a surface protein that is overexpressed in certain cancer cells, binds to signal regulatory protein α (SIRPα) present on phagocytic cells such as macrophages. This binding sends an inhibitory signal that suppresses their phagocytic activity against cancer cells, thus serving as a "don't eat me" signal. The mAb secreted by the virus interrupts the CD47-SIRPα interaction, thereby restoring macrophage activity against cancer cells. Furthermore, the mAb mediates antibody-dependent cellular cytotoxicity (ADCC) against cancer cells expressing CD47 via NK cells. The virus demonstrated protective effects against intracranial GBM in mice.[39]

The antitumor activity of macrophages in GBM can also be restored through the manipulation of cholesterol efflux, specifically by using an adenovirus that produces apolipoprotein AI (ApoA1). ApoA1 serves as a ligand for the ATP-binding cassette transporter A1/G1 (ABCA1/G1) cholesterol efflux receptor, which is found to be upregulated in GBM tumor-associated macrophages (TAMs). This upregulation, along with the elevated expression of phagocytosis-inhibitory receptors such as sialic acid binding Ig-like lectin 10 (Siglec-10) and programmed cell death 1 (PD-1), is a consequence of cholesterol accumulation in GBM. The stimulation of ABCA1/G1 through the adenovirus produced ApoA1 has been observed to reverse the deficiency

in macrophage phagocytosis, leading to tumor clearance. This effect was demonstrated in mouse orthotopic GBM models with GL261 and G422 tumors. Furthermore, the intratumoral administration of the virus was found to enhance systemic antitumor immunity and establish long-term tumor-specific memory.[40]

1.3.3 Targeting T cells

An engineered vaccinia virus, which encodes interleukin-12 (IL-12) and interleukin-7 (IL-7), has shown promise in modulating the immunosuppressive TME when delivered intratumorally in a mouse model. IL-12 serves to activate NK and T cells, thereby amplifying the production and secretion of interferon-γ. Concurrently, IL-7 plays a crucial role in maintaining T cell homeostasis and exhibits a synergistic effect on T cell stimulation when combined with IL-12. In the context of mouse models with low immunogenicity, specifically B16-F10 and Lewis lung carcinoma (LLC), viral replication coupled with cytokine production triggered inflammatory responses and increased the presence of tumor-infiltrating lymphocytes (TILs). TILs serve as an indicator of tumor immunogenicity and have a direct correlation with anti-tumor immunity. This culminated in the rejection of both treated and distant untreated tumor deposits (abscopal effect), stimulating an immune memory response that safeguarded the mice against subsequent challenges. Additionally, the virus was found to increase tumor sensitivity to anti-PD-1 and cytotoxic T lymphocyte-associated protein 4 (CTLA-4) mAb therapy.[41]

Viral vectored interleukin-2 (IL-2) can also modify TME. IL-2 is a potent T-cell mitogen and activator that can extend the function of T-cells and facilitate tumor clearance. Clinically, systemic administration of IL-2 is associated with severe toxicity. An IL-2 construct consisting of a glycosylphosphatidylinositol (GPI) anchor with a rigid peptide linker fused to IL-2 was delivered by oncolytic vaccinia virus. Intratumoral vaccination with the recombinant vaccinia virus led to local expression of IL-2 and was shown to induce potent antitumor CD8^{+} T cell responses in MC38, LLC, and CT26 models, without toxic side effects.[42]

Viral vectored vaccines can also synergize with ICB. Intratumoral vaccination with vaccinia virus expressing anti-PD-L1 mAb and GM-CSF enhanced tumor infiltration of lymphocytes and DC cells, promoted maturation of DCs and neoantigen presentation, enhanced antitumoral CTL responses, thus leading to rejection of both treated and distant tumors in murine models with B16-F10, Py230, and MC38 cells.[43] Intratumoral vaccination with rotavirus was found to synergize with anti-CTLA-4 and anti-PD-L1 mAbs.[4]

Leptin is a canonical adipokine with potent metabolic reprogramming functions such as the promotion of glucose and fatty acid oxidation and mitochondrial biogenesis. T cells stimulated in the context of leptin can synthesize more cytokines and increase their proliferation. Vaccinia virus engineered to express leptin in tumor cells induced complete responses in tumor-bearing mice and supported memory development in the tumor infiltrate.[44]

1.3.4 Targeting tumor cells

Trametinib, a clinical drug that inhibits the mitogen-activated protein kinase kinase (MEK) pathway in melanoma cells, was combined with intratumorally administrated T-VEC encoding mouse GM-CSF in a mouse D4M3 melanoma tumor model. The combination therapy significantly inhibited tumor growth, induced antigen spreading, increased tumor infiltrating CD8^{+} T cells, and improved T cell activation with higher levels of interferon γ (IFNγ), granzyme B, and Ki67. The therapy also increased programmed cell death ligand 1 (PD-L1) expression in the TME and sensitized the tumor to anti-PD-1 mAb in D4M3 and CT26 mouse tumor models.[45]

Phosphatase and tensin homolog deleted on chromosome 10 (PTEN) encodes a lipid/protein phosphatase and is characterized as a tumor suppressor gene for its role in antagonizing the phosphatidylinositol-4,5-bisphosphate 3-kinase/protein kinase B (PI3K/AKT) pathway. In a murine intracranial DB7 breast cancer model, HSV-P10, an oncolytic herpesvirus encoding PTENα, was delivered intratumorally and reduced AKT phosphorylation and AKT/ mammalian target of rapamycin (mTOR) activity, increased mitochondrial membrane potential, and enhanced adenosine triphosphate (ATP) secretion, which serves as a DAMP due to its correlation with cell membrane damage. HSV-P10 increased the infiltration of CD8^{+} T cells, reduced PD-L1 expression, prolonged the survival of tumor-bearing mice, and induced a memory response against tumor rechallenge.[46]

Viral vectored vaccines can also encode cytotoxic agents such as pyroptosis-inducing molecule N-terminal gasdermin domain (GSDM^{NT}). Recombinant adeno-associated viruses (rAAVs) expressing GSDM^{NT} induced a robust anti-tumor immune response in a rat intracranial C6 GBM model. rAAVs temporarily opened the blood-brain barrier and recruited tumor-infiltrating lymphocytes into the brain. The oncolytic effect was further improved in combination with anti-PD-L1 ICB. Oncolytic parapoxvirus ovis (ORFV) can also induce cell pyroptosis owing to its ability to activate the gasdermin E (GSDME) pathway. Consequently, ORFV sensitized immunologically 'cold' tumors to checkpoint blockade in mouse B16 and 4T1 models. Similarly, recombinant measles virus vaccine strain rMV-Hu191 was shown to induce pyroptosis in a mouse esophageal squamous cell carcinoma (ESCC) xenograft model via caspase-3/GSDME-mediated pathways.[47]

Tumor cells can be labeled with chemokines that can recruit immune cells. For example, chemokine C-C motif ligand 5 (CCL5) is an inflammatory chemokine that promotes chemotaxis of immune cells by interacting with C-C chemokine receptor type 1(CCR1) and/or type 5 (CCR5). A chimeric antibody-like molecule consists of a single chain of epidermal growth factor receptor (EGFR) mAb cetuximab scFv fused to IgG1 Fc and another chain of CCL5 fused to IgG1 Fc acts like a bispecific antibody. It binds to EGFR on cancer cells, delivers CCL5 to the TME, and mediates ADCC via Fc. In mouse intracranial C2A-EGFR GBM models, intratumoral vaccination with oncolytic herpes simplex virus type 1 (oHSV) encoding the secretable bispecific protein

significantly enhanced the infiltration and activation of natural killer cells, macrophages, and T cells; inhibited tumor EGFR signaling; reduced tumor size; and prolonged survival of tumor-bearing mice. Vaccination also induced abscopal effect.[48]

1.4 Antigen loading methods of viral vectored cancer vaccines

In addition to triggering ICD and the release of tumor antigens in situ, viral vectors can also be engineered to carry various forms of tumor antigens. Viral particles have the ability to infect cells, deliver the loaded antigens into the cytoplasm, and promote antigen presentation to MHC I molecules, thereby favoring CTL responses.

1.4.1 Introduction of tumor associated antigens post viral assembly

Antigens can be conjugated to proteins on the surface of viral vaccines via chemical reactions or physical adsorption. Click Chemistry, awarded the Nobel Prize in Chemistry in 2022, is extensively utilized for the chemical modification of virus surfaces. Ji and colleagues employed Click Chemistry to introduce the model antigen OVA peptides onto the surface of a modified influenza virus, subsequently verifying its capacity to induce anti-tumor immune responses.[49] Physical adsorption is another method used for antigen modification on the virus surface. Fusciello and colleagues isolated cell membranes from tumor cell lines, such as B16-F10, and repeatedly extruded them with the adenovirus Delta-24-RGD until a membrane-virus composite vaccine was formed with the cell membrane enveloping the virus surface. Consequently, membrane proteins and other antigens on the surface of tumor cells could be introduced onto the virus surface via cell

membrane mediation. This approach demonstrated preventive and therapeutic anti-tumor immune effects in animal experiments, potentially circumventing the need for identification, characterization, and synthesis of tumor-associated antigens.[50]

Roy and colleagues discovered that antigens do not necessarily need to be associated with viruses at the molecular level. A mixture of viruses serving as adjuvants and antigen peptides can effectively present peptide antigens. In mouse models, researchers employed four different viruses, including adenovirus, Maraba Virus, VSV, and Vaccinia virus, mixed with peptide antigens for heterologous alternating immunization. This approach stimulated effective anti-tumor immune responses.[51]

1.4.2 Genetic engineering for antigen expression

The new generation of virus particles replicated by these late stage-modified particles will not contain the corresponding antigens. For a more consistent and stable delivery of antigens, it is a common practice to integrate the genes encoding tumor antigens into the virus particles. D'Alise and colleagues identified 31 novel T-cell antigens, which are produced by single base mutations, from the CT26 mouse colon cancer cell line through sequencing and antigenicity prediction. These antigens were expressed as a fusion artificial antigen protein. The tumor vaccine was developed by introducing the gene of this antigen protein into the Gorilla Adenovirus (GAd). Animal models have demonstrated that GAd vaccines encoding neoantigens can trigger T-cell responses. After a single immunization in mice, T-cell responses were observed for seven antigens via enzyme-linked

immunospot assay (ELISpot), among which 3 CD4^{+} T cell and 3 CD8^{+} T cell responses were

detected via flow cytometry. These tumor-specific T cells do not recognize unmutated native

proteins and can inhibit tumor occurrence and development.[52] Animal models have further shown

that GAd vaccines encoding tumor neoantigens can enhance the stemness of tumor-specific CD8^{+}

T cells.[19] The anti-tumor vaccine Nous209, which is based on GAd and MVA, is currently

undergoing phase I[18] and phase I/II[20] clinical trials. Nous209 encodes 209 frameshift peptide (FSP)

antigens that are shared among patients with DNA mismatch repair-deficient (dMMR) tumors.

Preliminary results indicate that Nous209, in combination with anti-PD-1 mAb therapy, is safe in

patients with dMMR cancer and effectively induces anti-tumor immune responses.

The viral vectored vaccine GRANITE, which is designed to encode tumor neoantigens, is

presently in the midst of phase I/II clinical trials. GRANITE is composed of two key components:

the Chimpanzee Adenovirus ChAd68, which encodes neo antigens, and the Venezuelan Equine

Encephalitis Virus (VEEV) vectored self-amplifying RNA (samRNA) also encoding neo antigens.

The treatment strategy involves an alternating immunization schedule with these two viruses,

supplemented with PD-1 and CTLA-4 mAbs. This regimen is being explored for the treatment of

advanced metastatic solid tumors. Preliminary results suggest that this therapeutic approach is safe

and capable of inducing a potent anti-tumor T-cell response.[21]

The adenovirus vectored vaccine Ad-sig-hMUC1/ecdCD40L, which is designed to encode the

tumor-associated antigen human mucin-1 (hMUC-1), has exhibited anti-tumor properties in

animal models. This vaccine expresses a fusion protein that combines hMUC-1 and human CD40L. Safety of this vaccine has been demonstrated in phase I clinical trials in patients with advanced adenocarcinoma exhibiting high expression levels of hMUC-1.[22]

Numerous preclinical studies are exploring the use of viruses encoding tumor antigens as vaccines. Ring and colleagues have reported on a non-pathogenic (LCMV) that encodes tumor associated antigen tyrosinase-related protein 2 (TRP2). This vaccine has shown potential in reprogramming Fibroblast Stromal Cells (FSCs) in mouse models, thereby recruiting antigen-specific $CD8^+$ T cells to control tumor growth.[53] Smith and colleagues have discussed an adenovirus, Ad5-TRP2, which encodes TRP2. In both preventive and therapeutic mouse models, this vaccine, when combined with Polylactic Acid-Polyglycolic acid copolymer/dendritic Polyamidoamine (PLGA/PAMAM) nanoparticle adjuvants, has demonstrated potential in inhibiting the occurrence and growth of subcutaneous B16F10 mouse melanoma.[54] Das et al. have reported on the effects of alternating immunization with Vesicular Stomatitis Virus (VSV-GP-TAA) encoding tumor-associated antigens and the artificial protein antigen KISMA in mouse models. The encoded tumor-associated antigens include OVA, neoantigen Adpgk, Reps1, and HPV-related antigen E7. KISIMA, on the other hand, is an artificial fusion protein that contains antigen peptides, cell penetrating peptides, and toll-like receptor 2/4 (TLR2/TLR4) ligand peptides. The researchers observed that alternating immunization with the virus and protein yielded superior anti-tumor effects compared to a single vaccine.[32] Moshaheb and colleagues have reported on the

anti-tumor effects of the chimeric virus PVSRIPO, which encodes the tumor-associated antigen DMG/DIPG H3.3K27M, in mouse models. PVSRIPO is a genetically stable hybrid virus of poliovirus and rhinovirus that can infect DC cells to present antigens. Antigen encoding PVSRIPO has been shown to activate CD8+ T cells, and delay tumor growth in animal models.[55] Medina et al. have reported on MVA vectored vaccine rMVA-CD40L-TAA encoding tumor-associated antigens (TAAs). Animal experiments show that rMVA-CD40L-TAA can not only expand CD8+ T cells but also activate NK cells after a single intravenous immunization. It can synergistically kill tumors in combination with anti-tumor mAb TA99.[33]

1.5   Conclusions and future outlooks

Viral vectors are appealing carriers for the development of cancer vaccines. They are relatively simple and well-characterized compared to bacterial and cell-based vaccines, and the mechanisms of viral replication and spreading have often been extensively studied. Rational engineering of viral vectors has been conducted to improve their safety profile, *in vivo* distribution, and tumor fitness, taking advantage of their flexibility. Most viral vectors are administered intratumorally, while some enhancements have enabled systemic injection. Numerous immune-stimulating molecules, expressed by the viral vector or administered separately, have been used to stimulate both innate and adaptive immune cells, enhancing their ability to modify the immunosuppressive TME. Tumor-associated antigens have been introduced to the vector via different methods to generate tumor-specific T cell responses.

Challenges still exist for the substantial clinical use of viral vectors. A recent trial of AAV vectored gene therapy resulted in a catastrophic outcome: the 27-year-old patient died 8 days post-infusion of a high dose of recombinant AAV. Examination suggested that an innate immune reaction against the vector caused acute respiratory distress syndrome (ARDS), potentially leading to the multiorgan failure, which caused the patient's death.[56] Unlike gene therapy which aims to modify most of an individual's cells, vaccines potentially require transformation of a much smaller number of cells, thus requiring a smaller dosage. However, this incident still alerts us that the outcome of delivering a live virus to an individual is not well studied and clearly established, despite numerous clinical trials conducted. Here we reviewed a few efforts to improve safety of the viral vectors, and it will remain a crucial aim for future studies.

The impact of immune responses against vaccine vectors on anti-tumor immunity is another challenge in the development of viral vector-based cancer vaccines. The generation of immune responses is an energy-intensive process.[57] Immune responses directed against the vector may compete with anti-tumor immunity for energy, nutrients, and cellular resources. However, the innate immune response against the vector may also kill tumor cells in a non-specific manner and enhance anti-tumor immunity. Experience from the development of infectious disease vaccines suggest that pre-existing immunity to the vector seems to enhance humoral immunity against the target antigen but reduce cellular immunity.[58] The influence of preexisting antiviral immunity on the occurrence and evolution of antitumor immunity is currently only preliminarily understood.[59-

[61] As previously summarized, we have discussed several methods to reduce host antiviral immune responses, as well as examples of directing antiviral immune responses towards the tumor.

In response to these challenges, in addition to conducting more in-depth research and understanding of the mechanisms of pathogen-host immune interactions and cancer biology, we may also not overlook the differences between the immune systems of different individuals. We may not only need "personalized" antigens but also "personalized" vectors. For instance, the level of pre-existing serum anti-vector antibodies can affect not only the immune efficacy but also the probability of severe allergic reactions occurring post vaccination. Apart from differences in pre-existing antibody levels, HLA polymorphism can also affect the pathogenicity of a specific pathogen. For example, recent research indicates that in individuals carrying HLA-B*15:01, due to their immune cells' more efficient presentation of a common coronavirus epitope, these individuals' T cells can recognize cells infected by a variety of different coronaviruses more strongly and broadly: people in this category often exhibit milder symptoms after infection with the SARS-CoV-2.[62] Considering that in this example, the widespread prevalence of common cold coronaviruses in the population may have selected for such advantageous genes, for other viruses that are widely disseminated in the population, such as adenoviruses, HSV, etc., their pathogenicity and antigen presentation efficiency may also be influenced by HLA polymorphism. Therefore, clinical research on microbial vector vaccines may need to consider the impact of patient genotypic differences.

The complexity of tumors represents another significant challenge in the development of cancer vaccines. A successful cancer vaccine may require the simultaneous application of knowledge from microbiology, cancer biology, and immunology to address the numerous difficulties in this field. Therefore, interdisciplinary collaboration is of paramount importance. Moreover, due to the heterogeneity and high mutation rate of tumor cells, any anti-tumor therapy targeting a specific aspect or mechanism of the tumor is ultimately likely to fail due to antigen loss or other forms of resistance. Consequently, cancer vaccines currently in clinical research are often combined with other therapies, such as radiotherapy, chemotherapy, ICB, etc. The trend towards combination therapies is expected to continue, and future research directions may involve more findings from other fields, such as new bioinformatics methods, deep learning, and artificial intelligence, combined with cancer vaccines to combat tumors from multiple different angles, thereby improving the survival and quality of life of cancer patients.

REFERENCES

1. Siegel, R. L.; Miller, K. D.; Fuchs, H. E.; Jemal, A., Cancer statistics, 2022. *CA Cancer J Clin* **2022,** *72* (1), 7-33.

2. Rojas, L. A.; Sethna, Z.; Soares, K. C.; Olcese, C.; Pang, N.; Patterson, E.; Lihm, J.; Ceglia, N.; Guasp, P.; Chu, A.; Yu, R.; Chandra, A. K.; Waters, T.; Ruan, J.; Amisaki, M.; Zebboudj, A.; Odgerel, Z.; Payne, G.; Derhovanessian, E.; Muller, F.; Rhee, I.; Yadav, M.; Dobrin, A.; Sadelain, M.; Luksza, M.; Cohen, N.; Tang, L.; Basturk, O.; Gonen, M.; Katz, S.; Do, R. K.; Epstein, A. S.; Momtaz, P.; Park, W.; Sugarman, R.; Varghese, A. M.; Won, E.; Desai, A.; Wei, A. C.; D'Angelica, M. I.; Kingham, T. P.; Mellman, I.; Merghoub, T.; Wolchok, J. D.; Sahin, U.; Tureci, O.; Greenbaum, B. D.; Jarnagin, W. R.; Drebin, J.; O'Reilly, E. M.; Balachandran, V. P., Personalized RNA neoantigen vaccines stimulate T cells in pancreatic cancer. *Nature* **2023,** *618* (7963), 144-150.

3. Hanahan, D., Hallmarks of Cancer: New Dimensions. *Cancer Discov* **2022,** *12* (1), 31-46.

4. Shekarian, T.; Sivado, E.; Jallas, A. C.; Depil, S.; Kielbassa, J.; Janoueix-Lerosey, I.; Hutter, G.; Goutagny, N.; Bergeron, C.; Viari, A.; Valsesia-Wittmann, S.; Caux, C.; Marabelle, A., Repurposing rotavirus vaccines for intratumoral immunotherapy can overcome resistance to immune checkpoint blockade. *Sci Transl Med* **2019,** *11* (515), eaat5025 DOI: 10.1126/scitranslmed.aat5025.

5. Wieland, A.; Patel, M. R.; Cardenas, M. A.; Eberhardt, C. S.; Hudson, W. H.; Obeng, R. C.; Griffith, C. C.; Wang, X.; Chen, Z. G.; Kissick, H. T.; Saba, N. F.; Ahmed, R., Defining HPV-specific B cell responses in patients with head and neck cancer. *Nature* **2021,** *597* (7875), 274-278.

6. Ferreiro-Iglesias, A.; McKay, J. D.; Brenner, N.; Virani, S.; Lesseur, C.; Gaborieau, V.; Ness, A. R.; Hung, R. J.; Liu, G.; Diergaarde, B.; Olshan, A. F.; Hayes, N.; Weissler, M. C.; Schroeder, L.; Bender, N.; Pawlita, M.; Thomas, S.; Pring, M.; Dudding, T.; Kanterewicz, B.; Ferris, R.; Thomas, S.; Brhane, Y.; Diez-Obrero, V.; Milojevic, M.; Smith-Byrne, K.; Mariosa, D.; Johansson, M. J.; Herrero, R.; Boccia, S.; Cadoni, G.; Lacko, M.; Holcatova, I.; Ahrens, W.; Lagiou, P.; Lagiou, A.; Polesel, J.; Simonato, L.; Merletti, F.; Healy, C. M.; Hansen, B. T.; Nygard, M.; Conway, D. I.; Wright, S.; Macfarlane, T. V.; Robinson, M.; Alemany, L.; Agudo, A.; Znaor, A.; Amos, C. I.; Waterboer, T.; Brennan, P., Germline determinants of humoral immune response to HPV-16 protect against oropharyngeal cancer. *Nat Commun* **2021,** *12* (1), 5945.

7. Eberhardt, C. S.; Kissick, H. T.; Patel, M. R.; Cardenas, M. A.; Prokhnevska, N.; Obeng, R. C.; Nasti, T. H.; Griffith, C. C.; Im, S. J.; Wang, X.; Shin, D. M.; Carrington, M.; Chen, Z. G.; Sidney, J.; Sette, A.; Saba, N. F.; Wieland, A.; Ahmed, R., Functional HPV-specific PD-1(+) stem-like CD8 T cells in head and neck cancer. *Nature* **2021,** *597* (7875), 279-284.

8. Rosato, P. C.; Wijeyesinghe, S.; Stolley, J. M.; Nelson, C. E.; Davis, R. L.; Manlove, L. S.; Pennell, C. A.; Blazar, B. R.; Chen, C. C.; Geller, M. A.; Vezys, V.; Masopust, D., Virus-specific memory T cells populate tumors and can be repurposed for tumor immunotherapy. *Nat Commun* **2019,** *10* (1), 567.

9. Strickley, J. D.; Messerschmidt, J. L.; Awad, M. E.; Li, T.; Hasegawa, T.; Ha, D. T.; Nabeta, H. W.; Bevins, P. A.; Ngo, K. H.; Asgari, M. M.; Nazarian, R. M.; Neel, V. A.; Jenson, A. B.; Joh, J.; Demehri, S., Immunity to commensal papillomaviruses protects against skin cancer. *Nature* **2019,** *575* (7783), 519-522.

10. Restrepo, J.; Herrera, T.; Samakoses, R.; Reina, J. C.; Pitisuttithum, P.; Ulied, A.; Bekker, L. G.; Moreira, E. D.; Olsson, S. E.; Block, S. L.; Hammes, L. S.; Laginha, F.; Ferenczy, A.; Kurman, R.; Ronnett, B. M.; Stoler, M.; Bautista, O.; Gallagher, N. E.; Salituro, G.; Ye, M.; Luxembourg, A., Ten-Year Follow-up of 9-Valent Human Papillomavirus Vaccine: Immunogenicity, Effectiveness, and Safety. *Pediatrics* **2023,** *152* (4), e2022060993. DOI: 10.1542/peds.2022-060993.

11. Roden, R.; Wu, T. C., How will HPV vaccines affect cervical cancer? *Nat Rev Cancer* **2006,** *6* (10), 753-763.

12. Ferrucci, P. F.; Pala, L.; Conforti, F.; Cocorocchio, E., Talimogene Laherparepvec (T-VEC): An Intralesional Cancer Immunotherapy for Advanced Melanoma. *Cancers* **2021,** *13* (6), 1383.

13. Todo, T.; Ino, Y.; Ohtsu, H.; Shibahara, J.; Tanaka, M., A phase I/II study of triple-mutated oncolytic herpes virus G47Δ in patients with progressive glioblastoma. *Nat Commun* **2022,** *13* (1), 4119.

14. Todo, T.; Ito, H.; Ino, Y.; Ohtsu, H.; Ota, Y.; Shibahara, J.; Tanaka, M., Intratumoral oncolytic herpes virus G47Δ for residual or recurrent glioblastoma: a phase 2 trial. *Nat Med* **2022,** *28* (8), 1630-1639.

15. Samson, A.; Scott, K. J.; Taggart, D.; West, E. J.; Wilson, E.; Nuovo, G. J.; Thomson, S.; Corns, R.; Mathew, R. K.; Fuller, M. J.; Kottke, T. J.; Thompson, J. M.; Ilett, E. J.; Cockle, J. V.; van Hille, P.; Sivakumar, G.; Polson, E. S.; Turnbull, S. J.; Appleton, E. S.; Migneco, G.; Rose, A. S.; Coffey, M. C.; Beirne, D. A.; Collinson, F. J.; Ralph, C.; Alan Anthoney, D.; Twelves, C. J.; Furness, A. J.; Quezada, S. A.; Wurdak, H.; Errington-Mais, F.; Pandha, H.; Harrington, K. J.; Selby, P. J.; Vile, R. G.; Griffin, S. D.; Stead, L. F.; Short, S. C.; Melcher, A. A., Intravenous delivery of oncolytic reovirus to brain tumor patients immunologically primes for subsequent checkpoint blockade. *Sci Transl Med* **2018,** *10* (422), eaam7577. DOI: 10.1126/scitranslmed.aam7577.

16. Martinez-Velez, N.; Garcia-Moure, M.; Marigil, M.; Gonzalez-Huarriz, M.; Puigdelloses, M.; Gallego Perez-Larraya, J.; Zalacain, M.; Marrodan, L.; Varela-Guruceaga, M.; Laspidea, V.; Aristu, J. J.; Ramos, L. I.; Tejada-Solis, S.; Diez-Valle, R.; Jones, C.; Mackay, A.; Martinez-Climent, J. A.; Garcia-Barchino, M. J.; Raabe, E.; Monje, M.; Becher, O. J.; Junier, M. P.; El-Habr, E. A.; Chneiweiss, H.; Aldave, G.; Jiang, H.; Fueyo, J.; Patino-Garcia, A.; Gomez-Manzano, C.; Alonso, M. M., The oncolytic virus Delta-24-RGD elicits an antitumor effect in pediatric glioma and DIPG mouse models. *Nat Commun* **2019,** *10* (1), 2235.

17. Dummer, R.; Gyorki, D. E.; Hyngstrom, J.; Berger, A. C.; Conry, R.; Demidov, L.; Sharma, A.; Treichel, S. A.; Radcliffe, H.; Gorski, K. S.; Anderson, A.; Chan, E.; Faries, M.; Ross, M. I., Neoadjuvant talimogene laherparepvec plus surgery versus surgery alone for resectable stage IIIB-IVM1a melanoma: a randomized, open-label, phase 2 trial. *Nat Med* **2021,** *27* (10), 1789-1796.

18. Overman, M.; Fakih, M.; Le, D.; Shields, A.; Pedersen, K.; Shah, M.; Mukherjee, S.; Faivre, T.; Leoni, G.; D'Alise, A. M.; Cotugno, G.; Langone, F.; Capone, S.; Sorbo, M. R. D.; Scarselli, E.; Delaite, P., Phase I interim study results of Nous-209, an off-the-shelf immunotherapy, with pembrolizumab, for the treatment of tumors with a deficiency in mismatch repair/microsatellite instability (dMMR/MSI). *J Immunother Cancer* **2021,** *9* (Suppl 2), A441-A441. DOI: 10.1136/jitc-2021-SITC2021.410.

19. D'Alise, A. M.; Brasu, N.; De Intinis, C.; Leoni, G.; Russo, V.; Langone, F.; Baev, D.; Micarelli, E.; Petiti, L.; Picelli, S.; Fakih, M.; Le, D. T.; Overman, M. J.; Shields, A. F.; Pedersen, K. S.; Shah, M. A.; Mukherjee, S.; Faivre, T.; Delaite, P.; Scarselli, E.; Pace, L., Adenoviral-based vaccine promotes neoantigen-specific CD8(+) T cell stemness and tumor rejection. *Sci Transl Med* **2022,** *14* (657), eabo7604. DOI: 10.1126/scitranslmed.abo7604.

20. Overman, M. J.; Maurel, J.; Oberstein, P. E.; Roselló-Keränen, S.; Le, D. T.; Pedersen, K. S.; Mukherjee, S.; D'Alise, A. M.; Leoni, G.; Siani, L.; Scarselli, E.; Faivre, T.; Delaite, P.; Gogov, S.; Fakih, M., Results of phase I-II bridging study for Nous-209, a neoantigen cancer immunotherapy, in combination with pembrolizumab as first line treatment in patients with advanced dMMR/MSI-h colorectal cancer. *J Clin Oncol* **2023,** *41* (16_suppl), e14665-e14665. DOI: 10.1200/JCO.2023.41.16_suppl.e14665.

21. Palmer, C. D.; Rappaport, A. R.; Davis, M. J.; Hart, M. G.; Scallan, C. D.; Hong, S. J.; Gitlin, L.; Kraemer, L. D.; Kounlavouth, S.; Yang, A.; Smith, L.; Schenk, D.; Skoberne, M.; Taquechel, K.; Marrali, M.; Jaroslavsky, J. R.; Nganje, C. N.; Maloney, E.; Zhou, R.; Navarro-Gomez, D.; Greene, A. C.; Grotenbreg, G.; Greer, R.; Blair, W.; Cao, M. D.; Chan, S.; Bae, K.; Spira, A. I.; Roychowdhury, S.; Carbone, D. P.; Henick, B. S.; Drake, C. G.; Solomon, B. J.; Ahn, D. H.; Mahipal, A.; Maron, S. B.; Johnson, B.; Rousseau, R.; Yelensky, R.; Liao, C. Y.; Catenacci, D. V. T.; Allen, A.; Ferguson, A. R.; Jooss, K., Individualized, heterologous chimpanzee adenovirus and self-amplifying mRNA neoantigen vaccine for advanced metastatic solid tumors: phase 1 trial interim results. *Nat Med* **2022,** *28* (8), 1619-1629.

22. Tan, T. J.; Ang, W. X. G.; Wang, W. W.; Chong, H. S.; Tan, S. H.; Cheong, R.; Chia, J. W.; Syn, N. L.; Shuen, W. H.; Ba, R.; Kaliaperumal, N.; Au, B.; Hopkins, R.; Li, X.; Tan, A. C.; Seet, A. O. L.; Connolly, J. E.; Arkachaisri, T.; Chew, V.; Lajam, A. B. M.; Guo, D.; Chew, M. Z. W.; Wasser, M.; Kumar, P.; Albani, S.; Toh, H. C., A phase I study of an adenoviral vector delivering a MUC1/CD40-ligand fusion protein in patients with advanced adenocarcinoma. *Nat Commun* **2022,** *13* (1), 6453.

23. Ling, A. L.; Solomon, I. H.; Landivar, A. M.; Nakashima, H.; Woods, J. K.; Santos, A.; Masud, N.; Fell, G.; Mo, X.; Yilmaz, A. S.; Grant, J.; Zhang, A.; Bernstock, J. D.; Torio, E.; Ito, H.; Liu, J.; Shono, N.; Nowicki, M. O.; Triggs, D.; Halloran, P.; Piranlioglu, R.; Soni, H.; Stopa, B.; Bi, W. L.; Peruzzi, P.; Chen, E.; Malinowski, S. W.; Prabhu, M. C.; Zeng, Y.; Carlisle, A.; Rodig, S. J.; Wen, P. Y.; Lee, E. Q.; Nayak, L.; Chukwueke, U.; Gonzalez Castro, L. N.; Dumont, S. D.; Batchelor, T.; Kittelberger, K.; Tikhonova, E.; Miheecheva, N.; Tabakov, D.; Shin, N.; Gorbacheva, A.; Shumskiy, A.; Frenkel, F.; Aguilar-Cordova, E.; Aguilar, L. K.; Krisky, D.; Wechuck, J.; Manzanera, A.; Matheny, C.; Tak, P. P.; Barone, F.; Kovarsky, D.; Tirosh, I.; Suva, M. L.; Wucherpfennig, K. W.; Ligon, K.; Reardon, D. A.; Chiocca, E. A., Clinical trial links oncolytic immunoactivation to survival in glioblastoma. *Nature* **2023,** *623* (7985), 157-166.

24. Nassiri, F.; Patil, V.; Yefet, L. S.; Singh, O.; Liu, J.; Dang, R. M. A.; Yamaguchi, T. N.; Daras, M.; Cloughesy, T. F.; Colman, H.; Kumthekar, P. U.; Chen, C. C.; Aiken,

R.; Groves, M. D.; Ong, S. S.; Ramakrishna, R.; Vogelbaum, M. A.; Khagi, S.; Kaley, T.; Melear, J. M.; Peereboom, D. M.; Rodriguez, A.; Yankelevich, M.; Nair, S. G.; Puduvalli, V. K.; Aldape, K.; Gao, A.; Lopez-Janeiro, A.; de Andrea, C. E.; Alonso, M. M.; Boutros, P.; Robbins, J.; Mason, W. P.; Sonabend, A. M.; Stupp, R.; Fueyo, J.; Gomez-Manzano, C.; Lang, F. F.; Zadeh, G., Oncolytic DNX-2401 virotherapy plus pembrolizumab in recurrent glioblastoma: a phase 1/2 trial. *Nat Med* **2023,** *29* (6), 1370-1378.

25. Soliman, H.; Hogue, D.; Han, H.; Mooney, B.; Costa, R.; Lee, M. C.; Niell, B.; Williams, A.; Chau, A.; Falcon, S.; Soyano, A.; Armaghani, A.; Khakpour, N.; Weinfurtner, R. J.; Hoover, S.; Kiluk, J.; Laronga, C.; Rosa, M.; Khong, H.; Czerniecki, B., Oncolytic T-VEC virotherapy plus neoadjuvant chemotherapy in nonmetastatic triple-negative breast cancer: a phase 2 trial. *Nat Med* **2023,** *29* (2), 450-457.

26. Banaszynski, L. A.; Liu, C. W.; Wandless, T. J., Characterization of the FKBP.rapamycin.FRB ternary complex. *J Am Chem Soc* **2005,** *127* (13), 4715-4721.

27. Azad, T.; Rezaei, R.; Singaravelu, R.; Pelin, A.; Boulton, S.; Petryk, J.; Onsu, K. A.; Martin, N. T.; Hoskin, V.; Ghahremani, M.; Marotel, M.; Marius, R.; He, X.; Crupi, M. J. F.; Hoang, H. D.; Nik-Akhtar, A.; Ahmadi, M.; Zamani, N. K.; Golshani, A.; Alain, T.; Greer, P.; Ardolino, M.; Dickinson, B. C.; Tai, L. H.; Ilkow, C. S.; Bell, J. C., Synthetic virology approaches to improve the safety and efficacy of oncolytic virus therapies. *Nat Commun* **2023,** *14* (1), 3035.

28. Heilmann, E.; Kimpel, J.; Hofer, B.; Rossler, A.; Blaas, I.; Egerer, L.; Nolden, T.; Urbiola, C.; Krausslich, H. G.; Wollmann, G.; von Laer, D., Chemogenetic ON and OFF switches for RNA virus replication. *Nat Commun* **2021,** *12* (1), 1362.

29. Kelly, E. J.; Hadac, E. M.; Greiner, S.; Russell, S. J., Engineering microRNA responsiveness to decrease virus pathogenicity. *Nat Med* **2008,** *14* (11), 1278-1283.

30. Huang, H.; Liu, Y.; Liao, W.; Cao, Y.; Liu, Q.; Guo, Y.; Lu, Y.; Xie, Z., Oncolytic adenovirus programmed by synthetic gene circuit for cancer immunotherapy. *Nat Commun* **2019,** *10* (1), 4801.

31. Guo, L.; Hu, C.; Liu, Y.; Chen, X.; Song, D.; Shen, R.; Liu, Z.; Jia, X.; Zhang, Q.; Gao, Y.; Deng, Z.; Zuo, T.; Hu, J.; Zhu, W.; Cai, J.; Yan, G.; Liang, J.; Lin, Y., Directed natural evolution generates a next-generation oncolytic virus with a high potency and safety profile. *Nat Commun* **2023,** *14* (1), 3410.

32. Das, K.; Belnoue, E.; Rossi, M.; Hofer, T.; Danklmaier, S.; Nolden, T.; Schreiber, L. M.; Angerer, K.; Kimpel, J.; Hoegler, S.; Spiesschaert, B.; Kenner, L.; von Laer, D.; Elbers, K.; Derouazi, M.; Wollmann, G., A modular self-adjuvanting cancer vaccine combined with an oncolytic vaccine induces potent antitumor immunity. *Nat Commun* **2021,** *12* (1), 5195.

33. Medina-Echeverz, J.; Hinterberger, M.; Testori, M.; Geiger, M.; Giessel, R.; Bathke, B.; Kassub, R.; Grabnitz, F.; Fiore, G.; Wennier, S. T.; Chaplin, P.; Suter, M.; Hochrein, H.; Lauterbach, H., Synergistic cancer immunotherapy combines MVA-CD40L induced innate and adaptive immunity with tumor targeting antibodies. *Nat Commun* **2019,** *10* (1), 5041.

34. Atasheva, S.; Emerson, C. C.; Yao, J.; Young, C.; Stewart, P. L.; Shayakhmetov, D. M., Systemic cancer therapy with engineered adenovirus that evades innate immunity. *Sci Transl Med* **2020,** *12* (571), eabc6659. DOI: 10.1126/scitranslmed.abc6659.

35. Evgin, L.; Kottke, T.; Tonne, J.; Thompson, J.; Huff, A. L.; van Vloten, J.; Moore, M.; Michael, J.; Driscoll, C.; Pulido, J.; Swanson, E.; Kennedy, R.; Coffey, M.; Loghmani, H.; Sanchez-Perez, L.; Olivier, G.; Harrington, K.; Pandha, H.; Melcher, A.; Diaz, R. M.; Vile, R. G., Oncolytic virus-mediated expansion of dual-specific CAR T cells improves efficacy against solid tumors in mice. *Sci Transl Med* **2022,** *14* (640), eabn2231. DOI: 10.1126/scitranslmed.abn2231.

36. Kennedy, E. M.; Denslow, A.; Hewett, J.; Kong, L.; De Almeida, A.; Bryant, J. D.; Lee, J. S.; Jacques, J.; Feau, S.; Hayes, M.; McMichael, E. L.; Wambua, D.; Farkaly, T.; Rahmeh, A. A.; Herschelman, L.; Douglas, D.; Spinale, J.; Adhikari, S.; Deterling, J.; Scott, M.; Haines, B. B.; Finer, M. H.; Ashburn, T. T.; Queva, C.; Lerner, L., Development of intravenously administered synthetic RNA virus immunotherapy for the treatment of cancer. *Nat Commun* **2022,** *13* (1), 5907.

37. Niemann, J.; Woller, N.; Brooks, J.; Fleischmann-Mundt, B.; Martin, N. T.; Kloos, A.; Knocke, S.; Ernst, A. M.; Manns, M. P.; Kubicka, S.; Wirth, T. C.; Gerardy-Schahn, R.; Kuhnel, F., Molecular retargeting of antibodies converts immune defense against oncolytic viruses into cancer immunotherapy. *Nat Commun* **2019,** *10* (1), 3236.

38. Svensson-Arvelund, J.; Cuadrado-Castano, S.; Pantsulaia, G.; Kim, K.; Aleynick, M.; Hammerich, L.; Upadhyay, R.; Yellin, M.; Marsh, H.; Oreper, D.; Jhunjhunwala, S.; Moussion, C.; Merad, M.; Brown, B. D.; Garcia-Sastre, A.; Brody, J. D., Expanding cross-presenting dendritic cells enhances oncolytic virotherapy and is critical for long-term anti-tumor immunity. *Nat Commun* **2022,** *13* (1), 7149.

39. Xu, B.; Tian, L.; Chen, J.; Wang, J.; Ma, R.; Dong, W.; Li, A.; Zhang, J.; Antonio Chiocca, E.; Kaur, B.; Feng, M.; Caligiuri, M. A.; Yu, J., An oncolytic virus expressing a full-length antibody enhances antitumor innate immune response to glioblastoma. *Nat Commun* **2021,** *12* (1), 5908.

40. Wang, S.; Yan, W.; Kong, L.; Zuo, S.; Wu, J.; Zhu, C.; Huang, H.; He, B.; Dong, J.; Wei, J., Oncolytic viruses engineered to enforce cholesterol efflux restore tumor-associated macrophage phagocytosis and anti-tumor immunity in glioblastoma. *Nat Commun* **2023,** *14* (1), 4367.

41. Nakao, S.; Arai, Y.; Tasaki, M.; Yamashita, M.; Murakami, R.; Kawase, T.; Amino, N.; Nakatake, M.; Kurosaki, H.; Mori, M.; Takeuchi, M.; Nakamura, T., Intratumoral expression of IL-7 and IL-12 using an oncolytic virus increases systemic sensitivity to immune checkpoint blockade. *Sci Transl Med* **2020,** *12* (526), eaax7992. DOI: 10.1126/scitranslmed.aax7992.

42. Liu, Z.; Ge, Y.; Wang, H.; Ma, C.; Feist, M.; Ju, S.; Guo, Z. S.; Bartlett, D. L., Modifying the cancer-immune set point using vaccinia virus expressing re-designed interleukin-2. *Nat Commun* **2018,** *9* (1), 4682.

43. Wang, G.; Kang, X.; Chen, K. S.; Jehng, T.; Jones, L.; Chen, J.; Huang, X. F.; Chen, S. Y., An engineered oncolytic virus expressing PD-L1 inhibitors activates tumor neoantigen-specific T cell responses. *Nat Commun* **2020,** *11* (1), 1395.

44. Rivadeneira, D. B.; DePeaux, K.; Wang, Y.; Kulkarni, A.; Tabib, T.; Menk, A. V.; Sampath, P.; Lafyatis, R.; Ferris, R. L.; Sarkar, S. N.; Thorne, S. H.; Delgoffe, G. M., Oncolytic Viruses Engineered to Enforce Leptin Expression Reprogram Tumor-Infiltrating T Cell Metabolism and Promote Tumor Clearance. *Immunity* **2019,** *51* (3), 548-560.

45. Bommareddy, P. K.; Aspromonte, S.; Zloza, A.; Rabkin, S. D.; Kaufman, H. L., MEK inhibition enhances oncolytic virus immunotherapy through increased tumor cell killing and T cell activation. *Sci Transl Med* **2018,** *10* (471), eaau0417. DOI: 10.1126/scitranslmed.aau0417.

46. Russell, L.; Swanner, J.; Jaime-Ramirez, A. C.; Wang, Y.; Sprague, A.; Banasavadi-Siddegowda, Y.; Yoo, J. Y.; Sizemore, G. M.; Kladney, R.; Zhang, J.; Lehman, N. L.; Ostrowski, M. C.; Hong, B.; Caligiuri, M.; Yu, J.; Kaur, B., PTEN expression by an oncolytic herpesvirus directs T-cell mediated tumor clearance. *Nat Commun* **2018,** *9* (1), 5006.

47. Wu, A.; Li, Z.; Wang, Y.; Chen, Y.; Peng, J.; Zhu, M.; Li, Y.; Song, H.; Zhou, D.; Zhang, C.; Lv, Y.; Zhao, Z., Recombinant measles virus vaccine rMV-Hu191 exerts an oncolytic effect on esophageal squamous cell carcinoma via caspase-3/GSDME-mediated pyroptosis. *Cell Death Discov* **2023,** *9* (1), 171.

48. Tian, L.; Xu, B.; Chen, Y.; Li, Z.; Wang, J.; Zhang, J.; Ma, R.; Cao, S.; Hu, W.; Chiocca, E. A.; Kaur, B.; Caligiuri, M. A.; Yu, J., Specific targeting of glioblastoma with an oncolytic virus expressing a cetuximab-CCL5 fusion protein via innate and adaptive immunity. *Nat Cancer* **2022,** *3* (11), 1318-1335.

49. Ji, D.; Zhang, Y.; Sun, J.; Zhang, B.; Ma, W.; Cheng, B.; Wang, X.; Li, Y.; Mu, Y.; Xu, H.; Wang, Q.; Zhang, C.; Xiao, S.; Zhang, L.; Zhou, D., An engineered influenza virus to deliver antigens for lung cancer vaccination. *Nat Biotechnol* **2024,** *42* (3), 518-528.

50. Fusciello, M.; Fontana, F.; Tahtinen, S.; Capasso, C.; Feola, S.; Martins, B.; Chiaro, J.; Peltonen, K.; Ylosmaki, L.; Ylosmaki, E.; Hamdan, F.; Kari, O. K.; Ndika, J.; Alenius, H.; Urtti, A.; Hirvonen, J. T.; Santos, H. A.; Cerullo, V., Artificially cloaked viral nanovaccine for cancer immunotherapy. *Nat Commun* **2019,** *10* (1), 5747.

51. Roy, D. G.; Geoffroy, K.; Marguerie, M.; Khan, S. T.; Martin, N. T.; Kmiecik, J.; Bobbala, D.; Aitken, A. S.; de Souza, C. T.; Stephenson, K. B.; Lichty, B. D.; Auer, R. C.; Stojdl, D. F.; Bell, J. C.; Bourgeois-Daigneault, M. C., Adjuvant oncolytic virotherapy for personalized anti-cancer vaccination. *Nat Commun* **2021,** *12* (1), 2626.

52. D'Alise, A. M.; Leoni, G.; Cotugno, G.; Troise, F.; Langone, F.; Fichera, I.; De Lucia, M.; Avalle, L.; Vitale, R.; Leuzzi, A.; Bignone, V.; Di Matteo, E.; Tucci, F. G.; Poli, V.; Lahm, A.; Catanese, M. T.; Folgori, A.; Colloca, S.; Nicosia, A.; Scarselli, E., Adenoviral vaccine targeting multiple neoantigens as strategy to eradicate large tumors combined with checkpoint blockade. *Nat Commun* **2019,** *10* (1), 2688.

53. Ring, S. S.; Cupovic, J.; Onder, L.; Lutge, M.; Perez-Shibayama, C.; Gil-Cruz, C.; Scandella, E.; De Martin, A.; Morbe, U.; Hartmann, F.; Wenger, R.; Spiegl, M.; Besse, A.; Bonilla, W. V.; Stemeseder, F.; Schmidt, S.; Orlinger, K. K.; Krebs, P.; Ludewig, B.; Flatz, L., Viral vector-mediated reprogramming of the fibroblastic tumor stroma sustains curative melanoma treatment. *Nat Commun* **2021,** *12* (1), 4734.

54. Smith, R.; Wafa, E. I.; Geary, S. M.; Ebeid, K.; Alhaj-Suliman, S. O.; Salem, A. K., Cationic nanoparticles enhance T cell tumor infiltration and antitumor immune responses to a melanoma vaccine. *Sci Adv* **2022,** *8* (29), eabk3150. DOI: 10.1126/sciadv.abk3150.

55. Mosaheb, M. M.; Dobrikova, E. Y.; Brown, M. C.; Yang, Y.; Cable, J.; Okada, H.; Nair, S. K.; Bigner, D. D.; Ashley, D. M.; Gromeier, M., Genetically stable poliovirus vectors activate dendritic cells and prime antitumor CD8 T cell immunity. *Nat Commun* **2020,** *11* (1), 524.

56. Lek, A.; Wong, B.; Keeler, A.; Blackwood, M.; Ma, K.; Huang, S.; Sylvia, K.; Batista, A. R.; Artinian, R.; Kokoski, D.; Parajuli, S.; Putra, J.; Carreon, C. K.; Lidov, H.; Woodman, K.; Pajusalu, S.; Spinazzola, J. M.; Gallagher, T.; LaRovere, J.; Balderson, D.; Black, L.; Sutton, K.; Horgan, R.; Lek, M.; Flotte, T., Death after High-Dose rAAV9 Gene Therapy in a Patient with Duchenne's Muscular Dystrophy. *N Engl J Med* **2023,** *389* (13), 1203-1210.

57. Ganeshan, K.; Nikkanen, J.; Man, K.; Leong, Y. A.; Sogawa, Y.; Maschek, J. A.; Van Ry, T.; Chagwedera, D. N.; Cox, J. E.; Chawla, A., Energetic Trade-Offs and Hypometabolic States Promote Disease Tolerance. *Cell* **2019,** *177* (2), 399-413.

58. Saxena, M.; Van, T. T. H.; Baird, F. J.; Coloe, P. J.; Smooker, P. M., Pre-existing immunity against vaccine vectors--friend or foe? *Microbiology* **2013,** *159* (Pt 1), 1-11.

59. Wang, W. C.; Sayedahmed, E. E.; Mittal, S. K., Significance of Preexisting Vector Immunity and Activation of Innate Responses for Adenoviral Vector-Based Therapy. *Viruses* **2022,** *14* (12), 2727.

60. Glorioso, J. C.; Cohen, J. B.; Goins, W. F.; Hall, B.; Jackson, J. W.; Kohanbash, G.; Amankulor, N.; Kaur, B.; Caligiuri, M. A.; Chiocca, E. A.; Holland, E. C.; Queva, C., Oncolytic HSV Vectors and Anti-Tumor Immunity. *Curr Issues Mol Biol* **2021,** *41*, 381-468.

61. Shaw, A. R.; Suzuki, M., Immunology of Adenoviral Vectors in Cancer Therapy. *Mol Ther Methods Clin Dev* **2019,** *15*, 418-429.

62. Augusto, D. G.; Murdolo, L. D.; Chatzileontiadou, D. S. M.; Sabatino, J. J., Jr.; Yusufali, T.; Peyser, N. D.; Butcher, X.; Kizer, K.; Guthrie, K.; Murray, V. W.; Pae, V.; Sarvadhavabhatla, S.; Beltran, F.; Gill, G. S.; Lynch, K. L.; Yun, C.; Maguire, C. T.; Peluso, M. J.; Hoh, R.; Henrich, T. J.; Deeks, S. G.; Davidson, M.; Lu, S.; Goldberg, S. A.; Kelly, J. D.; Martin, J. N.; Vierra-Green, C. A.; Spellman, S. R.; Langton, D. J.; Dewar-Oldis, M. J.; Smith, C.; Barnard, P. J.; Lee, S.; Marcus, G. M.; Olgin, J. E.; Pletcher, M. J.; Maiers, M.; Gras, S.; Hollenbach, J. A., A common allele of HLA is associated with asymptomatic SARS-CoV-2 infection. *Nature* **2023,** *620* (7972), 128-136.

Chapter 2 Inducing Long Lasting B Cell and T Cell Immunity Against Multiple Variants of SARS-CoV-2 Through Mutant Bacteriophage Qβ – Receptor Binding Domain Conjugate

2.1 Introduction

The severe acute respiratory syndrome coronavirus 2 (SARS-CoV-2), the causative agent of the coronavirus disease 2019 (COVID-19), poses a serious threat to public health. As of October 2022, it caused over 6 million deaths worldwide. The Institute for Health Metrics and Evaluation estimated more than 18 million mortalities during 2020 and 2021 related to COVID-19 globally, far surpassing the reported numbers.[1] Anti-COVID-19 vaccines based on messenger RNA (mRNA),[2, 3] protein subunits,[4-7] adenovirus carrier[8-10] or inactivated SARS-CoV-2 virion particles[11, 12] have been developed, which have drastically reduced the rates of hospitalization, severe disease and death. However, there are significant limitations to the currently approved vaccines. The viruses have acquired significant mutations over the past two years with five variants of concern (VOCs), namely Alpha, Beta, Gamma, Delta and Omicron being declared by the World Health Organization (WHO) by spring 2023. These VOCs are more resistant to neutralization by monoclonal antibodies,[13-20] vaccinated or convalescent sera,[14, 17, 19-23] leading to frequent infections even in fully vaccinated[24, 25] or convalescent[22] people. On September 11, 2023, FDA amended the emergency use authorization (EUA) of Moderna and Pfizer COVID-19 Vaccine to include the updated formula that covers the dominate strain XBB.1.5 at the time. After less than half a year, the dominate strain became JN.1 meanwhile the popularity of linage XBB dropped to less than 1% on January 2024. (https://covid.cdc.gov/covid-data-tracker/#variant-proportions, accessed by

April 30th, 2024) The fast evolving nature of SARS-CoV-2 highlights the need to development of a broad spectrum vaccine. Furthermore, the immunity elicited through vaccination can wane rapidly.[26-29] In a large scale study of 2,653 people fully immunized with the Pfizer/BioNTech BNT162b2 mRNA vaccines, anti-Spike (S) protein IgG antibody titers decreased by up to 38% each month after immunization.[30] In another study involving 22,657 patients, for those infected with SARS-CoV-2 after being vaccinated with the Pfizer/BioNTech mRNA vaccine, the reduction of viral load as a result of vaccination became insignificant 6 months after the 2nd dose compared to the non-vaccinees, and the regained protection from the 3rd immunization became insignificant again in 2-4 months.[26] To compensate the fast wanning immunity induced by the current vaccines, frequent boosts is required, which creates challenge to supply chains and requires public compliance. SARS-CoV-2 majorly infects human via the respiratory epithelium. Mucosal antibodies and immune cells are the first line defense to the infection. A functional mucosal response has the potential to neutralize the viral particles before they enter the epithelium and reduce human-to-human transmission. Current vaccines lack the ability to effectively boost mucosal immunity in the human respiratory track. A recent study found that in the bronchoalveolar lavage fluid (BALF) of people vaccinated by 2 or 3 doses of the mRNA vaccine, little SARS-CoV-2 Spike-specific B and T cells were observed. Levels of neutralizing antibodies against D614G, Delta and Omicron variants in the BALF were significantly lower than those of convalescent patients despite robust antibody responses in blood induced by vaccines.[31] Thus, new vaccines that

can induce *broadly neutralizing, persistent, and comprehensive* immunity are urgently needed to enhance the protection against SARS-CoV-2.

The glycoprotein S, one of the surface components of the virus, is a major target of host immunity.[32, 33] S plays a critical role during the cellular entry by the virus, which is initiated through the recognition of cell surface receptor human angiotensin converting enzyme 2 (hACE2) by the receptor binding domain (RBD) of S.[34-36] The RBD is an attractive target for vaccine development.[37] However, efforts are needed to better determine the protective epitopes from the RBD and to boost the immune responses against SARS-CoV-2. Herein, we report that the epitope selection for RBD based vaccines is critical. A range of RBD peptides/glycopeptides and the glycosylated full-length RBD have been evaluated as a potential antigen. The full-length RBD has been found to be the most suitable antigen. The conjugate of the RBD with a promising protein carrier, bacteriophage mutant Qβ (mQβ), gave the highest levels of persistent IgG antibodies capable of neutralizing viruses including the VOCs. Furthermore, the mQβ-RBD conjugate elicited CD4$^+$ and CD8$^+$ T cell responses against SARS-CoV-2 including the Omicron variant.

2.2 Results and discussion

2.2.1 Conjugates of peptide/glycopeptide epitopes from the RBD failed to produce high levels of antibodies recognizing the RBD

A critical factor in conjugate vaccine design is epitope selection. Our initial efforts focused on peptide/glycopeptide epitopes from the RBD as their structures can be well-defined. From the cryo-EM structures of the complexes formed by the RBD (from the Wuhan-Hu-1 reference strain)

with the human ACE-2 protein or with several broadly neutralizing antibodies,[38-41] we selected a panel of RBD peptides and glycopeptides (**Table 2.1**) as potential epitopes based on high solvent accessibility, high B cell antigenicity prediction scores, and sequences within the RBD recognized by neutralizing antibodies.[42, 43]

To enhance antibody responses to the (glyco)peptides, mutant bacteriophage Qβ VLPs[43] have been utilized as the immunogenic carrier to deliver the epitopes. Bacteriophage Qβ capsid protein (CP) can be expressed recombinantly in *E. coli* cells to form VLPs with 180 copies of CPs arranged in a 28 nm diameter, icosahedral particle. Each CP allows up to 4 solvent accessible lysine residues on the exterior, which can provide the reactive sites enabling polyvalent bioconjugation.[44] With its high order of symmetry and optimal antigen presentation density, Qβ has been shown to significantly enhance antibody responses against conjugated subunit epitopes.[43, 45-49] Furthermore, a Qβ mutant (mQβ), A38K/A40C/D102C, was shown superior to wild type Qβ as a vaccine carrier further to enhance the antibody responses to the conjugated antigen while reducing the levels of antibodies generated against the carrier itself.[43]

Entry	Location	Sequence
1	407-428	CVRQIAPGQTGKIADYNYKLPDD
2	473-491	YQAGSTPCNGVEGFNCYFP
3	439-447	CNNLDSKVGG
4	495-507	CYGFQPTNGVGYQ
5	453-460	CYRLFRKSN
6	319-326	CRVQPT(α-Tf)ESI
7	336-346	CPFGEVFN(GlcNAc)ATR
8	336-346	CPFGEVFN(FucGlcNAc)ATR
9	484-518	EGFNCYFPLQSYGFQPTNGVGYQPYRVVVLSFELL
10	488-508	CYFPLQSYGFQPTNGVGYQPY
11	440-460	CNLDSKVGGNYNYLYRLFRKSN

Table 2.1 Panel of selected peptide or glycopeptide epitopes investigated in the current study. C shown in red indicated cysteine added to the sequences for bioconjugation. Underlined C represented cysteine residues connected by disulfide bond.

All peptides and glycopeptides were synthesized and conjugated with mQβ (**Scheme 2.1**), averaging 150-250 copies of the peptide/glycopeptide per mQβ particle. To evaluate the antigenicity of these conjugates, mice were immunized with each construct and monophosphoryl lipid A (MPLA) as the adjuvant on days 0, 14 and 28. Sera were collected on day 35 following the initial immunization. Enzyme Linked Immunosorbent Assay (ELISA) was first carried out using the corresponding conjugate of bovine serum albumin (BSA) and the (glyco)peptide to avoid interference from anti-mQβ antibodies. Concentration at half maximum effectiveness (EC50) titer values, the highest fold of dilution to retain more than 50% of the highest optical density values in ELISA, were calculated as the titer numbers. As shown in **Figure 2.1a**, all constructs elicited high levels of IgG antibodies against the respective immunizing antigen (geometrical mean of titer (GMT) 54,745 - 146,102), which suggests mQβ conjugates can boost the antibody responses

41

against the RBD (glyco)peptides. As an effective vaccine, it is critical that antibodies elicited can recognize the native RBD. To test this, another ELISA was set up using the full length RBD as the coating antigen. Interestingly, despite the high levels of anti-(glyco)peptide IgG antibodies produced by all 11 mQβ-(glyco)peptide conjugates **Figure 2.1a**), only mQβ-peptide **1** and mQβ-peptide **2** induced significant (GMT >1,000) IgG antibodies capable of recognizing the full length RBD (**Figure 2.1b**). This suggests that antigen design needs to be improved.
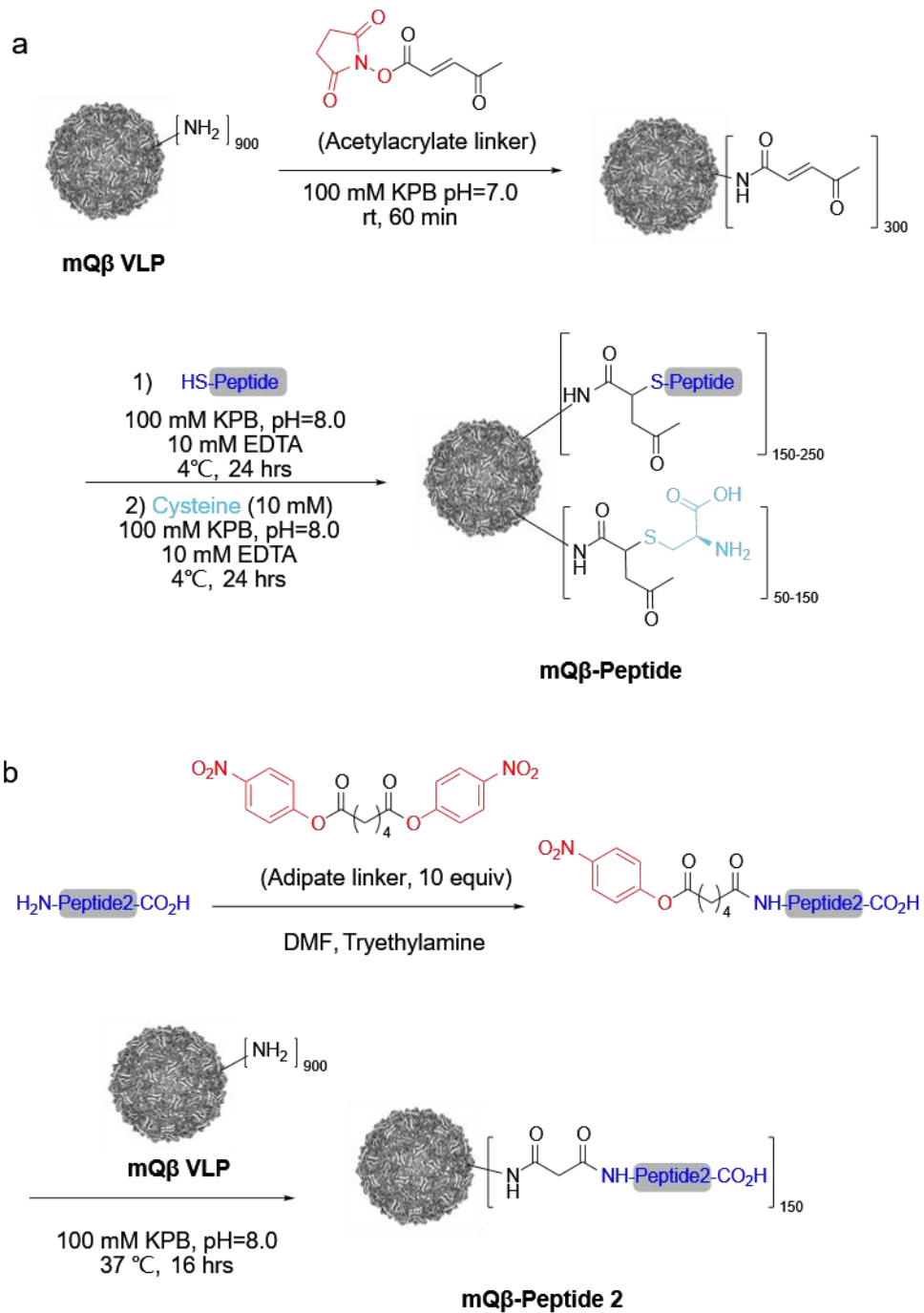
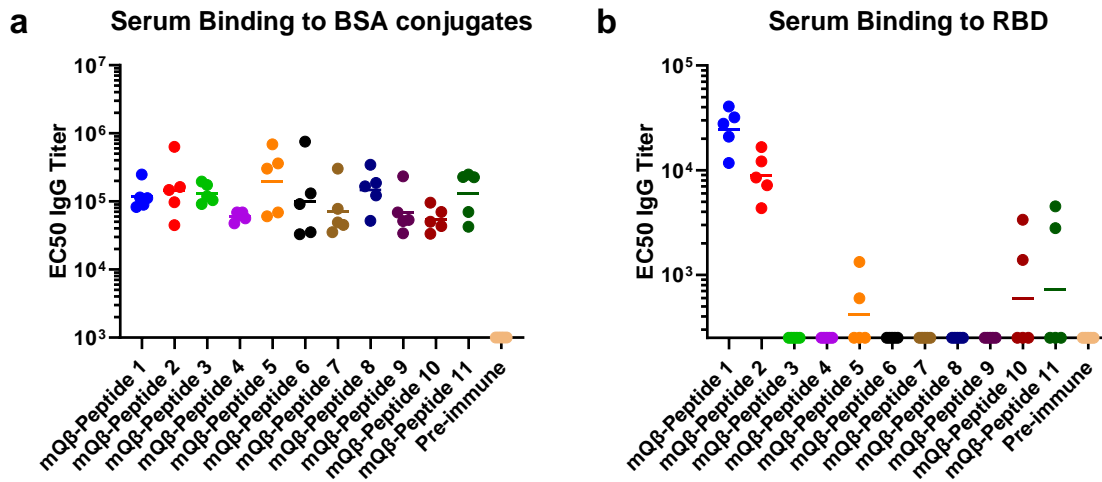**Scheme 2.1** Synthesis of mQβ-peptide/glycopeptide conjugates.

Figure 2.1 Immune response against mQβ-(glyco)peptide conjugates. EC50 IgG antibody titers against **a)** BSA-(glyco)peptide conjugates and **b)** RBD were plotted. Female C57BL/6 mice aged 6 weeks (n=5) were immunized with various (glyco)peptide conjugates on day 0, 14 and 28 subcutaneously under the scruff. Each dose contained equivalent of 8 nmol of (glyco)peptides, along with 20 µg MPLA. Serum samples were collected by day 35 and ELISA was run against a) (glyco)peptide BSA conjugates or b) full length RBD. Serum IgG titers were calculated to represent the dilution that gave half-maximal absorbance (GraphPad Prism 6, 4 PL nonlinear regression, least squares). While high levels of anti-(glyco)peptide IgG antibodies were produced by all 11 mQβ-(glyco)peptide conjugates, only mQβ-peptide **1** and mQβ-peptide **2** induced significant IgG antibodies capable of recognizing the full length RBD. Each symbol presented an individual mouse. Short horizontal bar in between the dots indicated the geometrical mean of the group. Limit of detection was 1,000 ELISA units in a) and 250 ELISA units in b), respectively. Dots on horizontal axis presented mice without detectable binding.

2.2.2 Design and synthesis of conjugates of mQβ with the full-length RBD

As an alternative to the (glyco)peptide antigens, we explored next the possibility of applying the full length RBD as the antigen. As the free RBD may be insufficiently immunogenic (*vide infra*) and the fusion of RBD with the mQβ coat protein may affect the mQβ assembly into nanoparticles, the chemical conjugation of RBD with mQβ was investigated. To produce antibodies capable of blocking RBD and hACE-2 interactions, we hypothesize that the RBD

should be oriented on mQβ in a way that its receptor binding motif (RBM) involved in hACE-2 binding is pointing away from the mQβ surface to enable its recognition by B cells for antibody generation *in vivo*. Examination of the structure formed by the complex of RBD with hACE-2[40] (**Figure 2.2**) and ectodomain of S[50] showed that of the 9 cysteine residues in the RBD sequence (R319-F541), 8 of which are paired as disulfides. The only free cysteine C538 (shown in purple) resides at the C terminus of the RBD, which is situated at the opposite side from the hACE2-RBD recognition interface.[40] Thus, we envision that conjugation of this RBD sequence through C538 will display RBD in a suitable orientation for the generation of neutralizing antibodies targeting residues at the interface between RBD and hACE-2.
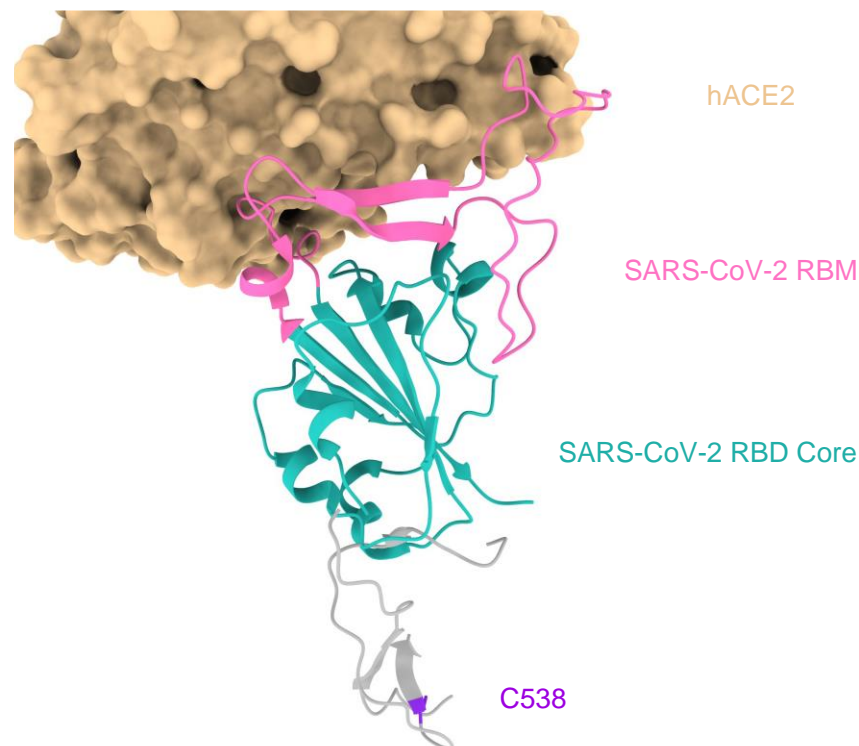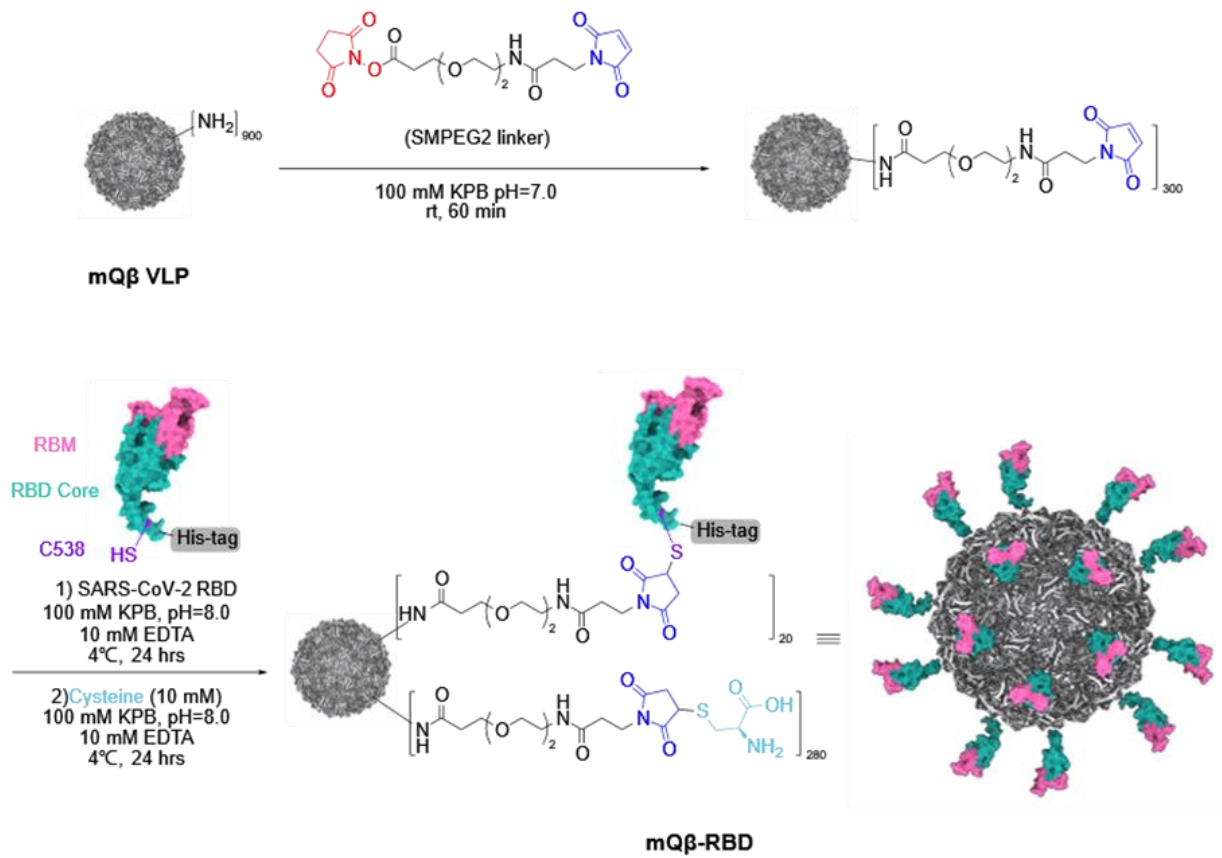

Figure 2.2 Cryo-EM structure of the hACE2-RBD complex, recreated based on PDB ID 6M17[40] using Chimera X 1.3.[51] Unsolved structure of the C- and N-terminus of RBD is estimated based

on cryo-EM structure of ectodomain S from PDB ID 6XR8[50] and displayed in grey. RBD is a rigid and stable cage-like domain that consists of a surface loop RBM (shown in pink) for receptor (shown in tan) engagement and a β sheet-enriched core (shown in light blue) for stabilization. The only free thiol-containing cysteine residue (C538) used for conjugation is shown in purple.

In order to conjugate the two macromolecules, mQβ VLPs were functionalized with a flexible thiol-reactive linker SMPEG2 (**Scheme 2.2**). The RBD (R319-F541) was expressed in expi293 cells with a C-terminus His-tag with the yield of 20 mg/L, which was subsequently incubated with SMPEG2 functionalized mQβ. The mQβ-RBD conjugate was purified via size exclusion chromatography (SEC) with the unreacted maleimide moieties on mQβ capped with cysteine. Based on the amount of the RBD consumed, the average loading of the RBD was determined to be 20 copies per particle. Dynamic light scattering (DLS) (**Figure 2.3**) and SEC (**Figure 2.4**) showed slight increases in particle size of the conjugate compared to unfunctionalized mQβ suggesting successful conjugation.

Scheme 2.2 Synthesis of the mQβ-RBD conjugate.

a Size Distribution by Intensity

b

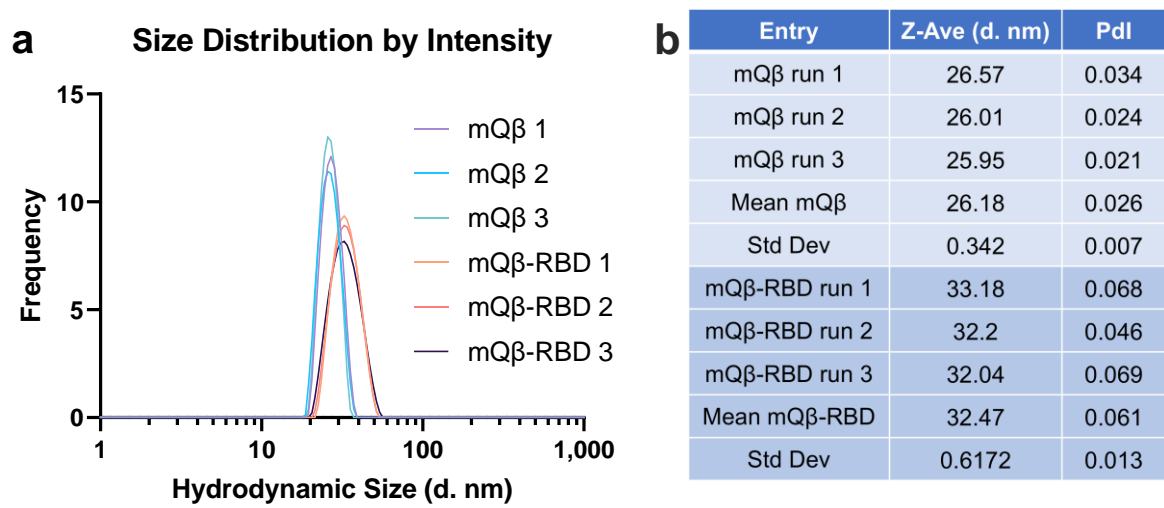| Entry	Z-Ave (d. nm)	PdI
mQβ run 1	26.57	0.034
mQβ run 2	26.01	0.024
mQβ run 3	25.95	0.021
Mean mQβ	26.18	0.026
Std Dev	0.342	0.007
mQβ-RBD run 1	33.18	0.068
mQβ-RBD run 2	32.2	0.046
mQβ-RBD run 3	32.04	0.069
Mean mQβ-RBD	32.47	0.061
Std Dev	0.6172	0.013

Figure 2.3 Size characterization of the conjugate vaccine. **a)** DLS size distribution of mQβ before and after RBD conjugation. Each curve presented a measurement. **b)** The summary of the measurements.
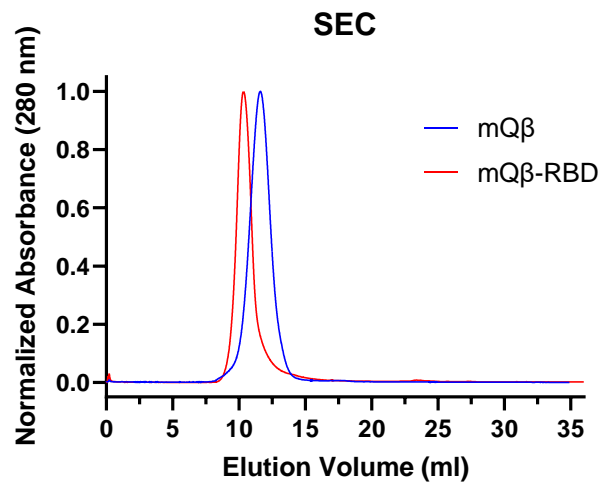

Figure 2.4 SEC traces of mQβ before and after RBD conjugation.

To validate that the RBD on mQβ-RBD conjugate can be recognized by its receptor, we used the ELISA assay. ELISA wells were coated with the mQβ-RBD conjugate and the free RBD, respectively. An hACE2-human IgG1 Fc chimera protein was added to the wells. Upon removing the unbound protein, the amounts of hACE2-Fc retained in the wells were quantified by horseradish peroxidase (HRP) conjugated secondary antibody against human IgG Fc. A significant increase (~2 fold, as calculated by the horizontal distance between the two curves) in recognition of mQβ-RBD by hACE2 was observed compared to wells containing an equivalent amount of the free RBD (**Figure 2.5a**). On the other hand, His-tag in the C terminus close to the conjugation site was recognized less by an anti His-tag 2nd antibody with a significantly lower (~3 fold) binding to the C-terminus His-tag of the conjugated RBD compared to the free RBD observed (**Figure 2.5b**). These results confirmed that the RBD was successfully conjugated to the mQβ with its RBM exposed for biological recognition.
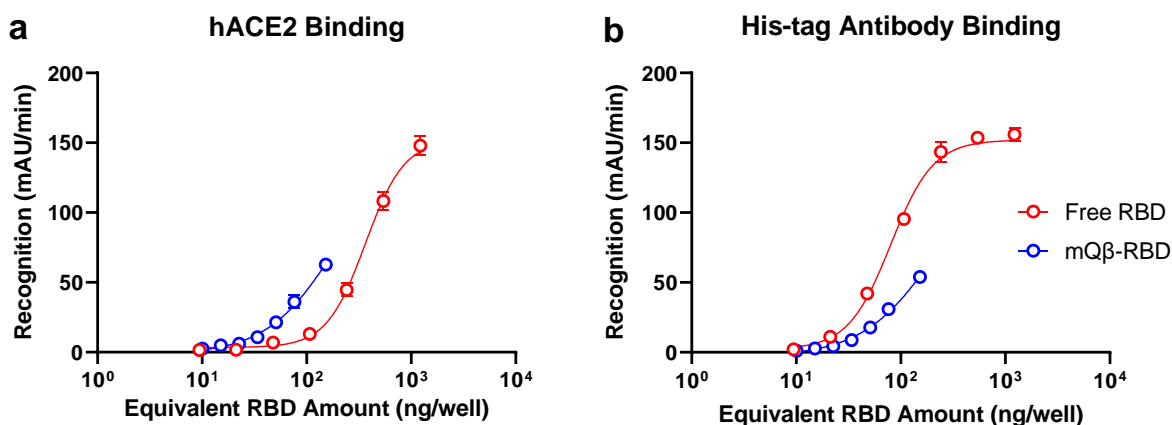

Figure 2.5 Kinetic ELISA measuring the accessibility of **a)** RBM and **b)** c-terminus His-tag on mQβ-RBD. Comparison was made between mQβ-RBD and free RBD in recognition by **a)** hACE2 or **b)** anti His-tag antibody. RBD conjugated on mQβ showed a ~2-fold increase in hACE2

recognition and a ~3-fold reduction in anti His-tag antibody recognition comparing to equivalent amount of free RBD.

2.2.3 mQβ-RBD conjugate is highly immunogenic leading to high levels of IgG antibodies that recognize the RBD

To test the immunogenicity of the mQβ-RBD conjugate, we immunized C57BL/6 mice with the mQβ-RBD conjugate (10 µg of RBD) and MPLA as the adjuvant following the aforementioned biweekly immunization schedule of one prime and two boosters. Using the identical immunization protocol, three control groups of mice were injected with 1) free RBD; 2) admixture of RBD with mQβ; 3) a RBD conjugate with a gold standard protein carrier, CRM-197, synthesized by the same conjugation chemistry as for mQβ-RBD, respectively at the equivalent amounts of RBD and MPLA. On day 0 prior to immunization and day 35 after the first immunization, sera were collected from all groups of mice and EC50 titers of IgG antibodies against the RBD were determined by ELISA. In addition, human convalescent sera (HCS) from 20 patients recovered from SARS-CoV-2 infections were obtained and screened for RBD binding via ELISA (**Figure 2.6**). Five patient HCS samples with the highest RBD recognition were selected and added to ELISA for a comparison with the immunized sera from mice (**Figure 2.7a**).
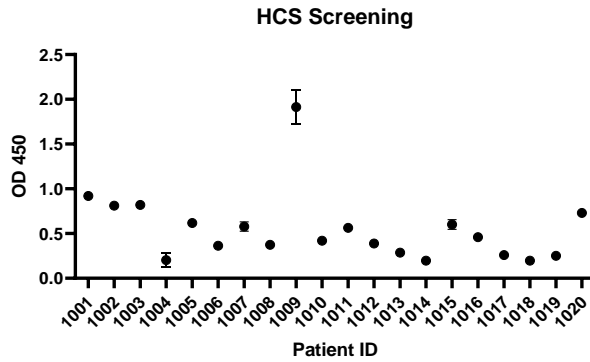
Figure 2.6 ELISA screening for HCS samples. All sera were diluted 1: 20,000 in PBS containing 0.1% BSA and reacted with immobilized RBD. Bound serum antibodies were analyzed by secondary antibody against human IgG. Samples 1001, 1002, 1003, 1009 and 1020 were used in later studies. Sample 1009 was used in PSV and live virus neutralization as it contained high levels of anti-RBD antibodies.
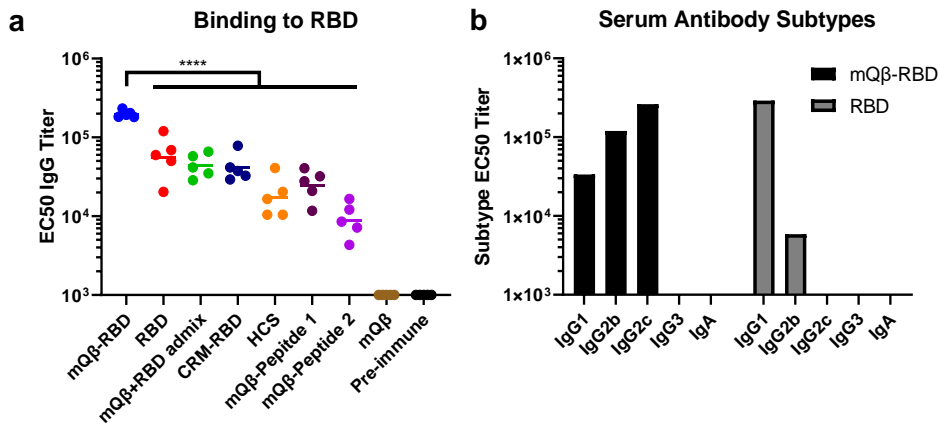

Figure 2.7 mQβ-RBD conjugates showed superior immunogenicity in mice. **a)** Female C57BL/6 mice aged 6 weeks (n = 5) were immunized with different constructs on days 0, 14 and 28 subcutaneously under the scruff. Each dose contained the equivalent of 10 ug RBD or 8 nmol of peptides, along with 20 µg MPLA. Serum samples were collected by day 35 and ELISA was run against RBD to determine the EC50 IgG titers against RBD. Each symbol represented an individual mouse or human. The horizontal bar indicated the geometrical mean in the group. **b)** Subtypes of the serum antibodies induced by mQβ-RBD and free RBD. Pooled sera (n = 5) were used. The limit of detection in these assays was 1,000 ELISA units. Dots on the horizontal axis in **a)** and empty bars in **b)** indicated antibody titers below the detection limit. Statistical analysis was performed by comparing the mQβ-RBD group with every other group. ****, $p < 0.0001$, one-way ANOVA via GraphPad Prism.

51

The ELISA results showed that mice immunized with mQβ-RBD gave an anti-RBD IgG EC50 GMT of 198,153 ELISA units, while mQβ immunized mice produced anti-RBD titers below 1,000 on day 35 and the pre-immune sera did not exhibit significant anti-RBD antibody titers above background (**Figure 2.7a**). The EC50 titers from the mQβ+RBD admix group (GMT of 43,611 ELISA units) were comparable to those of the free RBD group (GMT 55,030 ELISA units), which were significantly lower than titers from the mQβ-RBD group. This indicates that the covalent conjugation between the mQβ and RBD was critical for high immune responses. The CRM-197-RBD group gave an anti-RBD EC50 IgG GMT of 41,039 ELISA units (**Figure 2.7a**). The higher tiers induced by mQβ-RBD highlight the superiority of mQβ as the vaccine carrier compared to the gold standard carrier protein CRM-197.

The subtypes of the antibodies were analyzed. IgG1, IgG2b and IgG2c were the main IgG subtypes from the mice immunized with mQβ-RBD, suggesting that both Th1 and Th2 responses were induced by mQβ-RBD. In comparison, the mice receiving the free RBD produced mainly IgG1 responses, indicating a Th2 biased response in these mice (**Figure 2.7b**). No IgG3 or IgA was observed in the sera.

2.2.4 mQβ-RBD induced antibodies have potent neutralizing activities

For an effective vaccine, the ability to induce neutralizing antibodies is critical to blocking the viral infection of host cells. The non-neutralizing antibodies may potentially induce inflammation and exacerbate symptoms and outcomes of infection.[52, 53] To determine the levels of neutralizing

antibodies, we adapted an ELISA based surrogate virus neutralization titer assay (sVNT),[54] by determining the NT50 titers, which are the maximum fold of serum dilutions capable of inhibiting 50% of RBD-hACE2 recognition. sVNT is a convenient assay to quantify the levels of neutralizing antibodies. The results have been validated to correlate well with the gold standard viral neutralization assay in clinic studies.[54, 55] As shown in **Figure 2.8a**, mQβ-RBD immunized mice exhibited NT50 titers with the GMT of 4,345 ELISA units, which were over 20 times higher than those receiving free RBD (GMT 198 ELISA units), RBD/mQβ admixture (GMT 169 ELISA units), or HCS (GMT 187 ELISA units). Consistent with the IgG titers, CRM-197-RBD conjugate also elicited significantly lower neutralization antibody levels than mQβ-RBD. The sera from mQβ-peptide **1** and mQβ-peptide **2** conjugate immunized mice had NT50 below 1% of those from mQβ-RBD immunized mice.

In order to evaluate the quality of the antibodies, or the relative abundance of neutralizing antibodies in all RBD-directed antibodies, the neutralizing to the binding ratio (N/B) was calculated for each mouse. As shown in **Figure 2.8b**, The N/B values of the mQβ-RBD group are significantly higher, suggesting mQβ-RBD not only induced a higher magnitude of anti-RBD IgG antibody response, but also produced higher quality antibodies with better neutralization abilities.

As SARS-CoV-2 is a respiratory virus, antibodies in the respiratory tract mucus that covers the epithelial layer are the first line of defense. To test if the vaccine induced neutralizing antibodies in the respiratory tract, we collected the BALF by washing the whole lung from

immunized mice and conducted sVNT assay with the mucus wash. Titers at half maximum

neutralization (NT50) showed a strong neutralization function in mouse lung mucus after

immunization by mQβ-RBD at a level (GMT 3,148 ELISA units) comparable to that found in sera

(GMT 4,345 ELISA units). In contrast, the free RBD induced no detectable neutralization function

in lung mucus from the mice (**Figure 2.8c**). Subtyping of antibodies from the mQβ-RBD

immunized mouse lung mucus showed a very similar profile as those found in the sera, except that

IgA antibodies were observed from the lung mucus in addition to IgG antibodies suggesting that

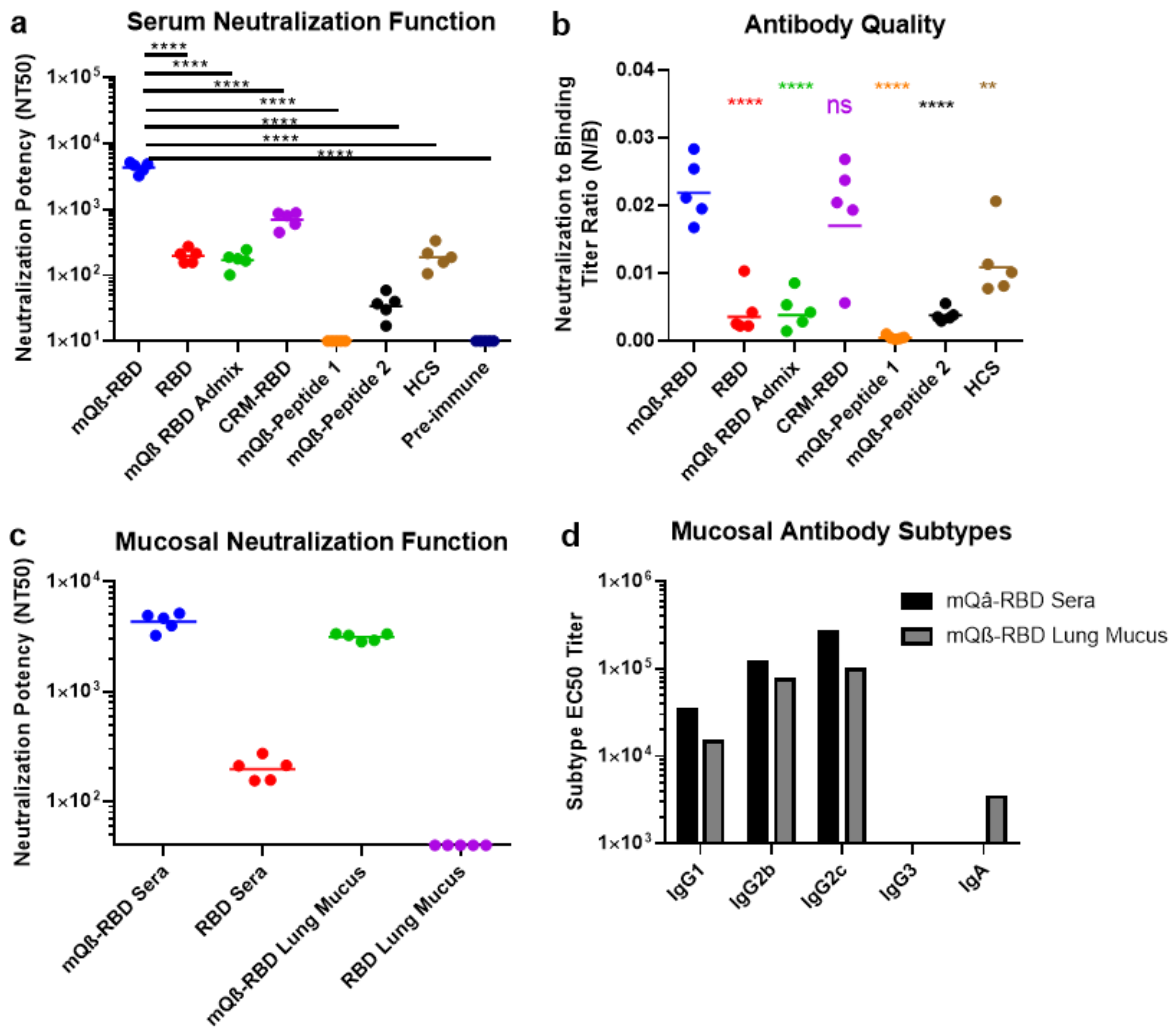mucosal immunity was induced through vaccination with mQβ-RBD (**Figure 2.8d**).

Figure 2.8 mQβ-RBD induced potently neutralizing antibodies in sera and respiratory tract mucus. **a)** Mouse sera on day 35 post immunization were tested in sVNT assay. Serially diluted sera were allowed to react with HRP-conjugated RBD and then added to an ELISA plate coated with the hACE-2-Fc chimera protein to capture non-neutralized RBD. Upon removal of non-captured RBD, colorimetric substrate 3,3',5,5'-tetramethybenzidine (TMB) was added to the plate after washing. The neutralization was determined by the percentage signal reduction compared to serum omitted wells with HRP-RBD omitted wells set as standards for 100% neutralization. NT50 titers were calculated to represent serum dilution fold to give 50% neutralization (GraphPad Prism 6, 4 PL nonlinear regression, least squares). **b)** Calculated N/B ratio of sVNT neutralization titer over its corresponding RBD recognition EC50 titer for each mouse. **c)** Immunized mice were euthanized by day 35 and the BALF was collected. Levels of neutralization antibodies in the BALF were evaluated by sVNT. **d)** Subtypes of mucosal antibodies in the BALF were compared to those observed in immune sera. For **a)**, **b)**, and **c)**, each symbol represented an individual mouse. The

horizontal bar indicated the geometrical mean in the group. The limit of detection for these assays was 10. Dots on the horizontal axis represented mice without detectable neutralization. For **d**), pooled sera (n = 5) were used. The limit of detection was 1,000 ELISA units. The empty bar indicated no binding detected. Statistical analysis was performed by comparing the mQβ-RBD group with every other group. ns, non-significant; **, $p < 0.01$; ***, $p < 0.001$; ****, $p < 0.0001$; one-way ANOVA analysis via GraphPad Prism 6.

2.2.5 Post-immune sera effectively neutralized S bearing pseudovirus and live SARS-CoV-2 virus infection of cells

To verify the neutralization function against viral particles, we constructed pseudovirions (PSVs) with SARS-CoV-2 S (S-PSV) based on envelope-deficient HIV reporter constructs encoding firefly luciferase (pNL-luc). Upon incubation of the S-PSVs with hACE-2 knockin HEK293 (hACE-2-HEK293) cells, the S-PSVs readily infected the cells as reflected by the high levels of bioluminescence from the wells following the addition of the luciferin substrate. As shown in **Figure 2.9**, when the S-PSVs were pre-incubated with sera from the mice immunized with mQβ-RBD, the sera were able to significantly reduce the S-PSV infection of hACE-2-HEK293 cells in a dose dependent manner. The NT50 value, i.e., the maximum fold of serum dilution that inhibited 50% of PSV infectivity, was determined to be 26,504. In comparison, NT50 values for sera from RBD immunized mice or HCS with the highest anti-RBD IgG titers were 10,252 and 2,674 respectively (**Figure 2.9a** and **d**). As a control, PSVs expressing the vesicular stomatitis virus glycoprotein (VSVg-PSV) were used. None of the post-immune sera inhibited VSVg-PSV infection of hACE-2-HEK293, suggesting that the inhibition of S-PSV was specifically due to antibody binding to S on the S-PSVs (**Figure 2.9c**). The higher NT50 observed

56

for the mQβ-RBD group correlated well with the higher levels of neutralization antibodies (**Figure 2.8a**) induced by mQβ-RBD immunization.

Next, we evaluated the abilities of post-immune sera to neutralize the live SARS-CoV-2 virus isolated from the clinic toward infection of hACE-2 expressing Vero E6 cells. When the virus was pre-incubated with HCS or sera from RBD immunized mice, a viral infection of Vero E6 cells could be inhibited at dilutions not higher than 320 or 40 folds, respectively. In contrast, with mQβ-RBD immune sera, the sera could be diluted up to 5,120 folds before losing their inhibitory activities against the SARS-CoV-2 virus (**Figure 2.9d**). These results indicated that neutralization activity of the sera from mQβ-RBD immunized mice against the clinical isolate is superior to neutralization activity from HCS or the free RBD immunized mice sera.
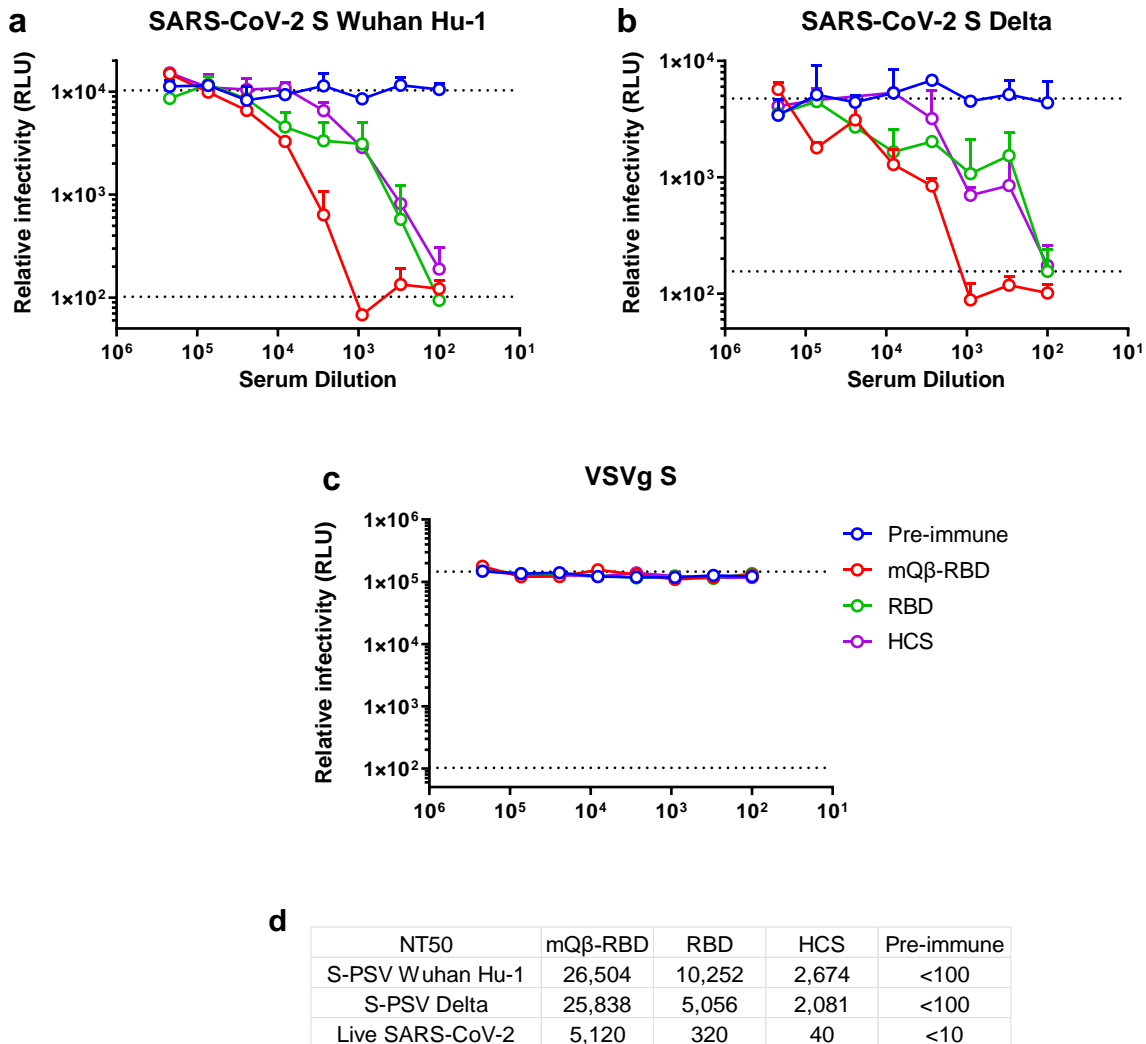
a SARS-CoV-2 S Wuhan Hu-1

b SARS-CoV-2 S Delta

c VSVg S

Legend:
- Pre-immune
- mQβ-RBD
- RBD
- HCS

d

NT50	mQβ-RBD	RBD	HCS	Pre-immune
S-PSV Wuhan Hu-1	26,504	10,252	2,674	<100
S-PSV Delta	25,838	5,056	2,081	<100
Live SARS-CoV-2	5,120	320	40	<10

Figure 2.9 mQβ-RBD immune sera inhibit SARS-CoV-2 viral infection *in vitro*. Lentivirus-based reporter PSVs containing **a)** SARS-CoV-2 Wuhan-Hu-1 reference strain S gene, **b)** Delta S gene or **c)** VSVg gene were generated in 293FT cells transfected with envelope-deficient HIV reporter constructs (pNL-luc). Purified PSVs were incubated with serially diluted mouse immune 35 days post priming or human convalescent sera at 37 °C for 1 hr. Next, 293FT cells overexpressing hACE2 were inoculated with the sera treated PSVs and incubated at 37 °C for 60 hrs. PSV infectivity was determined by measuring relative luminescence units (RLU). Pre-immune sera treated PSVs and mock infections were used as standards for 0% and 100% neutralization, as indicated by the top and button dashed lines, respectively. Percentage neutralization was fitted to serum dilution via 4PL nonlinear logistic method (GraphPad Prism 6, least squares). NT50 was calculated to present the dilution folds that blocked 50% infectivity relative to untreated PSVs. **d)** Calculated neutralization titers. For live SARS-CoV-2 neutralization, a viral isolate, SARS-CoV-2 VDL1, obtained from a human nasopharyngeal swab sample was treated with serially diluted

58

Figure 2.9 (cont'd)

immune sera before Vero E6 2C2 cells were added. The cells were cultured for 5 days until the endpoint was detected. Titers were reported as the highest fold of serum dilution that showed the absence of viral cytopathic effect in the Vero E6 2C2 cells. Pooled (n = 5) mouse sera were used here. For HCS, the individual sample (1009, see **Figure 2.6**) that gave the highest anti-RBD IgG titer was used. The limits of detection were 100 folds of dilution for PSV neutralization and 10 fold for the live virus, respectively. All dilutions were done in duplicates and the error bars presented the standard deviations. **a) b) c)** Data was collected by our collaborators Dr. Dohun Pyeon and Dr. Canchai Yang from the Department of Microbiology and Molecular Genetics. d) data was provided by our collaborator Dr. Steven Bolin from the College of Veterinary Medicine.

2.2.6 mQβ-RBD vaccination mitigated immune evasion by VOCs

A major concern for SARS-CoV-2 prevention is the emergence of VOCs, against which current vaccines have significantly reduced protection efficacy.[17, 19, 20] We tested the abilities of immune sera to neutralize RBDs from VOCs Beta, Gamma, Delta and Omicron BA. 1 via sVNT (**Figure 2.10**). The NT50 values against the Omicron BA. 1 RBD (GMT 1,195) decreased about 3.6 times as compared to those against the RBD from the reference strain (GMT 4,345). However, the overall potency against all VOC's RBDs tested remained high (**Figure 2.10**), and neutralization against the Omicron RBD showed complete or near-to-complete inhibition of hACE2 binding at up to 120-fold dilution (**Figure 2.10b**). On the other hand, RBD immunized mouse sera or HCS all showed a significant reduction on NT50 (greater than 15.6 times) (**Figure 2.10a** and **c**). The loss of neutralization potency against the Omicron RBD was particularly severe, which was almost completely ineffective (GMT less than 10 and 12 for RBD immunized mouse sera or HCS, respectively) (**Figure 2.10a**).
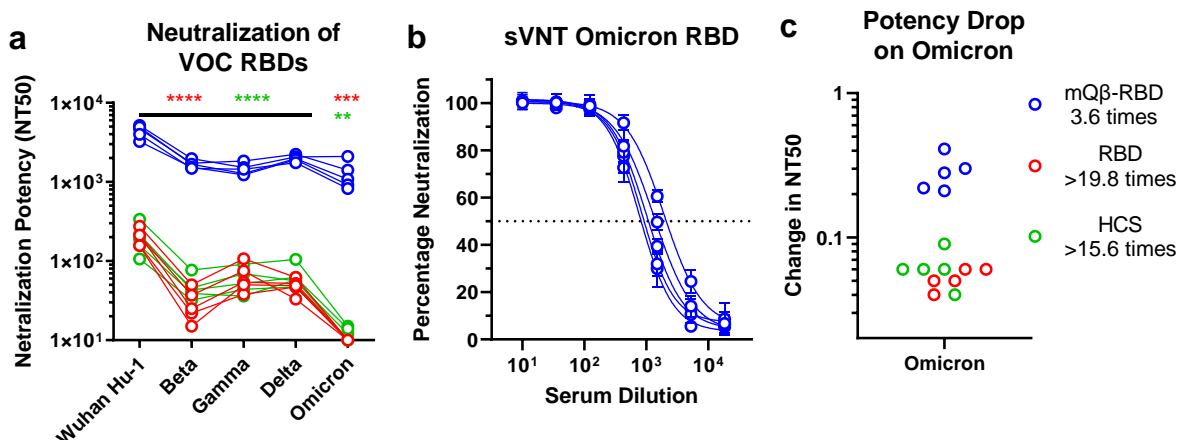
Figure 2.10 mQβ-RBD immune sera potently cross neutralized VOC RBDs as determined via sVNT. Assays were run in the same methods as against Wuhan-Hu1 RBD, except that HRP-RBD conjugates with VOC associated mutations were used. To account for differences in hACE2-RBD affinity and variations of RBD concentration in different batches, a titration of RBD concentration was performed before the neutralization assay. RBD concentrations were selected that gave equivalent hACE2 recognition (OD450 of 1.0). Symbols on the horizontal axis indicated no detectable neutralization. Statistical analysis was performed by comparing mQβ-RBD with every other group. ***, $p < 0.001$; ****, $p < 0.0001$, multiple unpaired t-test via GraphPad Prism 6. **b)** A representative data set (n=5) of mQβ-RBD sera neutralizing Omicron RBD. Each curve represented an individual mouse. **a), c)** Neutralization titers against VOC RBDs. mQβ-RBD maintained superior potency against all VOCs tested, while RBD alone immunization and HCS showed complete or partial loss of effectiveness against Omicron, respectively. Each symbol presented an individual mouse or HCS sample. The limit of detection for NT50s was 10 folds.

We also tested the immune sera against S-PSVs from the Delta variant. The mQβ-RBD immune sera had NT50 values of 25,838 against the Delta variant S, which was similar to that of neutralization potencies as found against S from the reference Wuhan-Hu-1 variant (NT50 = 26,504). NT50 titers for RBD immunized mouse sera and HCS against the Delta variant were significantly reduced (10,252 vs 5,056, and 2,674 vs 2,081) (**Figure 2.9b** and **d**).

2.2.7 mQβ-RBD induced persistent antibody responses in mice

As an anti-SARS-CoV-2 vaccine capable of inducing long lasting antibody responses is highly desirable, we monitored the levels of serum anti-RBD IgG antibodies in immunized mice over time following vaccination on days 0, 14 and 28 (**Figure 2.11a**). On day 7 after the initial immunization, high levels (~50% of the peak value) of anti-RBD were already observed in mQβ-RBD immunized mice. The anti-RBD antibody titers reached the peak between 35 and 56 days post priming (dpp) and maintained high over 225 dpp. Serum neutralization titers via sVNT on 225 dpp (GMT 4,052) were comparable (p=0.77) to those collected on 35 dpp (GMT 4,345) as well. In contrast, RBD immunized mice showed a significant reduction in serum antibody levels over time. The levels of anti-RBD antibodies and neutralization function from these mice were nondetectable on 225 dpp (**Figure 2.11b**). Those results supported the ability of mQβ-RBD conjugates to induce long lasting humoral responses.

2.2.8 Single dose mQβ-RBD immunization was effective.

Considering the fast-spreading nature of COVID-19, a vaccine that can work with a single dose would make its distribution much more accessible, especially in rural or developing regions. We tested a single dose immunization regime on mice and found that a single dose immunization produced a similar level of serum anti-RBD antibodies as indicated by ELISA ($p = 0.15$) (**Figure 2.11a**). Anti-RBD IgG titers after the single dose immunization on 35 dpp (GMT 156,099) were lower than those immunized by 3 doses (GMT 198,153), but the difference did not reach statistical

significance ($p = 0.20$, **Figure 2.11b**). Serum neutralization titers were lower (GMT 2,442) than

those induced by 3 dose immunization (GMT 4,345), but still significantly higher than those in

mice receiving 3 doses of free RBD immunization (GMT 198) (**Figure 2.11c**). The single dose

immunization also induced broadly neutralizing antibodies effective against all VOCs tested,

including the Omicron variant (**Figure 2.11**). Single dose immunization also induced a long-

lasting response, with persistent anti-RBD antibody levels and neutralization functions throughout

the 7 month period post immunization. For the unconjugated RBD, the single dose immunization

did not induce detectable titers of anti-RBD IgG after 35 dpp. These results demonstrated the
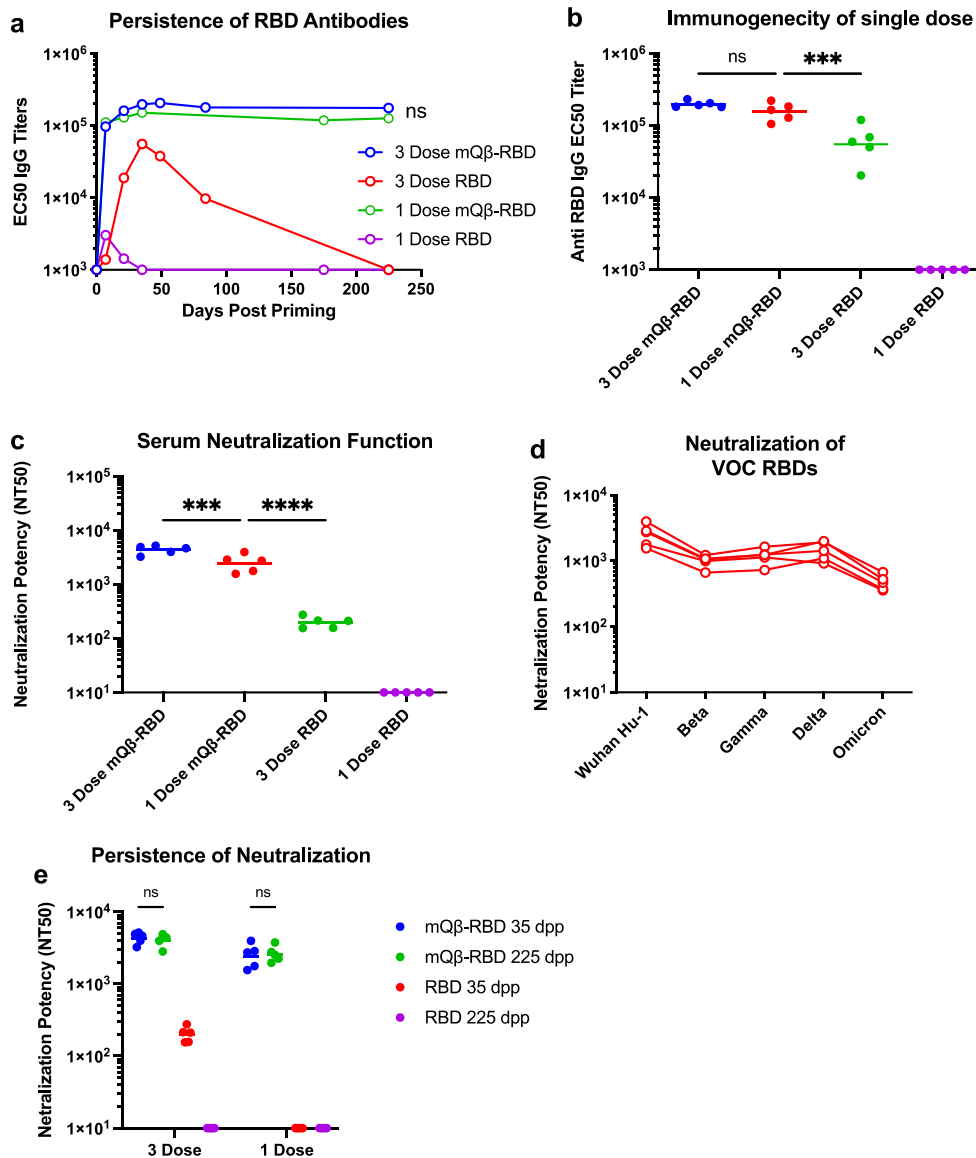
practical advantage of using the mQβ-RBD construct.

Figure 2.11 mQβ-RBD immunization induced long lasting immunity in mice. **a)** Sera samples were collected over time and anti-RBD IgG titers were monitored. Pooled (n = 5) sera were used. Titers were normalized to the GMT of individual mice on 35 dpp. For the three dose regimes, mice were vaccinated on days 0, 14, and 28. For the one dose study, mice were vaccinated on day 0. Levels of serum anti-RBD titers were compared between 3 dose and single dose groups via ELISA **b)**. Serum neutralization function against the native and VOC RBDs was evaluated via sVNT **c) d)**. Over more than 6 months post the last dose, mQβ-RBD immunized mice showed an anti-RBD antibody level and neutralization function comparable to those of a week following the last boost, regardless of numbers of doses used, while RBD alone induced immunity diminished completely **a) e)**. ns, non-significant; ****, $p < 0.0001$; **a) e)** paired t-test; **b)** one-way ANOVA; GraphPad Prism 6.

2.2.9 mQβ-RBD induced potent cellular responses in mice

T cells, including CD8^{+} cytotoxic T cells and CD4^{+} helper T cells, are another critical aspect of adaptive immunity besides antibody responses against SARS-CoV-2.[56, 57] To monitor cellular responses following immunization, splenocytes were collected from the immunized mice and the numbers of RBD reactive T cells were quantified via the IFN-γ ELISpot assay. As shown in **Figure 2.12a**, for both CD8^{+} and CD4^{+} cells isolated from mQβ-RBD immunized mouse spleens, significant amounts of RBD reactive, IFN-γ secreting T cells were observed after stimulation with the RBD primed bone marrow cells isolated from an unexposed mouse. This result indicates a significantly increased IFN-γ production by CD4^{+} and CD8^{+} T cells followed by the mQβ-RBD immunization compared to the free RBD immunization. T cell responses were also found to be persistent in mQβ-RBD immunized mice, as indicated by a similar number of RBD reactive T cells in samples collected on 225 dpp. On the other hand, the RBD immunized mice only showed detectable numbers of RBD reactive T cells on 35 dpp. Those results indicated the importance of using the mQβ carrier to induce persistent anti-SARS-CoV-2 T cell responses.

T cell responses against the Omicron RBD were also measured (**Figure 2.12b**). T cells isolated from mQβ-RBD immunized mouse spleens showed strong IFN-γ production responding to the Omicron RBD, similar to those observed against the Wuhan-Hu-1 RBD, suggesting that mQβ-RBD induced T cell responses are capable of recognizing the VOC.
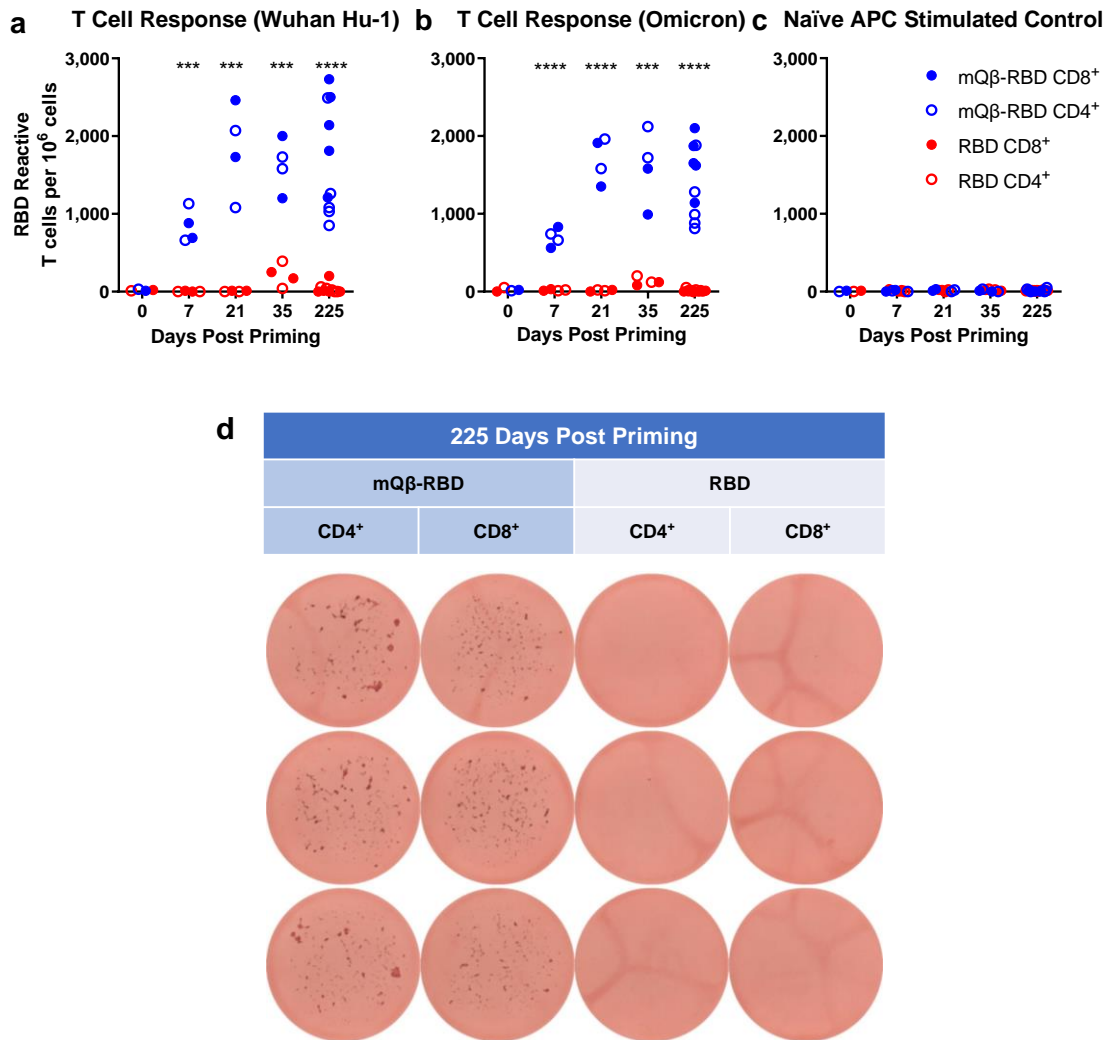
Figure 2.12 mQβ-RBD induced high magnitudes of anti-RBD T cell responses. Immunized mice were euthanized, and the spleens were collected. The CD8^{+} T cells were enriched by anti-CD8a microbeads and followed by the removal of CD4^{+} subpopulation by flushing through anti-CD4 microbeads. The CD4^{+} T cells were isolated in the same manner. 10^5 cells of each type were added to an INF-γ antibody coated MIPS plate. Mouse bone marrow cells were collected from a non-immunized mouse and primed with the RBD from **a)** the Wuhan Hu-1 or **b)** the Omicron variant. The primed bone marrow cells were added to the CD8^{+} and CD4^{+} cells, cocultured for 16 hours. Untreated bone marrow cells were also added the CD8^{+} and CD4^{+} cells for control and results were shown in panel **c**. The cells were removed and the captured INF-γ was detected by a biotinylated monoclonal antibody. The spots were developed by HRP conjugated streptavidin and 3-Amino-9-ethylcarbazole (AEC) substrate. Each sample was run in triplicates and the average numbers of spot forming units were plotted for each million cells. Each symbol presented a single mouse, and the statistical analysis was performed considering CD4^{+} and CD8^{+} cells together. **c)** Representative

images of spots formed by the mice splenic T cells in response to the naïve bone marrow cells presenting the Wuhan Hu-1 RBD on 225 dpp. ***, $p < 0.001$; ****, $p < 0.0001$; multiple unpaired t-test via GraphPad Prism 6.

For conjugate vaccine design, it is critical to select suitable antigen structures. Short peptides were commonly used for VLP conjugate vaccines due to their ease of synthesis and defined conjugation chemistry.[48, 58, 59] However, in our study, despite the high levels of IgG antibodies elicited by multiple mQβ-(glyco)peptide conjugates, there were little IgG antibodies produced recognizing the RBD and capable of neutralizing the RBD-hACE2 interactions (**Figure 2.2**). This suggests that the protective epitopes in the RBD are most likely 3-dimensional, and the (glyco)peptides may not have mimicked well their native conformation within the context of the full protein, thus failing to induce strong protective antibody responses. Thus, future efforts should focus on the full-length RBD as the epitope for RBD based vaccine design.

RBD alone has been used as a vaccine candidate,[37] which was found to generate neutralizing antibodies in mice, rabbits, and non-human primates and provide protection in non-human primates to an *in vivo* challenge with SARS-CoV-2. However, the immune responses induced by the RBD need to be improved as the antibodies did not last a long time, and they lost much efficacy against VOCs (**Figure 2.10** and **Figure 2.11**). Furthermore, T cell responses produced by the RBD immunization were suboptimal (**Figure 2.12**). In order to enhance the immunogenicity of RBD, various platforms including ferritin nanoparticles,[7] self-assembling nanoparticles[5, 6, 60] and aldolase based self-assembling frameworks[61] have been studied for antigen presentation. However, the

abilities to induce long-term antibody responses capable of neutralizing multiple VOCs such as Omicron have yet to be demonstrated by those platforms.

We demonstrated that the covalent conjugation of the RBD with the mQβ significantly enhanced both the humoral and cellular immunity against SARS-CoV-2. mQβ VLP has a well-defined 3D structure capable of organized display of antigens.[43] This feature is critical to powerfully activate the cognizant B cells and boost the antibody responses against the target antigen.[62] Furthermore, mQβ contains T cell epitopes for both mice and humans, and encapsulates RNA in the interior, which can function as potent adjuvants through the activation of Toll Like Receptor-7.[63, 64] These features provide a rationale of the superiority of the mQβ-RBD in producing neutralizing immunity as compared to RBD alone or the RBD conjugate with the gold standard carrier CRM-197.

To effectively protect against viral pathogens, directing the immune response to neutralizing epitopes is critical. Non-neutralizing epitopes may compete for limited T cell help in the body hindering the production of protective epitopes.[48] Furthermore, antibodies against SARS-CoV-2 that are non-neutralizing may induce inflammatory cytokines.[52, 53] mQβ-RBD conjugate immunization achieved superior neutralization potency via not only its high overall anti-RBD antibody titers but also the production of neutralizing antibodies, indicated by its high N/B ratio. Neutralization potencies were tested via ELISA based on RBD-hACE2 recognition inhibition, pseudovirus or live SARS-CoV-2 based cellular assay. These results correlated well with each

other, consistent with the idea that blocking of receptor engagement is the major mechanism of neutralization for the tested constructs. The high N/B ratio achieved may be due to the conjugation site selected leading to ready access of the RBM within the mQβ-RBD conjugate as compared to the free RBD (**Figure 2.5a**). These results are consistent with the idea of epitope-focused vaccine design.[65, 66] Long circulating pathogens like human influenza have adapted to the human immune system by hiding their conserved, broadly neutralizing epitopes under the coverage of hypervariable immunodominant regions. As a result, natural infection or conventional vaccine only gave limited neutralization breadth.[67] Studies have shown to utilize computational approach to design *de novo* proteins that mimic the structural features of hidden broadly neutralizing epitopes.[66, 68] Our results suggested by the precise control of conjugation site, immune responses could be shifted more toward the desired epitopes.

Mucosal immune response in the BALF is essential for prevention of viral spreading. Relative weak mucosal response induced by the current mRNA vaccines may be one of the contributing factor to their low effectivity in prevention of infection, especially against Omicron.[31] Our results demonstrated that subcutaneous administration of mQβ-RBD can induce potent mucosal responses including induction of IgA antibodies in BALF. The BALF antibody subtype distribution pattern induced by our construct was similar to those observed in other studies based on nanoparticle platforms.[60, 61] Robust neutralization in the BALF may support its ability to effectively block infectivity.

Due to reduced neutralization activity and fast waning immunity, currently approved vaccines struggle to protect against VOCs such as Omicron. Studies reported 7-30 fold reduction in neutralization potency against Omicron after 2-3 doses of vaccination or previous infection.[14, 20] We observed a similar trend for the HCS sera collected before the emergence of Omicron. mQβ-RBD showed a far less severe escape by Omicron (only a 3.6-fold reduction). We hypothesize that VLP Qβ may mitigate antigenic drifts in VOCs by the potent engagement of T follicular helper (Tfh) cells[69] via B cell presentation as shown by other studies.[70, 71] Tfh cells are essential for the development of broadly neutralizing antibodies against SARS-CoV-2,[72, 73] and might not be robustly and broadly activated during natural infection, at least in a short period, as indicated by the characteristic low rate of somatic hypermutation presented in most early neutralizing monoclonal antibodies isolated from convalescent patients.[74-76] Those early monoclonal antibodies mostly failed to neutralize Omicron.[16-20] These results support the idea of applying a highly immunogenic carrier such as mQβ for conjugate vaccines.

2.3 Conclusion

Among multiple peptides and glycopeptides as well as the full length RBD, RBD has been shown to be the most suitable epitope for vaccine design. Upon covalent linkage with mQβ, the mQβ-RBD conjugate is able to induce high levels and long-lasting antibodies against SARS-CoV-2 much more effectively than RBD alone or RBD conjugate with a gold standard carrier CRM-197. The antibodies produced can neutralize multiple variants including clinical isolates.

Furthermore, potent CD4$^+$ and CD8$^+$ T cells were induced through vaccination against both the reference strain and the Omicron variant. This is the first time that VLPs have been reported as a carrier to deliver the full length RBD protein in a conjugate vaccine. The effectiveness of mQβ-RBD in single dose immunization regime lowers the barrier to immunizing a massive population, especially in developing countries, highlighting its exciting potential.

2.4 Experimental methods

2.4.1 Expression of the RBD

100 µg of plasmid encoding SARS-CoV-2 RBD with the Wuhan Hu-1 sequence (BEI NR-52309) was transfected into 3×10^8 expi293 cells in 100mL of medium using expi293^{TM} expression system kit (Gibco A14635). One day post-transfection, transfection enhancers 1 and 2 were added to the culture per manufacturer's instructions. 5 days post-transfection, the cells are harvested and spun at 4,000 g for 5 min at 4°C. The supernatant containing the desired protein was collected and further purified by Ni-NTA, yielding 20mg protein per liter of culture. This experiment is conducted by Po-Han Lin.

2.4.2 Production of the mQβ conjugates

The peptides 1-5, 9-10 were purchased from SinoBio (https://www.synbio-tech.com/peptide-synthesis/custom-peptide-synthesis/). Glycopeptides 6-8 were synthesized by Dr. Sherif Ramadan via solid phase peptide synthesis protocol with glycosylated amino acids. All peptides except peptide 2 were N-terminus-caped with acetylation. The mQβ VLP particle and

peptide conjugations were prepared and characterized following protocols previously described.[43]

For the mQβ-RBD conjugate, mQβ was first modified with SMPEG2 (ThermoFisher 22103). To

a 1 ml solution of 10 mg/ml mQβ in 0.1 M potassium phosphate buffer (KPB) pH 7.0 was added

3.2 mg SMPEG2 (7.5 µmol, 2 equiv to accessible amines on the external surface (5 amines per

coat protein monomer)) in 10 µl DMSO. The mixture was gently nutated under room temperature

for 1 hour before 50 µl 500 mM Tris buffer pH 7.0 was added to quench the unconsumed

succinimidyl ester. The mixture was injected to a Superose 6 increase 10/300 GL SEC column

(Cytivia 29091596) on a Cytivia AKTA pure 25L system. The elution was conducted with PBS

(10 mM phosphate buffer with 150 mM NaCl, pH 7.4) in a flow rate of 0.5 ml/min. The peak

between 11- 13 ml was collected. The modified protein was concentrated to 0.5 ml volume with a

100 kD membrane filter (Millipore UFC9100) and the solution pH was adjusted to 8.0 with 5 M

KOH. 10 mg SARS-CoV-2 RBD (80 RBD molecules per mQβ particle) in 0.5 ml of 0.1 mM KPB

at pH 8.0 containing 20 mM EDTA was added. The mixture was purged with N_2, sealed and gently

nutated in dark under 4 °C for 36 h, before 1 M cysteine was added to a final concentration of 10

mM and the incubation was continued for another 12 h. The mixture was injected to the SEC

column and the peak between 9- 11 ml was collected. The unconjugated RBD eluted between 17-

22 ml and the area under UV absorbance curve was used to calculate conversion, based on a

standard curve calculated from a series of pure RBD injected at various concentrations. The RBD

loading on the mQβ was estimated to be 20 per capsid based on the consumption of the RBD.

2.4.3 Production of the CRM-RBD

1 mg CRM197 (FinaBio) was buffer exchanged to remove Tris and concentrated to a final solution of 0.1 ml KPB pH 7.0. The protein was modified with 0.14 mg SMPEG2 (0.33 µmol, 20 equiv) in the same condition for mQβ. Modified protein was collected on SEC between 15- 17 ml and reacted with 5 mg RBD (1: 10 molar ratio) in 0.2 ml KPB pH 8.0 with 10 mM EDTA in the same manner as the mQβ. Cysteine was added to a final concentration of 10 mM and nutated for 12 h before the final product was collected on the SEC between 14- 16 ml. The loading was 3.5 RBD per CRM197 based on consumption of the RBD.

2.4.4 Size characterization of mQβ-RBD

To measure the hydrodynamic size of the conjugate, 0.1 mg/ml protein in PBS was prepared and DLS was run on a Zetasizer Nano ZS at 25 °C. A 90 ° measurement angle was used, and data was analyzed using build-in protein parameters. The measurement was repeated 3 times for each sample (**Figure 2.3**). The SEC trace of the purified conjugate also showed a slight size increase as reflected by the decrease in elution time (**Figure 2.4**).

2.4.5 ELISA for verification of the RBD conjugation

The mQβ-RBD conjugate containing 10 to 150 ng RBD (on 42.3 to 635 ng mQβ-RBD conjugate) was coated on Nunc MaxiSorp 96 well plates (ThermoFisher 44-2404-21) in 100 µl PBS each well. 10- 1200 ng free RBD in 100 µl PBS was coated as standards. 1000 ng mQβ was also coated as a control. The plates were covered and kept at 4 °C overnight. The liquid was

discarded, and the wells were blocked by 200 µl PBS containing 1% BSA for 1 h. The plates were then washed with PBS pH 7.4 containing 0.5% Tween-20 (PBST) for 4 times. **a)** 20 ng hACE2-Fc chimera protein (GenScript Z03484) or **b)** 1: 2000 HRP-rabbit anti His-tag antibody (JacksonImmunoResearch 300-035-240) in 100 µl PBS containing 0.1% BSA was added to the wells for 2 h before the liquid was discarded. The wells were washed with PBST for 4 times before **a)** 1: 2000 HRP-goat anti human IgG antibody (JacksonImmunoResearch 109-005-003) or **b)** 1: 2000 HRP-goat anti rabbit IgG antibody (JacksonImmunoResearch 111-005-144) in 100 µl PBS containing 0.1% BSA was added. The liquid was discarded after 1 h incubation and the plates were washed with PBST for 4 times. 200 µl TMB (Sigma 860336) substrate solution (0.25 mg/ml TMB and 0.03% w/v hydrogen peroxide in citrate buffer with 10% DMSO) was added to the wells and OD 625 nm was recorded on a Molecular Devices SpectraMax M3 each 30 seconds over 10 mins. Vmax (mAU/min) was calculated using OD values between 0 and 0.5 AU and plotted against equivalent RBD quantities. Fitting was done by the 4PL nonlinear logistics (GraphPad Prism 6 with least squares algorism). The IC50 values of the fitting curves were used to compare binding. The mQβ coated wells did not show detectable binding (<3 mAU/min) in both cases and were subtracted as the blank for the data reported here. All concentrations were run on triplicates. All steps were run under ambient temperature unless specified.

2.4.6 Immunization protocol

Pathogen-free C57BL/6 female mice aged 6 weeks were obtained from the Charles River and maintained in the University Laboratory Animal Resources facility of Michigan State University. All animal care procedures and experimental protocols have been approved by the Institutional Animal Care and Use Committee (IACUC) of Michigan State University. Groups of five mice were injected subcutaneously under the scruff on day 0, 14 and 28 with the mQβ-RBD or the CRM-RBD conjugates containing 10 µg RBD in 0.2 mL sterile PBS. For the peptide conjugates, constructs containing 8 nmol peptides were used. For the free RBD, 10 µg RBD was used. For the admix, 10 µg RBD and 42.3 µg mQβ was used. 20 µg MPLA (Sigma L6895) in 20 µl DMSO was added to each dose as the adjuvant right before immunization. The serum samples were collected on days 0 (before immunization), 7, 21 and 35 via the saphenous vein. The final bleeding was done by cardiac puncture.

2.4.7 HCS

Blood samples were obtained from volunteers of Hatzalah of Michigan with consent from the donors. All 20 HCS samples were from patients hospitalized for COVID-19 related symptoms and had been diagnosed SARS-CoV-2 RNA positive via qPCR in May 2020. Blood samples were collected in their convalescent phase. The patients had an average age of 48 (min 26, max 68, median 48, std dev 12) when the samples were collected. Serum samples were isolated by

centrifugation at 4,000 g at 4 °C for 30 mins upon receiving, heat-inactivated under 56 °C for 30 mins and stored at -80 °C until use.

2.4.8 ELISA for serum antibody titers

Immulon 4 HBX 384 well plates (ThermoFisher 8755) were coated with 0.5 µg RBD in 50 µl PBS at 4 °C overnight. For BSA-(glyco)peptide conjugates, 0.5 µg conjugates were used. The liquid was discarded, and the wells were blocked by 100 µl PBS containing 1% BSA for 1 h. The liquid was discarded, and the plates were washed by PBST for 4 times. The immune sera were serial diluted in PBS containing 0.1% BSA. 50 µl diluted serum was added to each well and incubated for 2 h. The liquid was discarded, and the plates were washed with PBST for 4 times. 1: 2,000 HRP-goat anti mouse IgG antibody (JacksonImmunoResearch 115-035-003) in 50 µl PBS containing 0.1% BSA was added and incubated for 1 h. For HCS samples, the HRP-goat anti human IgG antibody was used. For subtypes, corresponding goat anti mouse antibodies were used. All IgG subtype secondary antibodies were from JacksonImmunoResearch. IgG1: 115-007-186; IgG2a: 115-035-1206; IgG2b: 115-035-207; IgG2c: 115-035-208; IgG3: 115-035-209. For IgA, Invitrogen 62-6720 was used. The liquid was discarded, and the plates were washed with PBST for 4 times. 75 µl TMB substrate solution was added to each well and the reaction was allowed to proceed for 15 mins before 25 µl 0.5 M sulfuric acid was added. OD450 was immediately recorded and fitted into the 4PL nonlinear logistic model via GraphPad Prism 6 with least squares algorism. BSA coated wells showed negligible signal (<0.1 AU) and were subtracted as plate blank.

Maximum OD values reached to ~3.0 for all groups. An OD of 1.5 intercept was universally used for all groups to calculate EC50 titers. All dilutions were run as triplicates. All steps were run under ambient temperature unless specified.

2.4.9 sVNT assay

Immulon 4 HBX 384 well plates were coated each well with 1 µg goat anti human IgG antibody (Sigma I2136) in 50 µl PBS under 4 °C overnight. The liquid was discarded, and the wells were blocked with 100 µl PBS containing 1% BSA. The liquid was discarded, and the plates were washed with PBST for 4 times. 25 ng hACE2-Fc chimera protein in 25 µl PBS with 0.1% BSA was added to each well and incubated for 1 h. The liquid was discarded, and the plates were washed with PBST for 4 times. For HCS, 100 ng hACE2-Fc in 25 µl PBS was directly coated overnight to avoid the binding of anti-human IgG to antibodies present in the HCS. Higher hACE2 concentration was used to ensure the same level of RBD binding since direct coating was not as efficient as antibody capturing. On the other hand, immune sera were serially diluted in PBS with 1% BSA and mixed (1: 1, v: v) with 1:1,000 diluted HRP-RBD (GenScript Z03594) in PBS with 1% BSA. For VOC RBDs, GenScript Z03596 (Beta), GenScript Z03601 (Gamma), GenScript Z03614 (Delta) and GenScript Z03730 (Omicron) was used. VOC RBDs have variable binding affinity to hACE2. As a result, a titration with variable RBD concentration was performed before each assay with the same method except immune sera were omitted. The concentration for each VOC that gave the constant level of hACE2 binding comparing to the reference RBD (OD450 of

1 AU) was determined and used. The serum-RBD mixtures were incubated for 1 h and a 50 µl aliquot was added to each well of the hACE2 coated plates. Incubation was continued for another 1 h before the liquid was discarded. The plates were washed with PBST and 75 µl TMB substrate solution was added to each well. The reaction was allowed to proceed for 15 mins before 25 µl 0.5 M sulfuric acid was added and OD450 was immediately recorded. Serum omitted wells reached OD of ~1 AU and were used for standards for 0% neutralization. RBD omitted wells showed negligible binding (OD < 0.1 AU) and were used as standards for 100% neutralization. For other wells, neutralization efficiency was determined as:

$$\% \: Neutralization = 100\% \times \frac{OD(Serum \: omitted) - OD(Immune \: Serum)}{OD(Serum \: omitted) - OD(RBD \: ommitted)}$$

Neutralization efficiency was fitted into serum dilution via the 4PL nonlinear logistic model via GraphPad Prism 6 with least squares algorism. Highest serum dilution fold that gave 50% neutralization was determined for each sample as NT50 titer. All dilutions were run on triplicates. All steps were run under ambient temperature unless specified.

2.4.10 Mouse BALF collection

The method was adapted from a published study.[77] Pathogen-free C57BL/6 female mice (n=5) were immunized with mQβ-RBD or RBD per protocol described above. Mice were euthanized on day 35 post priming, and blood samples were collected by cardiac puncture, where a needle was carefully inserted to the heart through the diaphragm without piercing the lungs. A small fraction

(~50 µl) of blood was collected by a heparin coated vial for blood cell counting. For each mouse, whole lungs were removed from the chest cavity along with the trachea. The lungs were transferred to a petri dish where the surface was washed by PBS to remove potential blood contamination. Mucus wash was performed by repeated instill and aspiration of the same 1 ml PBS with 0.1% BSA via the trachea by a 1 ml syringe. The wash was repeated for 7 times. ELISA analysis of aliquoted samples after each wash indicated no increase in anti-RBD IgG titers after the 6th wash. To correct the potential serum antibody contamination from micro bleeding during the wash, blood cell concentration was counted in the BALF wash and compared to the blood sample from the same mouse. Blood contamination was determined by the following formular:

$$\% \ Blood \ contamination = 100\% \times \frac{Blood \ cell \ concentration \ in \ mucus \ wash \times 40}{Blood \ cell \ concentration \ in \ blood}$$

Where 40 is the dilution factor to the BALF introduced by the washing. This ratio was based on the estimated volume of 25 µl BALF for a mouse.[77] Blood contamination was less than 5% for all samples collected and had been subtracted from the titers reported in this work.

2.4.11 Pseudovirus neutralization assay

Lentiviral PSVs were generated by transfecting 293FT cells with 4µg of viral packaging plasmid with luciferase reporter gene (pNL4-3 Luc) and 4µg of plasmid expressing the envelop gene (pCMV14-CoV2S Wuhan Hu-1/Delta or pCMV-VSVg). 48 h post transfection cell supernatant containing PSVs were vacuum filtered through a 0.22µm Durapore PVDF membrane

and then concentrated by ultracentrifugation at 76,800 g (SW 32 Ti) at 4°C for 2 h. Concentrated PSVs were then incubated with pooled (n=5) immune sera (collected 35dpp) or HCS 1009 (which contains highest amount of anti-RBD IgG in 20 HCS samples, see **Figure 2.6**) at threefold serial dilution from 100 - 218,700 and spun at 500 g for 1 min. The supernatant was incubated 1 h at 37°C in a humified atmosphere of 5% CO_2. After 1 h, 293FT cells transiently expressing hACE2 were added and incubated for 60 h at 37 °C in a humified atmosphere of 5% CO_2. PSV neutralization by sera were assessed by Bright Glo luciferase assay (Promega E2610). Relative luminescence units (RLU) were recorded to present infectivity after luciferin was added. Mock infection was carried out without PSVs as standard for 100% neutralization. Pre-immune serum was used as the standard for 0% neutralization. For all other samples, percentage neutralization efficiency was determined as:

$$\% \, Neutralization = 100\% \times \frac{RLU(Pre-immune) - RLU\,(Immune\,Serum)}{RLU\,(Pre-immune) - RLU\,(Mock\,infection)}$$

Percent neutralization was fitted to serum dilution via 4PL nonlinear logistics (GraphPad Prism 6, least squares). NT50 titers were determined to present the highest serum dilutions that gave 50% neutralization. All samples were run in duplicates. All steps were carried under ambient temperature unless specified.

2.4.12 Live virus neutralization assay

All steps were conducted under BSL-3 condition. A standard microtitration viral neutralization assay was done using Vero E6 2C2 cells (a biological clone of the Vero E6 cell line) and a 96 well microtitration plate. A viral isolate, SARS-CoV-2 VDL1, was made from a nasopharyngeal swab sample isolated in April 2020 from a patient in Michigan. The strain was passaged 4 times in Vero E6 cells and cell free supernatant was frozen at -80 °C for viral stock. Viral stock was titrated at 10-fold dilutions in HEPES buffered Medium 199 (M199) supplemented with 6% fetal bovine serum. Monolayers of Vero E6 2C2 cells in microtitration plate wells were used to identify the dilution of viral stock that contained approximately 100 cell culture infective doses of virus (CCID) per 100 µl. In the top well of a microtitration plate column of wells, immune serum or HCS 1009 (which contains highest amount of anti-RBD IgG in 20 HCS samples, see **Figure 2.6**) was diluted 1:10 in supplemented M199 then serial 2-fold dilutions were made in M199 down an 8 well column. An appropriate dilution of virus was added to each dilution of serum and incubated for 1 hour at 37 °C in a humified atmosphere of 5% CO_2 in air. A back titer of the viral dilution used in the assay was included in the microtitration plate to confirm the dose of virus used was approximately 100 CCID. After 1 hour, Vero E6 2C2 cells were added to each dilution of serum and to the back titer of virus. The microtitration plate was sealed with tape and incubated for 5 days until the endpoint of antibody titer was determined. The endpoint was the

reciprocal of the last dilution of serum that completely neutralized virus, as determined by an absence of viral cytopathic effect in the Vero E6 2C2 cell monolayer.

2.4.13 ELISpot assay

Pathogen-free C57BL/6 female mice (n=11) were immunized with mQβ-RBD or RBD per protocol described above. 2 mice were sacrificed on days 7, 21, and 35 for T cell collection. The final 5 mice in each group were sacrificed on day 225. Mouse spleens were collected and crunched to single cells by a 1 ml syringe piston in a gentle circular motion. The resulting cells were treated with red blood cell (RBC) lysis buffer and filtered through a 70 µm cell strainer to yield ~10^8 splenocytes from each mouse. Cells were suspended in 90% FBS, 10% DMSO and frozen in liquid nitrogen until use. For ELISpot, thawed cells were suspended in PBS containing 0.1% BSA and 2 mM EDTA. CD8$^+$ cells were enriched by binding to anti mouse CD8a microbeads (Miltenyi Biotec 130-117-044) and flowing through a magnetized column (Miltenyi Biotec 130-042-401). The flow through cells were subjected to CD4$^+$ T cell isolation. CD8$^+$ cells retained on column were eluted after magnetization was removed and bound to anti mouse CD4 microbeads (Miltenyi Biotec 130-117-043). The CD8$^+$CD4$^+$ subpopulation was removed by flowing through a magnetized column, yielding in the flow through ~10^6 CD8$^+$ T cells for each 10^7 splenocytes. CD4$^+$ T cells were isolated in a similar manner, yielding ~1.5×10^6 CD4$^+$ T cells. Mouse bone marrow cells were collected from an unimmunized female C57BL/6 mouse. The mouse was euthanized and both femurs were collected. Both ends of the femurs were cut off and the bone marrow cells were collected by

flushing through 5 ml ice cold culture medium (RPMI 1640 medium supplemented with L-glutamine (Gibco 11875093) and 10% FBS (Sigma F6765)) followed by RBC lysis buffer treatment and filtration through a 70 µm cell strainer. ~5×10^7 cells were collected from a mouse. The bone marrow cells were cultured in the culture medium primed with 10 µg/ml SARS-CoV-2 RBD from Wuhan Hu-1 (BEI NR52306) or Omicron (SinoBiological 40592-V08H121) at 37 °C in a humified atmosphere of 5% CO_2 in air for 6 h. Unprimed bone marrow cells were used for control. MultiScreen-IP Filter Plates (Millipore S2EM004M99) were coated with 10 µg/ml an anti-mouse IFN-γ capture antibody (BD 51-2525KZ) in 100 µl PBS at 4 °C overnight. The liquid was discarded, and the plates were washed with the culture medium. The wells were blocked with 200 µl culture medium for 2 h before the liquid was discarded. To each well was added 2×10^4 primed or unprimed bone marrow cells and 10^5 CD8$^+$ or CD4$^+$ cells in 100 µl culture medium. The plates were covered and incubated at 37 °C in a humified atmosphere of 5% CO_2 in air for 16 h before the cell suspension was discarded. The plates were soaked with DI water for 5 mins twice and washed with 0.05% PBST for 3 times. To each well was added 5 µg/ml a biotinated anti mouse IFN-γ detection antibody (BD 51-1818KA) in 100 µl PBS with 0.1% BSA and incubated for 2 h. The liquid was discarded, and the plates were washed with 0.05% PBST for 3 times. 1: 100 diluted Streptavidin-HRP (BD 557630) in PBS with 0.1% BSA was added to each well and incubated for 1 h. The liquid was discarded, and the wells were washed with 0.05% PBST for 4 times followed by PBS twice. 100 µl AEC substrate solution (BD 551951) was added to each well and the reaction

was allowed to proceed for 10 mins before the liquid was discarded and the plates were washed under running DI water. The wells were air dried overnight, imaged and analyzed by a Cellular Technology Ltd. ImmunoSpot System. Each cell type for each mouse was run in triplicates. All steps were performed under ambient temperature unless specified.

REFERENCES

1. Wang, H.; Paulson, K. R.; Pease, S. A.; Watson, S.; Comfort, H.; Zheng, P.; Aravkin, A. Y.; Bisignano, C.; Barber, R. M.; Alam, T., Estimating Excess Mortality Due to the COVID-19 Pandemic: A Systematic Analysis of COVID-19-Related Mortality, 2020–21. *Lancet* **2022,** *399*, 1513-1536.

2. Corbett, K. S.; Edwards, D. K.; Leist, S. R.; Abiona, O. M.; Boyoglu-Barnum, S.; Gillespie, R. A.; Himansu, S.; Schafer, A.; Ziwawo, C. T.; DiPiazza, A. T.; Dinnon, K. H.; Elbashir, S. M.; Shaw, C. A.; Woods, A.; Fritch, E. J.; Martinez, D. R.; Bock, K. W.; Minai, M.; Nagata, B. M.; Hutchinson, G. B.; Wu, K.; Henry, C.; Bahl, K.; Garcia-Dominguez, D.; Ma, L.; Renzi, I.; Kong, W. P.; Schmidt, S. D.; Wang, L.; Zhang, Y.; Phung, E.; Chang, L. A.; Loomis, R. J.; Altaras, N. E.; Narayanan, E.; Metkar, M.; Presnyak, V.; Liu, C.; Louder, M. K.; Shi, W.; Leung, K.; Yang, E. S.; West, A.; Gully, K. L.; Stevens, L. J.; Wang, N.; Wrapp, D.; Doria-Rose, N. A.; Stewart-Jones, G.; Bennett, H.; Alvarado, G. S.; Nason, M. C.; Ruckwardt, T. J.; McLellan, J. S.; Denison, M. R.; Chappell, J. D.; Moore, I. N.; Morabito, K. M.; Mascola, J. R.; Baric, R. S.; Carfi, A.; Graham, B. S., SARS-CoV-2 mRNA vaccine design enabled by prototype pathogen preparedness. *Nature* **2020,** *586* (7830), 567-571.

3. Polack, F. P.; Thomas, S. J.; Kitchin, N.; Absalon, J.; Gurtman, A.; Lockhart, S.; Perez, J. L.; Perez Marc, G.; Moreira, E. D.; Zerbini, C.; Bailey, R.; Swanson, K. A.; Roychoudhury, S.; Koury, K.; Li, P.; Kalina, W. V.; Cooper, D.; Frenck, R. W., Jr.; Hammitt, L. L.; Tureci, O.; Nell, H.; Schaefer, A.; Unal, S.; Tresnan, D. B.; Mather, S.; Dormitzer, P. R.; Sahin, U.; Jansen, K. U.; Gruber, W. C.; Group, C. C. T., Safety and Efficacy of the BNT162b2 mRNA Covid-19 Vaccine. *N Engl J Med* **2020,** *383* (27), 2603-2615.

4. Tian, J. H.; Patel, N.; Haupt, R.; Zhou, H.; Weston, S.; Hammond, H.; Logue, J.; Portnoff, A. D.; Norton, J.; Guebre-Xabier, M.; Zhou, B.; Jacobson, K.; Maciejewski, S.; Khatoon, R.; Wisniewska, M.; Moffitt, W.; Kluepfel-Stahl, S.; Ekechukwu, B.; Papin, J.; Boddapati, S.; Jason Wong, C.; Piedra, P. A.; Frieman, M. B.; Massare, M. J.; Fries, L.; Bengtsson, K. L.; Stertman, L.; Ellingsworth, L.; Glenn, G.; Smith, G., SARS-CoV-2 spike glycoprotein vaccine candidate NVX-CoV2373 immunogenicity in baboons and protection in mice. *Nat Commun* **2021,** *12* (1), 372.

5. Walls, A. C.; Miranda, M. C.; Schafer, A.; Pham, M. N.; Greaney, A.; Arunachalam, P. S.; Navarro, M. J.; Tortorici, M. A.; Rogers, K.; O'Connor, M. A.; Shirreff, L.; Ferrell, D. E.; Bowen, J.; Brunette, N.; Kepl, E.; Zepeda, S. K.; Starr, T.; Hsieh, C. L.; Fiala, B.; Wrenn, S.; Pettie, D.; Sydeman, C.; Sprouse, K. R.; Johnson, M.; Blackstone,

A.; Ravichandran, R.; Ogohara, C.; Carter, L.; Tilles, S. W.; Rappuoli, R.; Leist, S. R.; Martinez, D. R.; Clark, M.; Tisch, R.; O'Hagan, D. T.; Van Der Most, R.; Van Voorhis, W. C.; Corti, D.; McLellan, J. S.; Kleanthous, H.; Sheahan, T. P.; Smith, K. D.; Fuller, D. H.; Villinger, F.; Bloom, J.; Pulendran, B.; Baric, R. S.; King, N. P.; Veesler, D., Elicitation of broadly protective sarbecovirus immunity by receptor-binding domain nanoparticle vaccines. *Cell* **2021,** *184* (21), 5432-5447.

6. Saunders, K. O.; Lee, E.; Parks, R.; Martinez, D. R.; Li, D.; Chen, H.; Edwards, R. J.; Gobeil, S.; Barr, M.; Mansouri, K.; Alam, S. M.; Sutherland, L. L.; Cai, F.; Sanzone, A. M.; Berry, M.; Manne, K.; Bock, K. W.; Minai, M.; Nagata, B. M.; Kapingidza, A. B.; Azoitei, M.; Tse, L. V.; Scobey, T. D.; Spreng, R. L.; Rountree, R. W.; DeMarco, C. T.; Denny, T. N.; Woods, C. W.; Petzold, E. W.; Tang, J.; Oguin, T. H., 3rd; Sempowski, G. D.; Gagne, M.; Douek, D. C.; Tomai, M. A.; Fox, C. B.; Seder, R.; Wiehe, K.; Weissman, D.; Pardi, N.; Golding, H.; Khurana, S.; Acharya, P.; Andersen, H.; Lewis, M. G.; Moore, I. N.; Montefiori, D. C.; Baric, R. S.; Haynes, B. F., Neutralizing antibody vaccine for pandemic and pre-emergent coronaviruses. *Nature* **2021,** *594* (7864), 553-559.

7. Joyce, M. G.; Chen, W. H.; Sankhala, R. S.; Hajduczki, A.; Thomas, P. V.; Choe, M.; Martinez, E. J.; Chang, W. C.; Peterson, C. E.; Morrison, E. B.; Smith, C.; Chen, R. E.; Ahmed, A.; Wieczorek, L.; Anderson, A.; Case, J. B.; Li, Y.; Oertel, T.; Rosado, L.; Ganesh, A.; Whalen, C.; Carmen, J. M.; Mendez-Rivera, L.; Karch, C. P.; Gohain, N.; Villar, Z.; McCurdy, D.; Beck, Z.; Kim, J.; Shrivastava, S.; Jobe, O.; Dussupt, V.; Molnar, S.; Tran, U.; Kannadka, C. B.; Soman, S.; Kuklis, C.; Zemil, M.; Khanh, H.; Wu, W.; Cole, M. A.; Duso, D. K.; Kummer, L. W.; Lang, T. J.; Muncil, S. E.; Currier, J. R.; Krebs, S. J.; Polonis, V. R.; Rajan, S.; McTamney, P. M.; Esser, M. T.; Reiley, W. W.; Rolland, M.; de Val, N.; Diamond, M. S.; Gromowski, G. D.; Matyas, G. R.; Rao, M.; Michael, N. L.; Modjarrad, K., SARS-CoV-2 ferritin nanoparticle vaccines elicit broad SARS coronavirus immunogenicity. *Cell Rep* **2021,** *37* (12), 110143.

8. Zhu, F. C.; Li, Y. H.; Guan, X. H.; Hou, L. H.; Wang, W. J.; Li, J. X.; Wu, S. P.; Wang, B. S.; Wang, Z.; Wang, L.; Jia, S. Y.; Jiang, H. D.; Wang, L.; Jiang, T.; Hu, Y.; Gou, J. B.; Xu, S. B.; Xu, J. J.; Wang, X. W.; Wang, W.; Chen, W., Safety, tolerability, and immunogenicity of a recombinant adenovirus type-5 vectored COVID-19 vaccine: a dose-escalation, open-label, non-randomised, first-in-human trial. *Lancet* **2020,** *395* (10240), 1845-1854.

9. van Doremalen, N.; Lambe, T.; Spencer, A.; Belij-Rammerstorfer, S.; Purushotham, J. N.; Port, J. R.; Avanzato, V. A.; Bushmaker, T.; Flaxman, A.; Ulaszewska, M.;

Feldmann, F.; Allen, E. R.; Sharpe, H.; Schulz, J.; Holbrook, M.; Okumura, A.; Meade-White, K.; Perez-Perez, L.; Edwards, N. J.; Wright, D.; Bissett, C.; Gilbride, C.; Williamson, B. N.; Rosenke, R.; Long, D.; Ishwarbhai, A.; Kailath, R.; Rose, L.; Morris, S.; Powers, C.; Lovaglio, J.; Hanley, P. W.; Scott, D.; Saturday, G.; de Wit, E.; Gilbert, S. C.; Munster, V. J., ChAdOx1 nCoV-19 vaccine prevents SARS-CoV-2 pneumonia in rhesus macaques. *Nature* **2020,** *586* (7830), 578-582.

10. Sadoff, J.; Gray, G.; Vandebosch, A.; Cardenas, V.; Shukarev, G.; Grinsztejn, B.; Goepfert, P. A.; Truyers, C.; Fennema, H.; Spiessens, B.; Offergeld, K.; Scheper, G.; Taylor, K. L.; Robb, M. L.; Treanor, J.; Barouch, D. H.; Stoddard, J.; Ryser, M. F.; Marovich, M. A.; Neuzil, K. M.; Corey, L.; Cauwenberghs, N.; Tanner, T.; Hardt, K.; Ruiz-Guinazu, J.; Le Gars, M.; Schuitemaker, H.; Van Hoof, J.; Struyf, F.; Douoguih, M.; Group, E. S., Safety and Efficacy of Single-Dose Ad26.COV2.S Vaccine against Covid-19. *N Engl J Med* **2021,** *384* (23), 2187-2201.

11. Gao, Q.; Bao, L.; Mao, H.; Wang, L.; Xu, K.; Yang, M.; Li, Y.; Zhu, L.; Wang, N.; Lv, Z.; Gao, H.; Ge, X.; Kan, B.; Hu, Y.; Liu, J.; Cai, F.; Jiang, D.; Yin, Y.; Qin, C.; Li, J.; Gong, X.; Lou, X.; Shi, W.; Wu, D.; Zhang, H.; Zhu, L.; Deng, W.; Li, Y.; Lu, J.; Li, C.; Wang, X.; Yin, W.; Zhang, Y.; Qin, C., Development of an inactivated vaccine candidate for SARS-CoV-2. *Science* **2020,** *369* (6499), 77-81.

12. Wang, H.; Zhang, Y.; Huang, B.; Deng, W.; Quan, Y.; Wang, W.; Xu, W.; Zhao, Y.; Li, N.; Zhang, J.; Liang, H.; Bao, L.; Xu, Y.; Ding, L.; Zhou, W.; Gao, H.; Liu, J.; Niu, P.; Zhao, L.; Zhen, W.; Fu, H.; Yu, S.; Zhang, Z.; Xu, G.; Li, C.; Lou, Z.; Xu, M.; Qin, C.; Wu, G.; Gao, G. F.; Tan, W.; Yang, X., Development of an Inactivated Vaccine Candidate, BBIBP-CorV, with Potent Protection against SARS-CoV-2. *Cell* **2020,** *182* (3), 713-721.

13. VanBlargan, L. A.; Errico, J. M.; Halfmann, P. J.; Zost, S. J.; Crowe, J. E., Jr.; Purcell, L. A.; Kawaoka, Y.; Corti, D.; Fremont, D. H.; Diamond, M. S., An infectious SARS-CoV-2 B.1.1.529 Omicron virus escapes neutralization by therapeutic monoclonal antibodies. *Nat Med* **2022,** *28* (3), 490-495.

14. Iketani, S.; Liu, L.; Guo, Y.; Liu, L.; Chan, J. F.; Huang, Y.; Wang, M.; Luo, Y.; Yu, J.; Chu, H.; Chik, K. K.; Yuen, T. T.; Yin, M. T.; Sobieszczyk, M. E.; Huang, Y.; Yuen, K. Y.; Wang, H. H.; Sheng, Z.; Ho, D. D., Antibody evasion properties of SARS-CoV-2 Omicron sublineages. *Nature* **2022,** *604* (7906), 553-556.

15. Planas, D.;   Saunders, N.;   Maes, P.;   Guivel-Benhassine, F.;   Planchais, C.; Buchrieser, J.;   Bolland, W. H.;   Porrot, F.;   Staropoli, I.;   Lemoine, F.;   Pere, H.;   Veyer, D.;   Puech, J.;   Rodary, J.;   Baele, G.;   Dellicour, S.;   Raymenants, J.;   Gorissen, S.; Geenen, C.;   Vanmechelen, B.;   Wawina-Bokalanga, T.;   Marti-Carreras, J.;   Cuypers, L.; Seve, A.;   Hocqueloux, L.;   Prazuck, T.;   Rey, F. A.;   Simon-Loriere, E.;   Bruel, T.; Mouquet, H.;   Andre, E.; Schwartz, O., Considerable escape of SARS-CoV-2 Omicron to antibody neutralization. *Nature* **2022,** *602* (7898), 671-675.

16. Takashita, E.;   Kinoshita, N.;   Yamayoshi, S.;   Sakai-Tagawa, Y.;   Fujisaki, S.;   Ito, M.; Iwatsuki-Horimoto, K.;   Chiba, S.;   Halfmann, P.;   Nagai, H.;   Saito, M.;   Adachi, E.; Sullivan, D.;   Pekosz, A.;   Watanabe, S.;   Maeda, K.;   Imai, M.;   Yotsuyanagi, H.; Mitsuya, H.;   Ohmagari, N.;   Takeda, M.;   Hasegawa, H.; Kawaoka, Y., Efficacy of Antibodies and Antiviral Drugs against Covid-19 Omicron Variant. *N Engl J Med* **2022,** *386* (10), 995-998.

17. Schulz, S. R.;   Hoffmann, M.;   Roth, E.;   Pracht, K.;   Burnett, D. L.;   Mazigi, O.; Schuh, W.;   Manger, B.;   Mielenz, D.;   Goodnow, C. C.;   Christ, D.;   Pohlmann, S.; Jack, H. M., Augmented neutralization of SARS-CoV-2 Omicron variant by boost vaccination and monoclonal antibodies. *Eur J Immunol* **2022,** *52* (6), 970-977.

18. Cao, Y.;   Wang, J.;   Jian, F.;   Xiao, T.;   Song, W.;   Yisimayi, A.;   Huang, W.;   Li, Q.; Wang, P.;   An, R.;   Wang, J.;   Wang, Y.;   Niu, X.;   Yang, S.;   Liang, H.;   Sun, H.;   Li, T.;   Yu, Y.;   Cui, Q.;   Liu, S.;   Yang, X.;   Du, S.;   Zhang, Z.;   Hao, X.;   Shao, F.;   Jin, R.;   Wang, X.;   Xiao, J.;   Wang, Y.; Xie, X. S., Omicron escapes the majority of existing SARS-CoV-2 neutralizing antibodies. *Nature* **2022,** *602* (7898), 657-663.

19. Hoffmann, M.;   Kruger, N.;   Schulz, S.;   Cossmann, A.;   Rocha, C.;   Kempf, A.; Nehlmeier, I.;   Graichen, L.;   Moldenhauer, A. S.;   Winkler, M. S.;   Lier, M.;   Dopfer-Jablonka, A.;   Jack, H. M.;   Behrens, G. M. N.; Pohlmann, S., The Omicron variant is highly resistant against antibody-mediated neutralization: Implications for control of the COVID-19 pandemic. *Cell* **2022,** *185* (3), 447-456.

20. Liu, L.;   Iketani, S.;   Guo, Y.;   Chan, J. F.;   Wang, M.;   Liu, L.;   Luo, Y.;   Chu, H.; Huang, Y.;   Nair, M. S.;   Yu, J.;   Chik, K. K.;   Yuen, T. T.;   Yoon, C.;   To, K. K.;   Chen, H.;   Yin, M. T.;   Sobieszczyk, M. E.;   Huang, Y.;   Wang, H. H.;   Sheng, Z.;   Yuen, K. Y.; Ho, D. D., Striking antibody evasion manifested by the Omicron variant of SARS-CoV-2. *Nature* **2022,** *602* (7898), 676-681.

21. Zou, J.; Xia, H.; Xie, X.; Kurhade, C.; Machado, R. R. G.; Weaver, S. C.; Ren, P.; Shi, P. Y., Neutralization against Omicron SARS-CoV-2 from previous non-Omicron infection. *Nat Commun* **2022,** *13* (1), 852.

22. Altarawneh, H. N.; Chemaitelly, H.; Hasan, M. R.; Ayoub, H. H.; Qassim, S.; AlMukdad, S.; Coyle, P.; Yassine, H. M.; Al-Khatib, H. A.; Benslimane, F. M.; Al-Kanaani, Z.; Al-Kuwari, E.; Jeremijenko, A.; Kaleeckal, A. H.; Latif, A. N.; Shaik, R. M.; Abdul-Rahim, H. F.; Nasrallah, G. K.; Al-Kuwari, M. G.; Butt, A. A.; Al-Romaihi, H. E.; Al-Thani, M. H.; Al-Khal, A.; Bertollini, R.; Tang, P.; Abu-Raddad, L. J., Protection against the Omicron Variant from Previous SARS-CoV-2 Infection. *N Engl J Med* **2022,** *386* (13), 1288-1290.

23. Lusvarghi, S.; Pollett, S. D.; Neerukonda, S. N.; Wang, W.; Wang, R.; Vassell, R.; Epsi, N. J.; Fries, A. C.; Agan, B. K.; Lindholm, D. A.; Colombo, C. J.; Mody, R.; Ewers, E. C.; Lalani, T.; Ganesan, A.; Goguet, E.; Hollis-Perry, M.; Coggins, S. A.; Simons, M. P.; Katzelnick, L. C.; Wang, G.; Tribble, D. R.; Bentley, L.; Eakin, A. E.; Broder, C. C.; Erlandson, K. J.; Laing, E. D.; Burgess, T. H.; Mitre, E.; Weiss, C. D., SARS-CoV-2 BA.1 variant is neutralized by vaccine booster-elicited serum but evades most convalescent serum and therapeutic antibodies. *Sci Transl Med* **2022,** *14* (645), eabn8543. DOI: 10.1126/scitranslmed.abn8543.

24. Chaguza, C.; Coppi, A.; Earnest, R.; Ferguson, D.; Kerantzas, N.; Warner, F.; Young, H. P.; Breban, M. I.; Billig, K.; Koch, R. T.; Pham, K.; Kalinich, C. C.; Ott, I. M.; Fauver, J. R.; Hahn, A. M.; Tikhonova, I. R.; Castaldi, C.; De Kumar, B.; Pettker, C. M.; Warren, J. L.; Weinberger, D. M.; Landry, M. L.; Peaper, D. R.; Schulz, W.; Vogels, C. B. F.; Grubaugh, N. D., Rapid emergence of SARS-CoV-2 Omicron variant is associated with an infection advantage over Delta in vaccinated persons. *Med* **2022,** *3* (5), 325-334.

25. Lipsitch, M.; Krammer, F.; Regev-Yochay, G.; Lustig, Y.; Balicer, R. D., SARS-CoV-2 breakthrough infections in vaccinated individuals: measurement, causes and impact. *Nat Rev Immunol* **2022,** *22* (1), 57-65.

26. Levine-Tiefenbrun, M.; Yelin, I.; Alapi, H.; Herzel, E.; Kuint, J.; Chodick, G.; Gazit, S.; Patalon, T.; Kishony, R., Waning of SARS-CoV-2 booster viral-load reduction effectiveness. *Nat Commun* **2022,** *13* (1), 1237.

27. Braeye, T.; Catteau, L.; Brondeel, R.; van Loenhout, J. A. F.; Proesmans, K.; Cornelissen, L.; Van Oyen, H.; Stouten, V.; Hubin, P.; Billuart, M.; Djiena, A.;

Mahieu, R.; Hammami, N.; Van Cauteren, D.; Wyndham-Thomas, C., Vaccine effectiveness against onward transmission of SARS-CoV2-infection by variant of concern and time since vaccination, Belgian contact tracing, 2021. *Vaccine* **2022,** *40* (22), 3027-3037.

28. Perez-Alos, L.; Armenteros, J. J. A.; Madsen, J. R.; Hansen, C. B.; Jarlhelt, I.; Hamm, S. R.; Heftdal, L. D.; Pries-Heje, M. M.; Moller, D. L.; Fogh, K.; Hasselbalch, R. B.; Rosbjerg, A.; Brunak, S.; Sorensen, E.; Larsen, M. A. H.; Ostrowski, S. R.; Frikke-Schmidt, R.; Bayarri-Olmos, R.; Hilsted, L. M.; Iversen, K. K.; Bundgaard, H.; Nielsen, S. D.; Garred, P., Modeling of waning immunity after SARS-CoV-2 vaccination and influencing factors. *Nat Commun* **2022,** *13* (1), 1614.

29. Tartof, S. Y.; Slezak, J. M.; Puzniak, L.; Hong, V.; Xie, F.; Ackerson, B. K.; Valluri, S. R.; Jodar, L.; McLaughlin, J. M., Durability of BNT162b2 vaccine against hospital and emergency department admissions due to the omicron and delta variants in a large health system in the USA: a test-negative case-control study. *Lancet Respir Med* **2022,** *10* (7), 689-699.

30. Israel, A.; Shenhar, Y.; Green, I.; Merzon, E.; Golan-Cohen, A.; Schäffer, A. A.; Ruppin, E.; Vinker, S.; Magen, E., Large-Scale Study of Antibody Titer Decay Following BNT162b2 mRNA Vaccine or SARS-CoV-2 Infection. *Vaccines* **2022,** *10* (1), 64.

31. Tang, J.; Zeng, C.; Cox, T. M.; Li, C.; Son, Y. M.; Cheon, I. S.; Wu, Y.; Behl, S.; Taylor, J. J.; Chakaraborty, R.; Johnson, A. J.; Shiavo, D. N.; Utz, J. P.; Reisenauer, J. S.; Midthun, D. E.; Mullon, J. J.; Edell, E. S.; Alameh, M. G.; Borish, L.; Teague, W. G.; Kaplan, M. H.; Weissman, D.; Kern, R.; Hu, H.; Vassallo, R.; Liu, S. L.; Sun, J., Respiratory mucosal immunity against SARS-CoV-2 after mRNA vaccination. *Sci Immunol* **2022,** *7* (76), eadd4853. DOI: 10.1126/sciimmunol.add4853.

32. Valencia, D. N., Brief Review on COVID-19: The 2020 Pandemic Caused by SARS-CoV-2. *Cureus* **2020,** *12* (3), e7386. DOI: 10.7759/cureus.7386.

33. Du, L.; He, Y.; Zhou, Y.; Liu, S.; Zheng, B. J.; Jiang, S., The spike protein of SARS-CoV--a target for vaccine and therapeutic development. *Nat Rev Microbiol* **2009,** *7* (3), 226-36.

34. Shang, J.; Wan, Y.; Luo, C.; Ye, G.; Geng, Q.; Auerbach, A.; Li, F., Cell entry mechanisms of SARS-CoV-2. *Proc Natl Acad Sci U S A* **2020,** *117* (21), 11727-11734.

35. Belouzard, S.; Millet, J. K.; Licitra, B. N.; Whittaker, G. R., Mechanisms of coronavirus cell entry mediated by the viral spike protein. *Viruses* **2012,** *4* (6), 1011-1033.

36. Li, F., Structure, Function, and Evolution of Coronavirus Spike Proteins. *Annu Rev Virol* **2016,** *3* (1), 237-261.

37. Yang, J.; Wang, W.; Chen, Z.; Lu, S.; Yang, F.; Bi, Z.; Bao, L.; Mo, F.; Li, X.; Huang, Y.; Hong, W.; Yang, Y.; Zhao, Y.; Ye, F.; Lin, S.; Deng, W.; Chen, H.; Lei, H.; Zhang, Z.; Luo, M.; Gao, H.; Zheng, Y.; Gong, Y.; Jiang, X.; Xu, Y.; Lv, Q.; Li, D.; Wang, M.; Li, F.; Wang, S.; Wang, G.; Yu, P.; Qu, Y.; Yang, L.; Deng, H.; Tong, A.; Li, J.; Wang, Z.; Yang, J.; Shen, G.; Zhao, Z.; Li, Y.; Luo, J.; Liu, H.; Yu, W.; Yang, M.; Xu, J.; Wang, J.; Li, H.; Wang, H.; Kuang, D.; Lin, P.; Hu, Z.; Guo, W.; Cheng, W.; He, Y.; Song, X.; Chen, C.; Xue, Z.; Yao, S.; Chen, L.; Ma, X.; Chen, S.; Gou, M.; Huang, W.; Wang, Y.; Fan, C.; Tian, Z.; Shi, M.; Wang, F. S.; Dai, L.; Wu, M.; Li, G.; Wang, G.; Peng, Y.; Qian, Z.; Huang, C.; Lau, J. Y.; Yang, Z.; Wei, Y.; Cen, X.; Peng, X.; Qin, C.; Zhang, K.; Lu, G.; Wei, X., A vaccine targeting the RBD of the S protein of SARS-CoV-2 induces protective immunity. *Nature* **2020,** *586* (7830), 572-577.

38. Pinto, D.; Park, Y. J.; Beltramello, M.; Walls, A. C.; Tortorici, M. A.; Bianchi, S.; Jaconi, S.; Culap, K.; Zatta, F.; De Marco, A.; Peter, A.; Guarino, B.; Spreafico, R.; Cameroni, E.; Case, J. B.; Chen, R. E.; Havenar-Daughton, C.; Snell, G.; Telenti, A.; Virgin, H. W.; Lanzavecchia, A.; Diamond, M. S.; Fink, K.; Veesler, D.; Corti, D., Cross-neutralization of SARS-CoV-2 by a human monoclonal SARS-CoV antibody. *Nature* **2020,** *583* (7815), 290-295.

39. Hastie, K. M.; Li, H.; Bedinger, D.; Schendel, S. L.; Dennison, S. M.; Li, K.; Rayaprolu, V.; Yu, X.; Mann, C.; Zandonatti, M.; Diaz Avalos, R.; Zyla, D.; Buck, T.; Hui, S.; Shaffer, K.; Hariharan, C.; Yin, J.; Olmedillas, E.; Enriquez, A.; Parekh, D.; Abraha, M.; Feeney, E.; Horn, G. Q.; Co, V. I. C. D. B. t.; Aldon, Y.; Ali, H.; Aracic, S.; Cobb, R. R.; Federman, R. S.; Fernandez, J. M.; Glanville, J.; Green, R.; Grigoryan, G.; Lujan Hernandez, A. G.; Ho, D. D.; Huang, K. A.; Ingraham, J.; Jiang, W.; Kellam, P.; Kim, C.; Kim, M.; Kim, H. M.; Kong, C.; Krebs, S. J.; Lan, F.; Lang, G.; Lee, S.; Leung, C. L.; Liu, J.; Lu, Y.; MacCamy, A.; McGuire, A. T.; Palser, A. L.; Rabbitts, T. H.; Rikhtegaran Tehrani, Z.; Sajadi, M. M.; Sanders, R. W.; Sato, A. K.; Schweizer, L.; Seo, J.; Shen, B.; Snitselaar, J. L.; Stamatatos, L.; Tan, Y.; Tomic, M. T.; van Gils, M. J.; Youssef, S.; Yu, J.; Yuan, T. Z.; Zhang, Q.; Peters, B.; Tomaras, G. D.; Germann, T.; Saphire, E. O., Defining variant-resistant epitopes targeted by SARS-CoV-2 antibodies: A global consortium study. *Science* **2021,** *374* (6566), 472-478.

40. Lan, J.; Ge, J.; Yu, J.; Shan, S.; Zhou, H.; Fan, S.; Zhang, Q.; Shi, X.; Wang, Q.; Zhang, L.; Wang, X., Structure of the SARS-CoV-2 spike receptor-binding domain bound to the ACE2 receptor. *Nature* **2020,** *581* (7807), 215-220.

41. Xu, B.; Tian, L.; Chen, J.; Wang, J.; Ma, R.; Dong, W.; Li, A.; Zhang, J.; Antonio Chiocca, E.; Kaur, B.; Feng, M.; Caligiuri, M. A.; Yu, J., An oncolytic virus expressing a full-length antibody enhances antitumor innate immune response to glioblastoma. *Nat Commun* **2021,** *12* (1), 5908.

42. Zhao, Q.; Gao, Y.; Xiao, M.; Huang, X.; Wu, X., Synthesis and immunological evaluation of synthetic peptide based anti-SARS-CoV-2 vaccine candidates. *Chem Commun (Camb)* **2021,** *57* (12), 1474-1477.

43. Sungsuwan, S.; Wu, X.; Shaw, V.; Kavunja, H.; McFall-Boegeman, H.; Rashidijahanabad, Z.; Tan, Z.; Lang, S.; Tahmasebi Nick, S.; Lin, P. H.; Yin, Z.; Ramadan, S.; Jin, X.; Huang, X., Structure Guided Design of Bacteriophage Qbeta Mutants as Next Generation Carriers for Conjugate Vaccines. *ACS Chem Biol* **2022,** *17* (11), 3047-3058.

44. Golmohammadi, R.; Fridborg, K.; Bundule, M.; Valegard, K.; Liljas, L., The crystal structure of bacteriophage Q beta at 3.5 A resolution. *Structure* **1996,** *4* (5), 543-554.

45. Yin, Z.; Comellas-Aragones, M.; Chowdhury, S.; Bentley, P.; Kaczanowska, K.; Benmohamed, L.; Gildersleeve, J. C.; Finn, M. G.; Huang, X., Boosting immunity to small tumor-associated carbohydrates with bacteriophage qbeta capsids. *ACS Chem Biol* **2013,** *8* (6), 1253-1262.

46. Yin, Z.; Wu, X.; Kaczanowska, K.; Sungsuwan, S.; Comellas Aragones, M.; Pett, C.; Yu, J.; Baniel, C.; Westerlind, U.; Finn, M. G.; Huang, X., Antitumor Humoral and T Cell Responses by Mucin-1 Conjugates of Bacteriophage Qbeta in Wild-type Mice. *ACS Chem Biol* **2018,** *13* (6), 1668-1676.

47. Wu, X.; McKay, C.; Pett, C.; Yu, J.; Schorlemer, M.; Ramadan, S.; Lang, S.; Behren, S.; Westerlind, U.; Finn, M. G.; Huang, X., Synthesis and Immunological Evaluation of Disaccharide Bearing MUC-1 Glycopeptide Conjugates with Virus-like Particles. *ACS Chem Biol* **2019,** *14* (10), 2176-2184.

48. Wu, X.; Yin, Z.; McKay, C.; Pett, C.; Yu, J.; Schorlemer, M.; Gohl, T.; Sungsuwan, S.; Ramadan, S.; Baniel, C.; Allmon, A.; Das, R.; Westerlind, U.; Finn, M.

G.; Huang, X., Protective Epitope Discovery and Design of MUC1-based Vaccine for Effective Tumor Protections in Immunotolerant Mice. *J Am Chem Soc* **2018,** *140* (48), 16596-16609.

49. Wang, G.; Kang, X.; Chen, K. S.; Jehng, T.; Jones, L.; Chen, J.; Huang, X. F.; Chen, S. Y., An engineered oncolytic virus expressing PD-L1 inhibitors activates tumor neoantigen-specific T cell responses. *Nat Commun* **2020,** *11* (1), 1395.

50. Cai, Y.; Zhang, J.; Xiao, T.; Peng, H.; Sterling, S. M.; Walsh, R. M., Jr.; Rawson, S.; Rits-Volloch, S.; Chen, B., Distinct conformational states of SARS-CoV-2 spike protein. *Science* **2020,** *369* (6511), 1586-1592.

51. Pettersen, E. F.; Goddard, T. D.; Huang, C. C.; Meng, E. C.; Couch, G. S.; Croll, T. I.; Morris, J. H.; Ferrin, T. E., UCSF ChimeraX: Structure visualization for researchers, educators, and developers. *Protein Sci* **2021,** *30* (1), 70-82.

52. Chakraborty, S.; Gonzalez, J. C.; Sievers, B. L.; Mallajosyula, V.; Chakraborty, S.; Dubey, M.; Ashraf, U.; Cheng, B. Y.; Kathale, N.; Tran, K. Q. T.; Scallan, C.; Sinnott, A.; Cassidy, A.; Chen, S. T.; Gelbart, T.; Gao, F.; Golan, Y.; Ji, X.; Kim-Schulze, S.; Prahl, M.; Gaw, S. L.; Gnjatic, S.; Marron, T. U.; Merad, M.; Arunachalam, P. S.; Boyd, S. D.; Davis, M. M.; Holubar, M.; Khosla, C.; Maecker, H. T.; Maldonado, Y.; Mellins, E. D.; Nadeau, K. C.; Pulendran, B.; Singh, U.; Subramanian, A.; Utz, P. J.; Sherwood, R.; Zhang, S.; Jagannathan, P.; Tan, G. S.; Wang, T. T., Early non-neutralizing, afucosylated antibody responses are associated with COVID-19 severity. *Sci Transl Med* **2022,** *14* (635), eabm7853. DOI: 10.1126/scitranslmed.abm7853.

53. Junqueira, C.; Crespo, A.; Ranjbar, S.; de Lacerda, L. B.; Lewandrowski, M.; Ingber, J.; Parry, B.; Ravid, S.; Clark, S.; Schrimpf, M. R.; Ho, F.; Beakes, C.; Margolin, J.; Russell, N.; Kays, K.; Boucau, J.; Das Adhikari, U.; Vora, S. M.; Leger, V.; Gehrke, L.; Henderson, L. A.; Janssen, E.; Kwon, D.; Sander, C.; Abraham, J.; Goldberg, M. B.; Wu, H.; Mehta, G.; Bell, S.; Goldfeld, A. E.; Filbin, M. R.; Lieberman, J., FcgammaR-mediated SARS-CoV-2 infection of monocytes activates inflammation. *Nature* **2022,** *606* (7914), 576-584.

54. Tan, C. W.; Chia, W. N.; Qin, X.; Liu, P.; Chen, M. I.; Tiu, C.; Hu, Z.; Chen, V. C.; Young, B. E.; Sia, W. R.; Tan, Y. J.; Foo, R.; Yi, Y.; Lye, D. C.; Anderson, D. E.; Wang, L. F., A SARS-CoV-2 surrogate virus neutralization test based on antibody-mediated blockage of ACE2-spike protein-protein interaction. *Nat Biotechnol* **2020,** *38* (9), 1073-1078.

55. Meyer, B.; Reimerink, J.; Torriani, G.; Brouwer, F.; Godeke, G. J.; Yerly, S.; Hoogerwerf, M.; Vuilleumier, N.; Kaiser, L.; Eckerle, I.; Reusken, C., Validation and clinical evaluation of a SARS-CoV-2 surrogate virus neutralisation test (sVNT). *Emerg Microbes Infect* **2020,** *9* (1), 2394-2403.

56. Moss, P., The T cell immune response against SARS-CoV-2. *Nat Immunol* **2022,** *23* (2), 186-193.

57. de Candia, P.; Prattichizzo, F.; Garavelli, S.; Matarese, G., T Cells: Warriors of SARS-CoV-2 Infection. *Trends Immunol* **2021,** *42* (1), 18-30.

58. Roldao, A.; Mellado, M. C.; Castilho, L. R.; Carrondo, M. J.; Alves, P. M., Virus-like particles in vaccine development. *Expert Rev Vaccines* **2010,** *9* (10), 1149-1176.

59. Frietze, K. M.; Peabody, D. S.; Chackerian, B., Engineering virus-like particles as vaccine platforms. *Curr Opin Virol* **2016,** *18*, 44-49.

60. Brouwer, P. J. M.; Brinkkemper, M.; Maisonnasse, P.; Dereuddre-Bosquet, N.; Grobben, M.; Claireaux, M.; de Gast, M.; Marlin, R.; Chesnais, V.; Diry, S.; Allen, J. D.; Watanabe, Y.; Giezen, J. M.; Kerster, G.; Turner, H. L.; van der Straten, K.; van der Linden, C. A.; Aldon, Y.; Naninck, T.; Bontjer, I.; Burger, J. A.; Poniman, M.; Mykytyn, A. Z.; Okba, N. M. A.; Schermer, E. E.; van Breemen, M. J.; Ravichandran, R.; Caniels, T. G.; van Schooten, J.; Kahlaoui, N.; Contreras, V.; Lemaitre, J.; Chapon, C.; Fang, R. H. T.; Villaudy, J.; Sliepen, K.; van der Velden, Y. U.; Haagmans, B. L.; de Bree, G. J.; Ginoux, E.; Ward, A. B.; Crispin, M.; King, N. P.; van der Werf, S.; van Gils, M. J.; Le Grand, R.; Sanders, R. W., Two-component spike nanoparticle vaccine protects macaques from SARS-CoV-2 infection. *Cell* **2021,** *184* (5), 1188-1200.

61. Tan, T. K.; Rijal, P.; Rahikainen, R.; Keeble, A. H.; Schimanski, L.; Hussain, S.; Harvey, R.; Hayes, J. W. P.; Edwards, J. C.; McLean, R. K.; Martini, V.; Pedrera, M.; Thakur, N.; Conceicao, C.; Dietrich, I.; Shelton, H.; Ludi, A.; Wilsden, G.; Browning, C.; Zagrajek, A. K.; Bialy, D.; Bhat, S.; Stevenson-Leggett, P.; Hollinghurst, P.; Tully, M.; Moffat, K.; Chiu, C.; Waters, R.; Gray, A.; Azhar, M.; Mioulet, V.; Newman, J.; Asfor, A. S.; Burman, A.; Crossley, S.; Hammond, J. A.; Tchilian, E.; Charleston, B.; Bailey, D.; Tuthill, T. J.; Graham, S. P.; Duyvesteyn, H. M. E.; Malinauskas, T.; Huo, J.; Tree, J. A.; Buttigieg, K. R.; Owens, R. J.; Carroll, M. W.; Daniels, R. S.; McCauley, J. W.; Stuart, D. I.; Huang, K. A.; Howarth, M.; Townsend, A. R., A COVID-19 vaccine candidate using SpyCatcher multimerization of the SARS-CoV-2 spike protein receptor-binding domain induces potent neutralising antibody responses. *Nat Commun* **2021,** *12* (1), 542.

62. Bachmann, M. F.; Rohrer, U. H.; Kundig, T. M.; Burki, K.; Hengartner, H.; Zinkernagel, R. M., The influence of antigen organization on B cell responsiveness. *Science* **1993,** *262* (5138), 1448-1451.

63. Braun, M.; Jandus, C.; Maurer, P.; Hammann-Haenni, A.; Schwarz, K.; Bachmann, M. F.; Speiser, D. E.; Romero, P., Virus-like particles induce robust human T-helper cell responses. *Eur J Immunol* **2012,** *42* (2), 330-340.

64. Skibinski, D. A.; Hanson, B. J.; Lin, Y.; von Messling, V.; Jegerlehner, A.; Tee, J. B.; Chye de, H.; Wong, S. K.; Ng, A. A.; Lee, H. Y.; Au, B.; Lee, B. T.; Santoso, L.; Poidinger, M.; Fairhurst, A. M.; Matter, A.; Bachmann, M. F.; Saudan, P.; Connolly, J. E., Enhanced neutralizing antibody titers and Th1 polarization from a novel Escherichia coli derived pandemic influenza vaccine. *PLoS One* **2013,** *8* (10), 0076571. DOI: 10.1371/journal.pone.0076571.

65. Burton, D. R., Antibodies, viruses and vaccines. *Nat Rev Immunol* **2002,** *2* (9), 706-713.

66. Correia, B. E.; Bates, J. T.; Loomis, R. J.; Baneyx, G.; Carrico, C.; Jardine, J. G.; Rupert, P.; Correnti, C.; Kalyuzhniy, O.; Vittal, V.; Connell, M. J.; Stevens, E.; Schroeter, A.; Chen, M.; Macpherson, S.; Serra, A. M.; Adachi, Y.; Holmes, M. A.; Li, Y.; Klevit, R. E.; Graham, B. S.; Wyatt, R. T.; Baker, D.; Strong, R. K.; Crowe, J. E., Jr.; Johnson, P. R.; Schief, W. R., Proof of principle for epitope-focused vaccine design. *Nature* **2014,** *507* (7491), 201-206.

67. Tan, H. X.; Jegaskanda, S.; Juno, J. A.; Esterbauer, R.; Wong, J.; Kelly, H. G.; Liu, Y.; Tilmanis, D.; Hurt, A. C.; Yewdell, J. W.; Kent, S. J.; Wheatley, A. K., Subdominance and poor intrinsic immunogenicity limit humoral immunity targeting influenza HA stem. *J Clin Invest* **2019,** *129* (2), 850-862.

68. Azoitei, M. L.; Correia, B. E.; Ban, Y. E.; Carrico, C.; Kalyuzhniy, O.; Chen, L.; Schroeter, A.; Huang, P. S.; McLellan, J. S.; Kwong, P. D.; Baker, D.; Strong, R. K.; Schief, W. R., Computation-guided backbone grafting of a discontinuous motif onto a protein scaffold. *Science* **2011,** *334* (6054), 373-376.

69. Sahoo, A.; Wali, S.; Nurieva, R., T helper 2 and T follicular helper cells: Regulation and function of interleukin-4. *Cytokine Growth Factor Rev* **2016,** *30*, 29-37.

70. Hong, S.; Zhang, Z.; Liu, H.; Tian, M.; Zhu, X.; Zhang, Z.; Wang, W.; Zhou, X.; Zhang, F.; Ge, Q.; Zhu, B.; Tang, H.; Hua, Z.; Hou, B., B Cells Are the Dominant Antigen-

Presenting Cells that Activate Naive CD4(+) T Cells upon Immunization with a Virus-Derived Nanoparticle Antigen. *Immunity* **2018,** *49* (4), 695-708.

71. Hua, Z.; Hou, B., The role of B cell antigen presentation in the initiation of CD4+ T cell response. *Immunol Rev* **2020,** *296* (1), 24-35.

72. Koutsakos, M.; Lee, W. S.; Wheatley, A. K.; Kent, S. J.; Juno, J. A., T follicular helper cells in the humoral immune response to SARS-CoV-2 infection and vaccination. *J Leukoc Biol* **2022,** *111* (2), 355-365.

73. Boppana, S.; Qin, K.; Files, J. K.; Russell, R. M.; Stoltz, R.; Bibollet-Ruche, F.; Bansal, A.; Erdmann, N.; Hahn, B. H.; Goepfert, P. A., SARS-CoV-2-specific circulating T follicular helper cells correlate with neutralizing antibodies and increase during early convalescence. *PLoS Pathog* **2021,** *17* (7), 1009761. DOI: 10.1371/journal.ppat.1009761.

74. Liu, L.; Wang, P.; Nair, M. S.; Yu, J.; Rapp, M.; Wang, Q.; Luo, Y.; Chan, J. F.; Sahi, V.; Figueroa, A.; Guo, X. V.; Cerutti, G.; Bimela, J.; Gorman, J.; Zhou, T.; Chen, Z.; Yuen, K. Y.; Kwong, P. D.; Sodroski, J. G.; Yin, M. T.; Sheng, Z.; Huang, Y.; Shapiro, L.; Ho, D. D., Potent neutralizing antibodies against multiple epitopes on SARS-CoV-2 spike. *Nature* **2020,** *584* (7821), 450-456.

75. Yuan, M.; Liu, H.; Wu, N. C.; Lee, C. D.; Zhu, X.; Zhao, F.; Huang, D.; Yu, W.; Hua, Y.; Tien, H.; Rogers, T. F.; Landais, E.; Sok, D.; Jardine, J. G.; Burton, D. R.; Wilson, I. A., Structural basis of a shared antibody response to SARS-CoV-2. *Science* **2020,** *369* (6507), 1119-1123.

76. Shi, R.; Shan, C.; Duan, X.; Chen, Z.; Liu, P.; Song, J.; Song, T.; Bi, X.; Han, C.; Wu, L.; Gao, G.; Hu, X.; Zhang, Y.; Tong, Z.; Huang, W.; Liu, W. J.; Wu, G.; Zhang, B.; Wang, L.; Qi, J.; Feng, H.; Wang, F. S.; Wang, Q.; Gao, G. F.; Yuan, Z.; Yan, J., A human neutralizing antibody targets the receptor-binding site of SARS-CoV-2. *Nature* **2020,** *584* (7819), 120-124.

77. Ito, R.; Ozaki, Y. A.; Yoshikawa, T.; Hasegawa, H.; Sato, Y.; Suzuki, Y.; Inoue, R.; Morishima, T.; Kondo, N.; Sata, T.; Kurata, T.; Tamura, S., Roles of anti-hemagglutinin IgA and IgG antibodies in different sites of the respiratory tract of vaccinated mice in preventing lethal influenza pneumonia. *Vaccine* **2003,** *21* (19-20), 2362-2371.

Chapter 3 A comprehensive synthetic library of poly-N-acetyl glucosamines enabled vaccine against lethal challenges of *Staphylococcus aureus*

Adapted from Tan, Z., Yang, W., O'Brien, N. A., Pan, X., Ramadan, S. Marsh, T., Hammer, N. Cywes-Bentley, C., Vinacur, M., Pier, G. B., Gildersleeve, J. C., Huang, X.. A comprehensive synthetic library of poly-N-acetyl glucosamines enabled vaccine against lethal challenges of *Staphylococcus aureus*. *Nat Commun* **2024**, *15* (1), 3420.

3.1 Introduction

Bacterial infections continue to threaten global health, and this situation is further exacerbated by the prevalence of antimicrobial resistant strains including those resistant to multiple drugs. In 2019, the Center for Disease Control and Prevention (CDC) estimated that 3 million antimicrobial-resistant infections occurred in the USA annually.[1] Antibiotic resistance is rising to dangerously high levels in all parts of the world with resistance in some pathogens observed to nearly all antibiotics that have been developed.[2] New strategies to prevent and treat infections are urgently needed.

Parallel to the development of new antibiotics, vaccination is an important approach for combating pathogens.[3] Multiple antimicrobial vaccines have been implemented against infections such as those by *Clostridium tetani*, *Bordetella pertussis* and *Streptococcus pneumoniae*. However, despite these successes, there are no approved vaccines against many other deadly pathogens including *Staphylococcus aureus* (*S. aureus*), which caused over 300,000 infections and 20,000 deaths through bloodstream infection in 2017 in the US.[1] The prevalence of methicillin-resistant

S. aureus (MRSA) further highlights the need for a vaccine to stem the rise of anti-microbial resistance.[4]

A major challenge in vaccine design is the selection of a suitable antigen. The envelope and biofilm of *S. aureus* as well as numerous other bacterial, fungal, and protozoal parasites contains the polysaccharide poly-β-(1−6)-*N*-acetylglucosamine (PNAG), which is composed of β-(1−6) linked glucosamine units with 80-95% of them *N*-acetylated.[5-8] Naturally occurring PNAG can vary in its chemical structures with the amino groups in some glucosamine existing as free amines rather than as *N*-acetamides (NHAc).[9] The differing degrees and positions of free amines *vs* NHAc in PNAG can result in high structural heterogeneity, and the precise PNAG structures from bacteria are not known. Present on the cell surface and as an integral component of the biofilm, PNAG has been found to be an important virulence factor that aids the bacterial evasion of the immune system.[5, 10] The widespread expression of PNAG in multiple pathogenic microbes and its important roles in pathogenesis render it an attractive target for vaccine development.

The immunological properties of PNAG have been investigated.[5, 11] PNAG pentasaccharides and nonasaccharides with all amine groups either free or fully acetylated have been synthesized and subsequently conjugated with an immunogenic protein carrier, tetanus toxoid (TT).[12-14] Mouse immunization studies showed that the TT-conjugates with the PNAG bearing all amines could induce protective immunity, while the antibodies elicited by the TT conjugates with fully acetylated PNAG counterparts failed to mediate protective functions such as opsonic killing and

in vivo protection.[11] Despite this interesting finding, PNAG based vaccines investigated to date only contained the glycans with all amine groups either free or fully acetylated. It is not clear what PNAG structure would comprise the best epitope(s) for maximal protective immunity, and whether specific patterns of amine *vs* acetylation in PNAG can be designed to enhance vaccine efficacy.

To gain a deeper understanding of the impact of variably acetylated PNAG epitopes, diverse structurally defined PNAG sequences are critically needed. In this work, we report a divergent strategy enabling the synthesis of a comprehensive library of 32 PNAG pentasaccharides with all possible combinations of the location and the number of free amines incorporated into the oligosaccharide. The availability of such a library enables us to establish the amine/acetylation code (locations of the free amine/NHAc in PNAG) of an anti-PNAG mAb. The fine patterns of free amine/NHAc of PNAG oligosaccharides are found to be critical for mAb binding. The structural patterns identified through the microarray study has guided the selection of PNAG epitopes for the design for next generation vaccine, which provide highly effective protection in multiple mouse models against *S. aureus* infections, including those by MRSA.
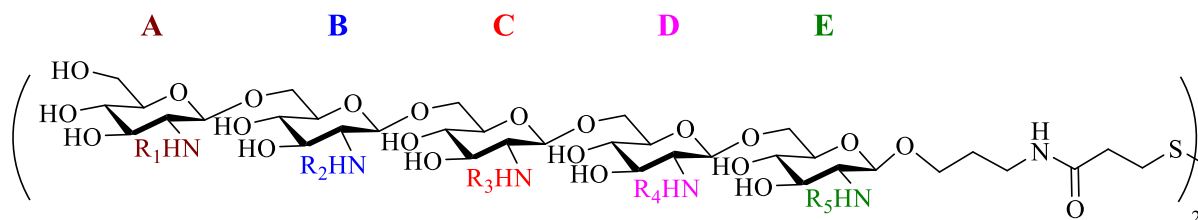
3.2 Results and discussion

3.2.1 Synthesis of the PNAG oligosaccharide library

To date, only fully acetylated PNAG and fully deacetylated PNAG have been investigated as immunogens for vaccine studies.[12-14] The availability of a library of PNAG oligosaccharides with systematically varied numbers and locations of free amines can greatly aid in the understanding of

the protective epitope structure. My coworker, Dr. Weizhun Yang, synthesized a comprehensive

library of 32 pentasaccharides PNAG0-PNAG31 fully covering the free amine space of PNAG.

The reducing ends of the target pentasaccharides bear a linker terminated with a disulfide group,

which can be reduced for chemoselective conjugation to a carrier protein.

The synthesis of the full 32 possible PNAG pentasaccharides was conducted by Dr. Weizhun

Yang. **Figure 3.1** presents the structure and numbering of the pentasaccharide library. A brief

protocol for the synthesis is listed in the Appendices.

PNAG0 (00000): R_1, R_2, R_3, R_4, R_5 = H;
PNAG1 (00001): R_1, R_2, R_3, R_4 = H; R_5 = Ac
PNAG2 (00010): R_1, R_2, R_3, R_5 = H; R_4 = Ac
PNAG3 (00011): R_1, R_2, R_3 = H; R_4, R_5 = Ac
PNAG4 (00100): R_1, R_2, R_4, R_5 = H; R_3 = Ac
PNAG5 (00101): R_1, R_2, R_4 = H; R_3, R_5 = Ac
PNAG6 (00110): R_1, R_2, R_5 = H; R_3, R_4 = Ac
PNAG7 (00111): R_1, R_2 = H; R_3, R_4, R_5 = Ac
PNAG8 (01000): R_1, R_3, R_4, R_5 = H; R_2 = Ac
PNAG9 (01001): R_1, R_3, R_4 = H; R_2, R_5 = Ac
PNAG10 (01010): R_1, R_3, R_4 = H; R_2, R_4 = Ac
PNAG11 (01011): R_1, R_3 = H; R_2, R_4, R_5 = Ac
PNAG12 (01100): R_1, R_4, R_5 = H; R_2, R_3 = Ac
PNAG13 (01101): R_1, R_4 = H; R_2, R_3, R_5 = Ac
PNAG14 (01110): R_1, R_5 = H; R_2, R_3, R_4 = Ac
PNAG15 (01111): R_1 = H; R_2, R_3, R_4, R_5 = Ac

PNAG16 (10000): R_2, R_3, R_4, R_5 = H; R_1 = Ac
PNAG17 (10001): R_2, R_3, R_4 = H; R_1, R_5 = Ac
PNAG18 (10010): R_2, R_3, R_5 = H; R_1, R_4 = Ac
PNAG19 (10011): R_2, R_3 = H; R_1, R_4, R_5 = Ac
PNAG20 (10100): R_2, R_4, R_5 = H; R_1, R_3 = Ac
PNAG21 (10101): R_2, R_4 = H; R_1, R_3, R_5 = Ac
PNAG22 (10110): R_2, R_5 = H; R_1, R_3, R_4 = Ac
PNAG23 (10111): R_2 = H; R_1, R_3, R_4, R_5 = Ac
PNAG24 (11000): R_3, R_4, R_5 = H; R_1, R_2 = Ac
PNAG25 (11001): R_3, R_4 = H; R_1, R_2, R_5 = Ac
PNAG26 (11010): R_3, R_4 = H; R_1, R_2, R_4 = Ac
PNAG27 (11011): R_3 = H; R_1, R_2, R_4, R_5 = Ac
PNAG28 (11100): R_4, R_5 = H; R_1, R_2, R_3 = Ac
PNAG29 (11101): R_4 = H; R_2, R_1, R_3, R_5 = Ac
PNAG30 (11110): R_5 = H; R_2, R_1, R_3, R_4 = Ac
PNAG31 (11111): R_1, R_2, R_3, R_4, R_5 = Ac

Figure 3.1 Structures of the comprehensive library of PNAG pentasaccharides. The five-digit
number in the bracket for each compound codes for free amine (0) or *N*-acetamide (1) at residues
ABCDE from the non-reducing end to the reducing end of the pentasaccharide respectively. The
five-digit number was then viewed as a binary number and converted to the decimal system as the
compound number. For example, 01010 in binary number is equivalent to 10 in the decimal system.
Thus, the PNAG pentasaccharide bearing *N*-acetylation at units B and D only is named as PNAG10.

3.2.2 Superiority of the mQβ-conjugate in inducing anti-PNAG antibodies compared to the corresponding tetanus toxoid conjugate

As carbohydrate antigens in general are T cell independent B cell antigens[15] and small oligosaccharides alone are not immunogenic,[16] these types of antigens need to be conjugated to an immunogenic carrier in order to induce anti-carbohydrate IgG antibody responses. The mutant bacteriophage Qβ[17] is a powerful carrier and likely highly useful for carbohydrate based conjugate vaccines.[18-20] As PNAG oligosaccharides can potentially contain multiple free amine moieties, we resorted to sulfhydryl chemistry for PNAG/mQβ conjugation. The mQβ A38K/A40C/D102C was expressed in *E. coli*, purified, and incubated with the bifunctional linker succinimidyl 3-(bromoacetamido)propionate (SBAP) to react with free amines on the mQβ surface (Figure 4A). Upon removal of the excess linker, the SBAP functionalized mQβ was added to the PNAG-pentasaccharide followed by quenching the unreacted bromoacetamide moieties on mQβ with cysteine to avoid any potential side reactions of residual bromoacetamide on mQβ upon storage or following vaccination. matrix-assisted laser desorption/ionization time-of-flight (MALDI-TOF) mass spectrometry (MS) analysis of the mQβ-PNAG conjugate showed an average loading of 250 copies of pentasaccharide per particle (**Figure 3.2**). It is known that the antigen loading density on Qβ can significantly impact the levels of antibodies induced against the target antigen.[20, 21] When the loading level of antigen was low (< 50 copies per particle), despite the same total amount of antigen administered, the antibody responses induced were low.[20, 21] Increasing the local density of the antigen on the particle (over 100 antigens per particle) can significantly improve the

antibody responses, which is presumably due to the more effective cross-linking of the B cell receptors on B cells.[22] The loading density of PNAG on the mQβ-PNAG conjugate was higher than the threshold antigen level needed for powerful B cell activation.
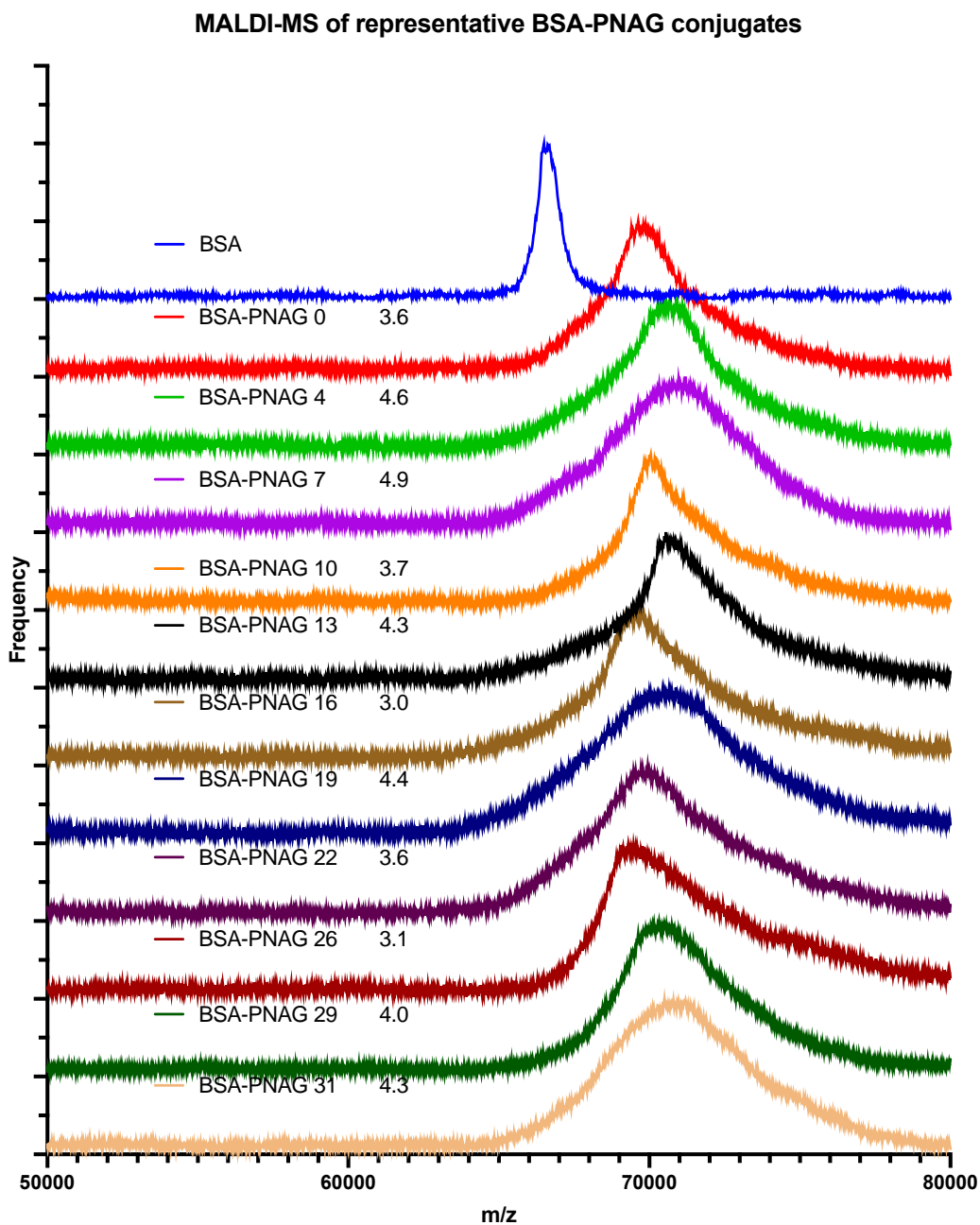

MALDI-MS of representative BSA-PNAG conjugates

BSA
BSA-PNAG 0   3.6
BSA-PNAG 4   4.6
BSA-PNAG 7   4.9
BSA-PNAG 10   3.7
BSA-PNAG 13   4.3
BSA-PNAG 16   3.0
BSA-PNAG 19   4.4
BSA-PNAG 22   3.6
BSA-PNAG 26   3.1
BSA-PNAG 29   4.0
BSA-PNAG 31   4.3

Figure 3.2 MALDI-TOF mass spectra of representative BSA-PNAG conjugates. Average loadings of glycans per BSA are presented.

With the mQβ-PNAG conjugates in hand, their abilities to induce anti-PNAG antibodies were evaluated. The conjugate of TT with the PNAG pentasaccharide bearing five free amines (5GlcNH2-TT) has undergone a phase 1 human clinical trial.[32] To compare with our mQβ-PNAG conjugate, we covalently linked PNAG0 (5GlcNH2) with the TT heavy chain (TTHc) using SBAP and achieved an average loading of 4.7 PNAG0 per protein molecule (**Figure 3.3b and Figure 3.4**). The recombinant TTHc is a suitable surrogate of TT.[33] As the molecular weight of mQβ particle (2,540 kDa for the protein shell) is about 49 times that of the TTHc (MW ~ 52 kDa), the overall densities of PNAG0 on mQβ-PNAG0 and TTHc-PNAG0 were similar.
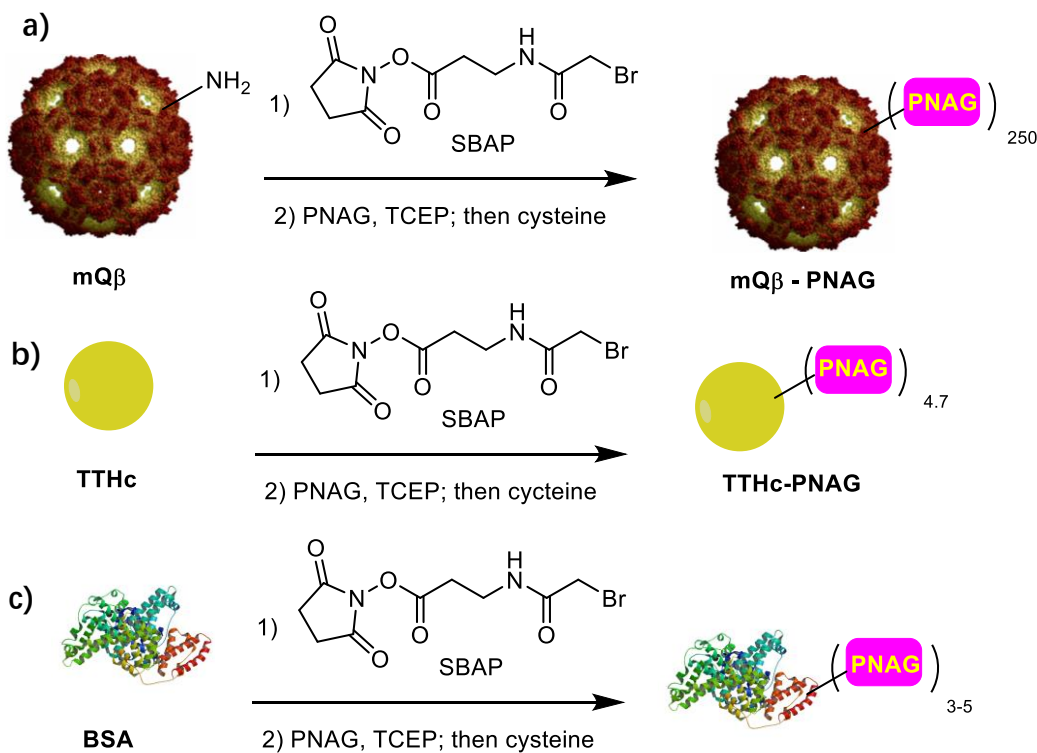

Figure 3.3 Syntheses of **a)** mQβ-, **b)** TTHc-, and **c)** BSA-PNAG conjugates. Abbreviations: succinimidyl 3-(bromoacetamido)propionate (SBAP), tris(2-carboxyethyl)phosphine (TCEP), tetanus toxoid heavy chain (TThc).

Head-to-head comparative immunogenicity studies of the mQβ- and the TTHc-PNAG0 conjugates were carried out. Groups of female C57Bl6 mice (n =5 per group) were immunized with freshly prepared mQβ-PNAG0 (8 nmol corresponding to 8 μg of PNAG0 per injection) or the TTHc-PNAG0 conjugate (8 nmol PNAG0 per injection) on days 0, 14 and 28. MPLA(20 μg) was added to each vaccination as the adjuvant. A control group of mice received a mixture of mQβ with PNAG0 at equivalent total amounts of mQβ, PNAG0, and MPLA following the same immunization protocol. On day 35, sera were collected from all mice.

To analyze the levels of antibodies generated, ELISA analyses were performed. To avoid the interference of anti-mQβ antibodies in the sera, the 32 PNAG pentasaccharides were conjugated with BSA individually (**Figure 3.2** and **Figure 3.3c**) and used as the ELISA coating antigens. As shown in **Figure 3.5a**, mQβ-PNAG0 induced high anti-PNAG IgG titers (EC50 IgG titers GMT 75,613, measured against BSA-PNAG0) while the IgM titers were negligible (GMT < 1,000). Furthermore, high levels of anti-PNAG0 IgG responses were observed more than one year after the initial immunization (**Figure 3.5b**). The IgG levels could be boosted back to near peak levels after nearly two years indicating that the mQβ conjugate induced PNAG0 specific memory B cells through immunization. The GMT of 75,613 achieved in mice receiving the mQβ-PNAG0 was significantly (P< 0.0001, Dunnett's multiple comparisons test) higher than the anti-PNAG0 IgG titers achieved in mice immunized with the corresponding TTHc-PNAG0 conjugate (GMT 4,765), highlighting the superior immunogenicity of the mQβ carrier for conjugate vaccines. Mice

immunized with the admixture of mQβ and PNAG0 did not produce any detectable levels of anti-PNAG0 IgG (GMT < 1,000), accentuating the critical need to covalently conjugate mQβ with PNAG0.

As C57Bl6 mice are inbred, to enhance the rigor of our study, we immunized outbred CD1 mice with the mQβ-PNAG0 conjugate following the same immunization protocol. mQβ-PNAG0 was able to elicit comparably high titers of anti-PNAG0 IgG antibodies on day 35 after the primary series of immunization in CD1 mice (**Figure 3.6**).
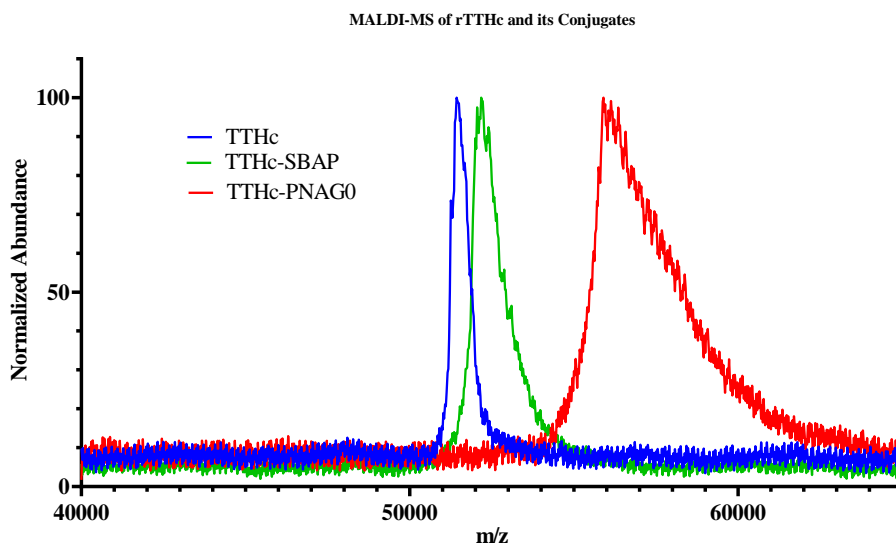

MALDI-MS of rTTHc and its Conjugates

Figure 3.4 MALDI-TOF MS characterization of TTHc conjugates. TTHc-SBAP: SBAP functionalized TTHc. The average glycan loading on the PNAG0 conjugates was calculated to be 4.7 glycans per TTHc molecule.
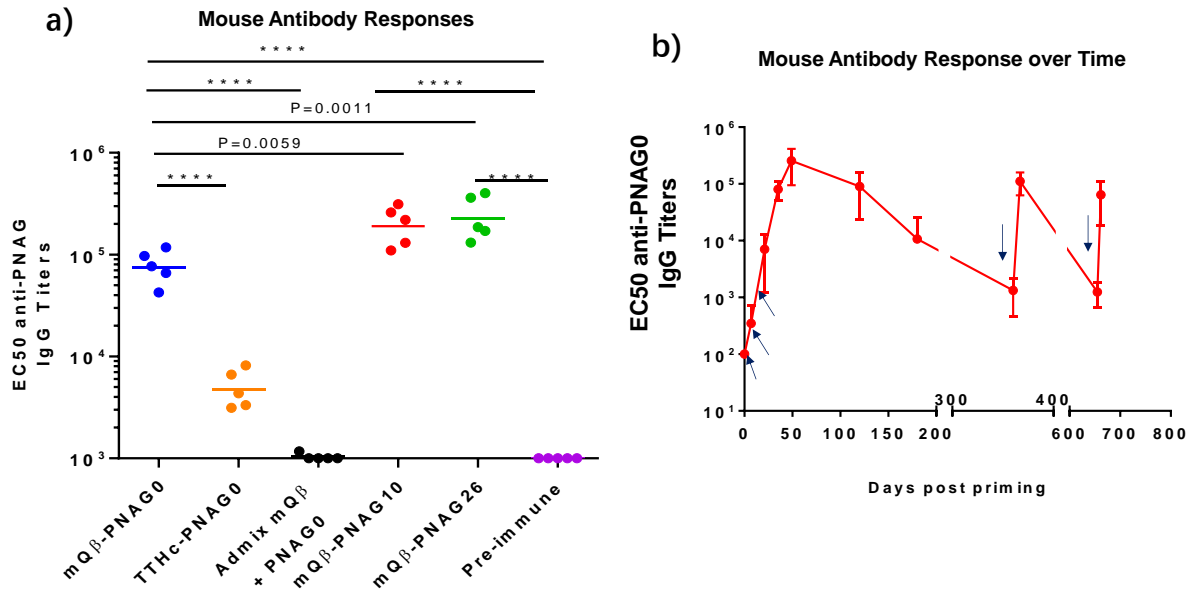
Figure 3.5 Immunization of mice with mQβ-PNAG led to high levels and long lasting anti-PNAG IgG antibodies. **a)** C57Bl6 mouse (n =5 per group) antibody responses at day 35 after immunization. The EC50 value (the fold of serum dilution that gives half-maximal binding) of the IgG titers to the immunizing oligosaccharide were plotted with each symbol representing one animal and the horizontal line is the geometric mean value of the titers within the group. The ELISA titers were determined using the BSA-PNAG conjugate containing the same PNAG structure as the immunizing Qβ-PNAG construct. One-way ANOVA allowed for rejection of the null hypothesis that all groups have the same mean IgG titers (P < 0.0001). Statistical significance was performed by Dunnett's multiple comparisons post-hoc test. **** P < 0.0001; **b)** Anti-PNAG0 IgG antibody responses of mice (n = 5) immunized with mQβ-PNAG0 monitored over time with mean titers plotted. Data are presented as mean values +/- standard deviation of the titer numbers from five mice. The arrows indicate days of vaccination (days 0, 14, 28, 360, and 655). The antibody responses could be boosted more than 650 days after prime vaccination.
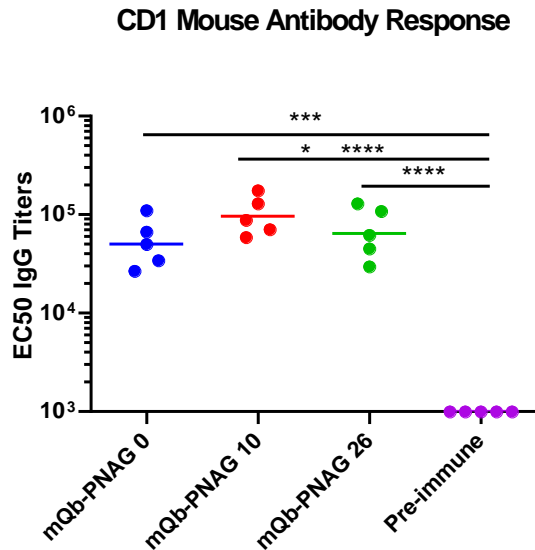
CD1 Mouse Antibody Response

Figure 3.6 Immunization of CD1 mice with mQβ-PNAG led to high levels of anti-PNAG IgG antibodies on day 35 after immunization. The EC50 values (the fold of serum dilution that gives half-maximal binding) of the IgG titers were plotted with each symbol representing one animal and the horizontal line is the geometrical mean value of the titers within the group. The ELISA titers were determined using the BSA-PNAG conjugate containing the same PNAG structure as the immunizing mQβ-PNAG construct. One-way Anova allowed for rejection of the null hypothesis that all groups have the same mean IgG titers ($p < 0.0001$). **** Statistical significance ($p < 0.0001$) by Dunnett's multiple comparisons post-hoc test.

3.2.3 Probing antigen specificity of an Anti-PNAG mAb to guide vaccine design

The precise PNAG sequences synthesized by pathogens such as *S. aureus* are not known. Furthermore, the most abundant PNAG structure on cell surfaces that would encompass a highly (80%-95%) acetylated polysaccharide is not a protective epitope.[13] To guide vaccine design, we envisioned anti-PNAG mAb F598 could provide valuable information regarding optimal acetylation patterns in a PNAG pentasaccharide. Isolated from a patient who recovered from an *S. aureus* infection, mAb F598 can protect mice against *S. aureus* infections.[34] The 32 PNAG pentasaccharide-BSA conjugates were immobilized onto a glycan microarray.[35] Following

incubation of mAb F598 with the microarray and washing, the amount of antibody remaining bound was quantified with a fluorescent secondary antibody. Interestingly, although mAb F598 was initially identified due to binding to de-acetylated PNAG with only ~ 15% N-acetylation,[34] it had little binding to glycan PNAG0 or any glycans containing only one Ac moiety. Highly acetylated PNAG such as PNAG30 and PNAG31 with four or more consecutive GlcNAcs were among the strongest binders (**Figure 3.7**). Both the location and the number of NHAc are important for F598 binding, supporting the idea of an amine/acetylation code. For example, despite having the same total number of NHAcs (4 in the molecules), PNAG23(10111) is a weak binder with the apparent affinity less than 5% of that with PNAG30(11110). Out of the PNAGs with two or three GlcNAc residues, PNAG10 and PNAG26 were the strongest binders respectively.

To better interpret the binding data, we quantified the GlcNAc binding preference of F598 by computing the preference index P for each unit of the pentasaccharide as

$$(1)\ P_i = \frac{\sum_j R_j A_i}{\sum_j R_j}$$

where i (A-E) is the site of monosaccharide from the non-reducing end to the reducing end, j (0-31) is the serial number of glycan, R is the intensity of the binding signal (Relative fluorescence unit, RLU), and A is the code for amine vs acetylation (A=-1 for free amine and A=1 for NHAc). P value indicates the conditional probability difference between finding an NHAc or free amine for binding, which ranges from -1 to 1 with -1 and 1 indicating complete preference for free amine or NHAc respectively at the specific site. As shown in **Figure 3.7b**, unit B position showed the

highest P value of 0.91, suggesting on average that there is a 95.5% chance to find an NHAc moiety

rather than a free amine on saccharide B for ligand binding with F598. The P values for sites A, C

and E were between 0.31-0.54 indictive of a moderate global preference for N-acetylation. There

were almost no preferences for NHAc or free amine for site 5 as the P value at this site was close
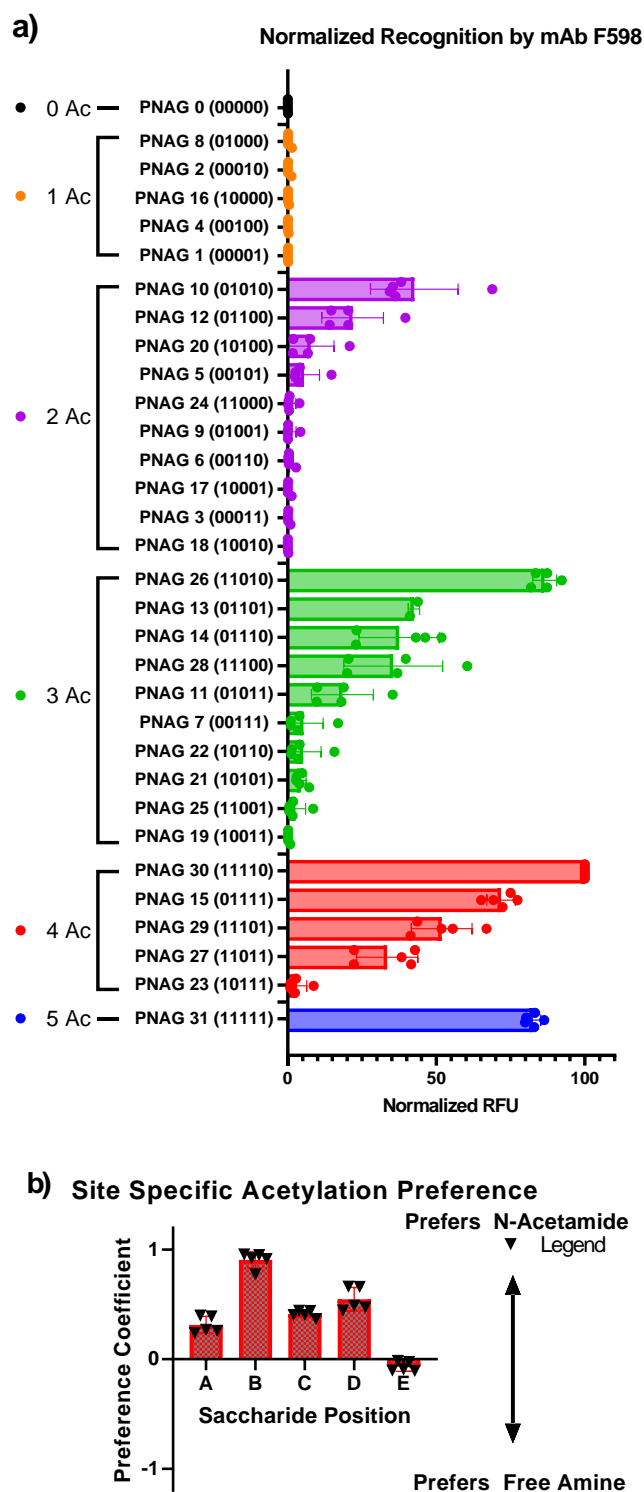
to 0.

Figure 3.7 Determination of the epitope profile of F598 mAb with the glycan microarray. **a)** Relative fluorescence unit (RFU) of F598 mAb binding with the library of 32 PNAG pentasaccharides. The glycans are grouped according to the number of NHAc units in the molecule.

Figure 3.7 (cont'd)

Each PNAG sequence is printed five times on the glycan microarray. The error bars represent the standard deviations of five individual spots. Data are presented as mean values +/- standard deviation. F598 generally prefers highly acetylated PNAG sequences. Both the location and the number of NHAc units are important determinants of F598 binding. **b)** Quantification of the preference of F598 for acetylation at each site of the PNAG pentasaccharide. The mean values are calculated from the values of the binding intensities of all 32 PNAG sequences to F598. Each PNAG sequence is printed five times on the glycan microarray. Data are presented as mean values +/- standard deviation. Data was collected by our collaborators in Dr. Jeffrey C. Gildersleeve's lab in the National Cancer Institute.

The importance of an NHAc at unit B identified from microarray binding can be rationalized by the crystal structure of F598 complexed with fully acetylated PNAG oligosaccharides (PDB 6be4).[36] The binding pocket of F598 could accommodate PNAG with five GlcNAc residues. The NHAc groups on saccharides B and D in the binding pocket deeply inserted into the groove clamped by the heavy and the light chain of the mAb, forming multiple hydrogen bonds, while the NHAcs on units A, C and E only had weak to moderate interactions with the antibody. The carbonyl oxygen of the NHAc on saccharide B forms a hydrogen bonding with light chain A32 backbone amide while bridging with light chain R52 residue via a water molecule. The carbonyl oxygen of NHAc on saccharide D also formed hydrogen bonds with light chain A97 backbone amide and the hydroxyl of heavy chain Y50. Those interactions supported the relatively high dependence of NHAc on sites B and D for the binding of F598.

3.2.4 Critical PNAG sequence for high immunogenicity of mQβ-PNAG

Based on the microarray results and the report that antibodies raised against the fully acetylated PNAG antigen were poorly protective,[13-15] we selected PNAG10 and PNAG26 as new PNAG

oligosaccharide antigens for further evaluations. PNAG10 has the strongest binding to F598 among all PNAG structures with 2 or fewer NHAcs, and PNAG26 is the best binder among all structures with 3 or fewer NHAcs. Both PNAG10 and PNAG26 have NHAcs on glycan sites B and D. PNAG0 was utilized as a positive control since the corresponding TT-PNAG0 construct (5GlcNH2-TT) has entered clinical trials [ClinicalTrials.gov Identifier: NCT02853617].

C57/Bl6 mice were immunized with the mQβ conjugates of PNAG10 or PNAG26 following the aforementioned immunization protocol (8 nmol PNAG, three injections on days 0, 14 and 28 with MPLA adjuvant). ELISA analysis of the immune sera showed significantly enhanced IgG antibody titers against the immunizing antigen (PNAG10 or PNAG 26) with GMT's of 191,141 and 227,064 ELISA units respectively as compared to pre-immune sera (**Figure 3.5**). Similarly, mQβ-PNAG10 or PNAG 26 conjugates induced high levels of anti-PNAG10 and anti-PNAG26 IgG antibodies respectively in CD1 mice (**Figure 3.6**).

To demonstrate the immunogenicity of the mQβ conjugates in an additional mammalian species, New Zealand white rabbits were immunized with mQβ conjugates of PNAG0, PNAG10, and PNAG26 (8 nmol PNAG per injection) following a similar prime-boost protocol as that used in the mouse study. ELISA analysis of the post-immune sera showed that all 3 constructs induced strong anti-PNAG IgG responses with EC50 titers over 100,000 ELISA units (**Figure 3.8a**), while those for the pre-immune sera were below 1,000 ELISA units. No side effects due to vaccinations were observed in either rabbits or mice.

We analyzed next the recognition of native PNAG using PNAG polysaccharide isolated from *Acinetobacter baumannii*[23, 24] as the coating antigen for ELISA. As shown in **Figure 3.8b**, control sera from rabbits immunized only with the Qβ carrier did not bind with PNAG. In contrast, sera from rabbits immunized with mQβ-PNAG0, -PNAG10, and -PNAG26 exhibited strong binding with mQβ-PNAG26 antiserum having the highest titer (1,584,983 ELISA units) to the native microbial polysaccharide. As a comparison, sera from the conjugate of 5GlcNH$_2$-TT[12, 14] immunized rabbit only gave a titer of 501 ELISA units (**Figure 3.8b**). Normal human sera containing natural antibodies to PNAG had an average ELISA titer of 631 ELISA units. These results further highlight the potential of mQβ-PNAG conjugates as vaccines.

Analysis of the microarray binding by post-immune sera revealed selective PNAG epitope recognition by the post-immune sera (**Figure 3.8d**). Rabbits immunized with mQβ-PNAG0 produced serum IgG antibodies exhibiting the strongest binding with the immunizing PNAG0 antigenic structure. Other good binders include PNAG1 and PNAG8, both having a single GlcNAc in the structure. Interestingly, for PNAG4 with the sequence of GlcN-GlcN-GlcNAc-GlcN-GlcN, although it also only contains one GlcNAc, it had much lower binding with the sera (about 30% that to PNAG1). This suggests that three or more consecutive GlcNs are important for binding by anti-PNAG0 sera.

mQβ-PNAG10 immunized rabbits produced serum antibodies that preferentially bind to PNAG8(01000) and PNAG10(01010), which differ only by the GlcNAc in residue D indicating

112

the non-reducing end GlcN-GlcNAc-GlcN may be the main epitope. Serum antibodies from mQβ-PNAG26(11010) immunized rabbits preferentially bound to PNAG25(11001), PNAG26(11010), PNAG8(01000), and PNAG16(10000) suggesting GlcNAc-GlcNAc-GlcN and GlcNAc-GlcN-GlcN may be part of the epitopes being recognized.
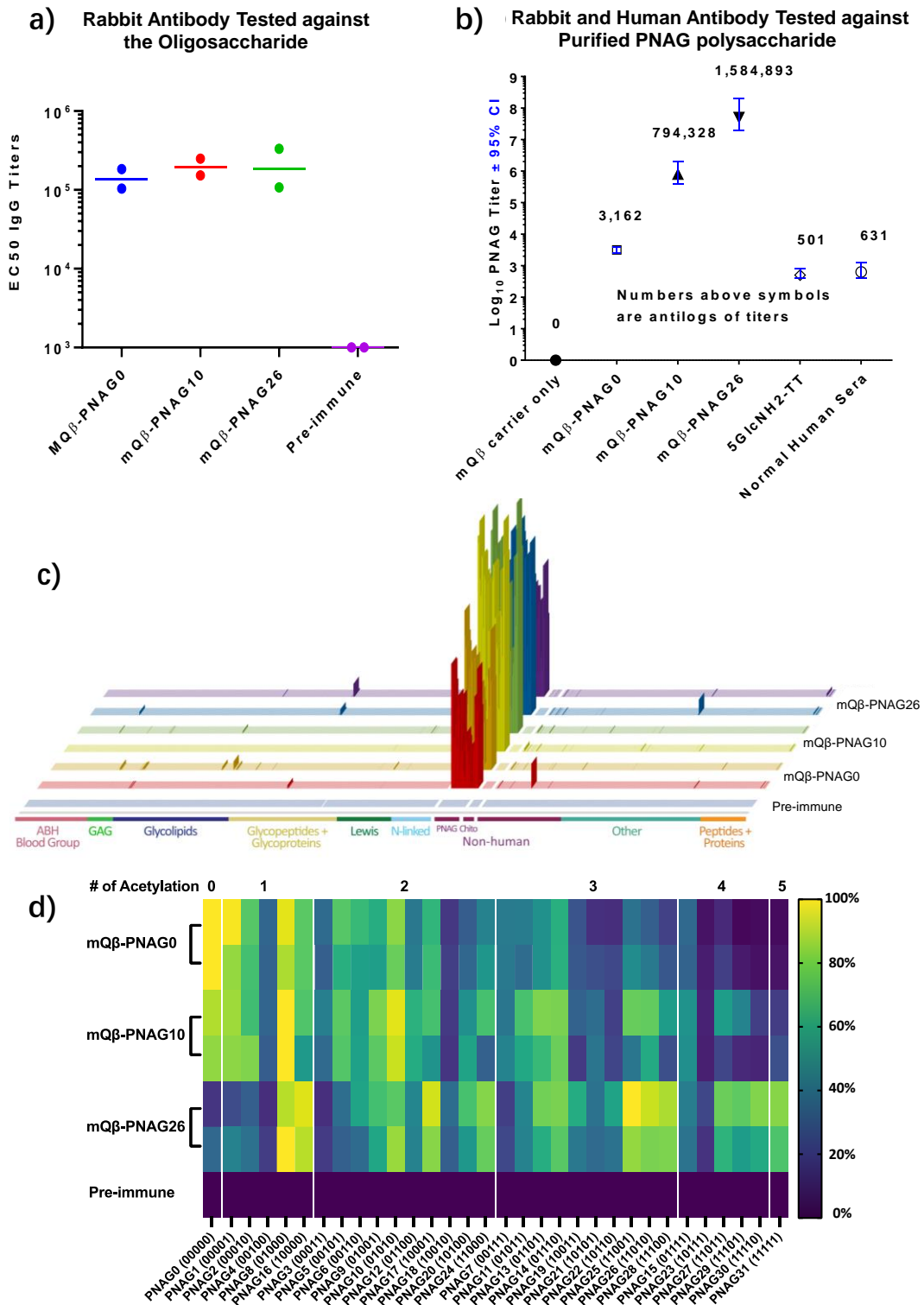
Figure 3.8 Immunization of rabbits with mQβ-PNAG conjugate induced significant anti-PNAG IgG antibodies. **a)** IgG antibody titers to the immunizing PNAG oligosaccharide in rabbit (n=2 per group) sera on day 35 after prime vaccination. **b)** IgG antibody titers in pooled rabbit sera from

Figure 3.8 (cont'd)

mQβ-conjugate or 5GlcNH2-TT conjugate immunized animals (n=2 per group) as well as titer of natural human IgG in pooled human serum against native PNAG polysaccharide purified from Acinetobacter baumannii. The numbers above symbols are the average titer numbers. Titers and 95% confidence intervals (C.I.) were determined by linear regression using log10 values of the average of replicate serum dilutions to determine the X intercept and 95% C.I. when Y=0.5 (OD405 nm of ELISA plate reading). **c)** Stacked bar graphs depicting the IgG signals at the serum dilution of 1:50,000 for each rabbit (n = 2) immunized with mQβ-PNAG0, mQβ-PNAG10 and mQβ-PNAG26 as well as pre-immune sera respectively on the array. The complete microarray results are shown in Supplementary Data; **d)** Normalized binding of the comprehensive library of PNAG pentasaccharides by IgG antibodies from post-immune sera of rabbits immunized with mQβ-PNAG0, mQβ-PNAG10 and mQβ-PNAG26, respectively, as well as pre-immune sera. PNAG sequences are grouped together according to the total number of acetamides in the molecules. The color scale bar is shown on the right with 100% indicating the strongest binding to a PNAG component and 0% indicating the weakest binder. For each antigen, the two rows represent sera from two rabbits per group immunized with the specific construct. **b)** Data was collected by our collaborators in Dr. Gerald B. Pier's lab in the Harvard Medical School. **c) d)** Data was collected by our collaborators in Dr. Jeffrey C. Gildersleeve's lab in the National Cancer Institute.

3.2.5 Antisera mediated bacterial recognition and killing

For an effective vaccine, it is important to establish that the post-immune sera bind not only the isolated antigen, but also the antigen expressed on pathogen cells. We reacted *S. aureus* ATCC 29213 cells with rabbit immune sera and the bound antibodies were detected by a fluorescently labeled anti-rabbit IgG secondary antibody. As shown in **Figure 3.9a**, fluorescence microscopy images showed stronger binding to bacterial cells by IgG antibodies in mQβ-PNAG10 and mQβ-PNAG26 immune sera compared to sera from mQβ-PNAG0 immunized rabbits or pre-immune sera. To validate pathogen recognition observed in fluorescence images, whole cell ELISA was performed. *S. aureus* cells were coated on ELISA plates, incubated with rabbit immune sera, and

detected by secondary antibodies. The post-immune sera exhibited significantly higher titers in binding with the cells compared to pre-immune sera (**Figure 3.10**).

For antibody-mediated complement deposition,[25] we added various immune sera to wells coated with purified PNAG isolated from *Acinetobacter baumannii*[23, 24] along with IgG/IgM depleted 2.5% human complement (**Figure 3.11a**). After incubation, the immobilized complement component C1q was detected by anti-C1q antibodies. As shown in Figure 8A, sera from mQβ-PNAG10 and mQβ-PNAG26 deposited significantly more C1q than those from mQβ-PNAG0 immunized rabbits, which in turn had more potent C1q binding than antibodies in sera from rabbits immunized with the 5GlcNH$_2$-TT conjugate.[12, 14]

The abilities of the post-immune sera to kill bacteria *in vitro* were evaluated next *via* the opsonophagocytic killing (OPK) assay. *S. aureus* cells were treated with pooled rabbit immune sera, followed by the addition of complement/phagocytic cells and quantification of the number of bacterial cells surviving the opsonic killing. As shown in **Figure 3.11b**, while the pre-immune sera were completely ineffective, all 3 constructs induced antibodies with potent *in vitro* killing activity. mQβ-PNAG26 (EC50: 2,534) and mQβ-PNAG10 (EC50: 3,045) showed higher EC50 OPK titers as compared to mQβ-PNAG0 (EC50: 1,345). Omitting either immune sera, complement or phagocytic cells resulted in complete loss of killing activity (**Figure 3.12**), indicating the need for all three components for protective immunity.
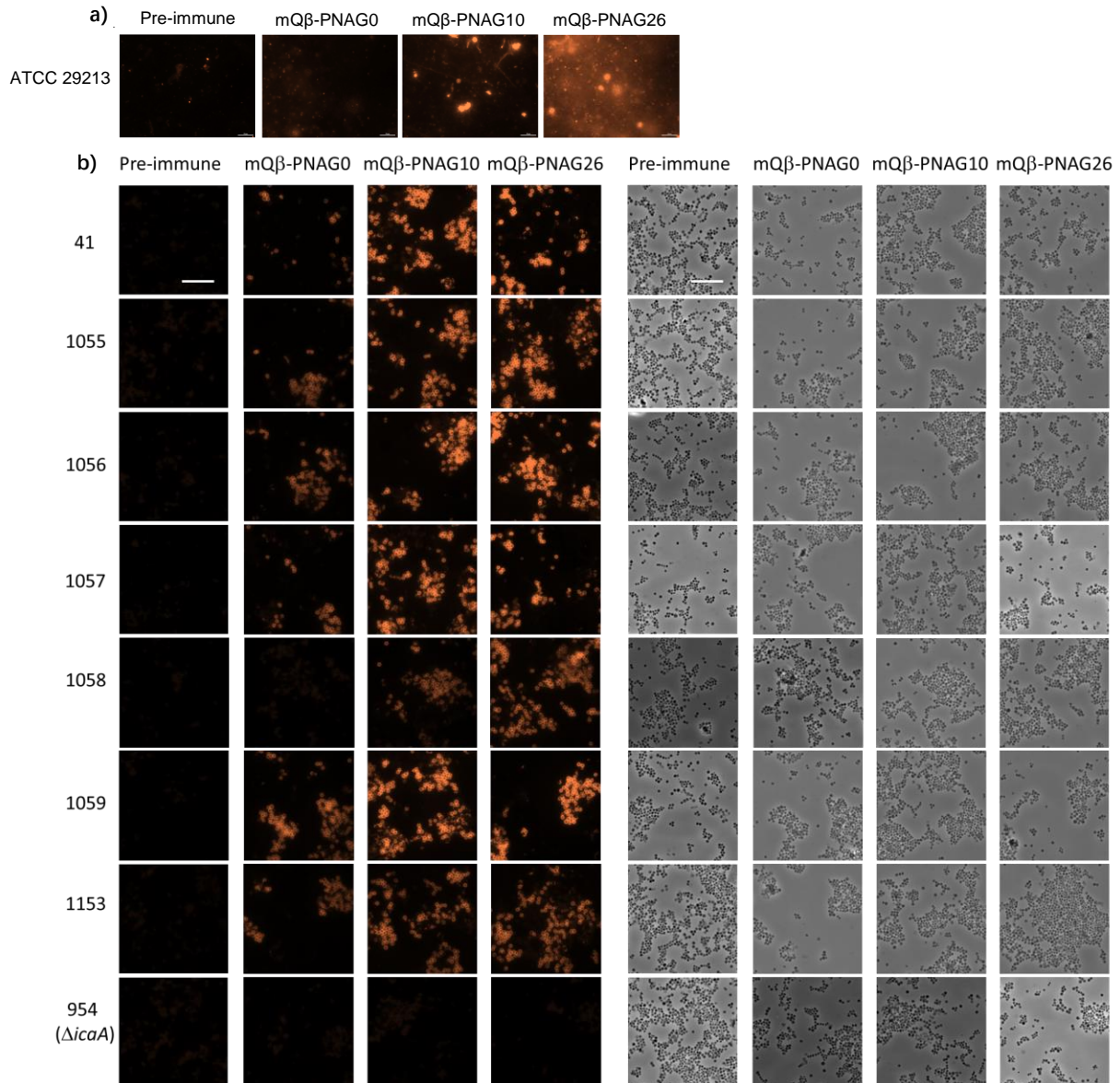
116

Figure 3.9 a) *S. aureus* ATCC 29213 cells were stained by pre-immune, and post-immune sera from rabbits immunized with mQβ-PNAG0, mQβ-PNAG10, and mQβ-PNAG26 respectively followed by the addition of Alexa Fluor 594 labeled goat anti rabbit IgG Fc 2nd antibody. The binding was visualized through fluorescence microscopy. Sera from rabbits immunized with mQβ-PNAG10, and mQβ-PNAG26 showed significant binding to the bacteria. The scale bar is 10 μm. **b)** Fluorescence images and bright field images of MRSA strains, i.e., 41, 1055, 1056, 1057, 1058, 1059, and 1153 upon staining with immune sera from rabbits immunized with mQβ-PNAG0, mQβ-PNAG10, and mQβ-PNAG26 respectively. The post-immune sera bound with these strains well as detected by the Alexa Fluor 594 labeled goat anti-rabbit IgG Fc 2nd antibody. In comparison, a control strain lacking PNAG expression with *icaA* gene knock out (954) showed negligible binding by the sera, suggesting the recognition is PNAG dependent. Scale bar: 10 μm.
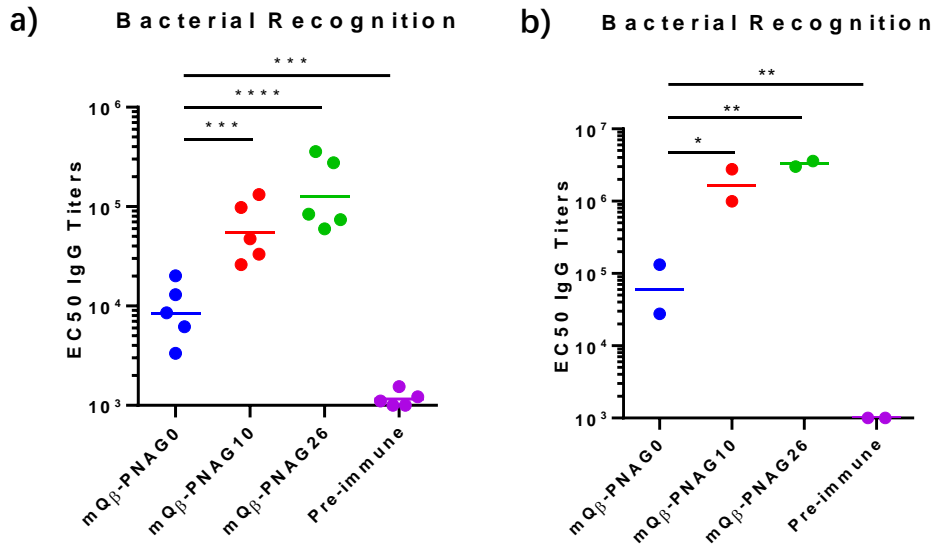
Figure 3.10 Post-immune sera of **a)** mice and **b)** rabbits immunized with the mQβ-PNAG conjugates recognized the *S. aureus* cells well as determined by ELISA. The EC50 values (the fold of serum dilution that gives half-maximal binding) of the IgG titers were plotted with each symbol representing one animal and the horizontal line is the geometrical mean value of the titers within the group. The ELISA titers were determined against *S. aureus* cell coated ELISA wells. Statistical analysis was performed using one way ANOVA. $* p < 0.05$; $** p < 0.01$; $*** p < 0.001$; $**** p < 0.0001$.
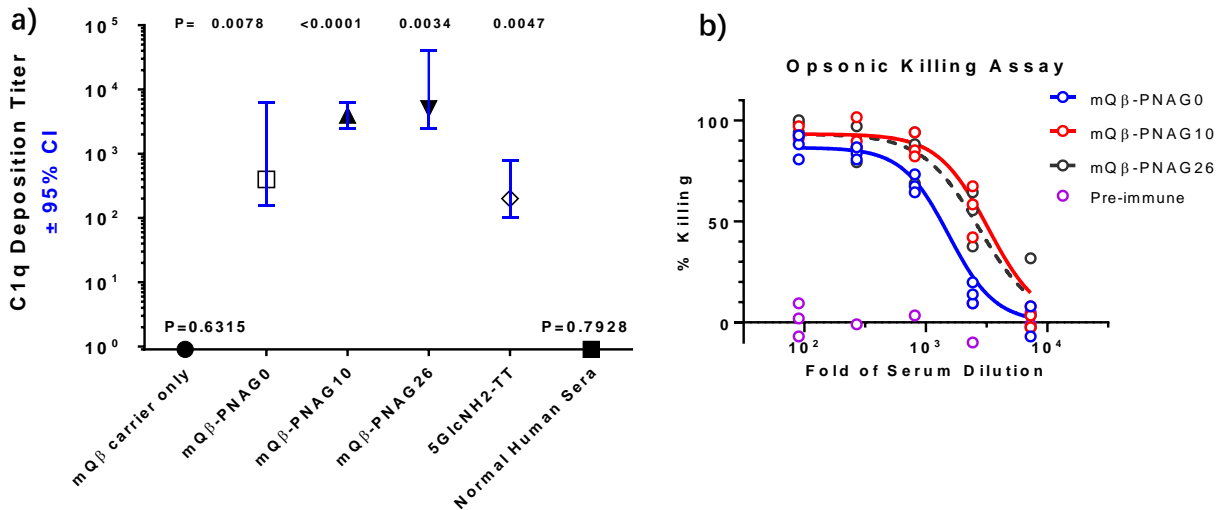

Figure 3.11 Deposition of C1q onto purified PNAG polysaccharide and analysis of opsonic killing activities. **a)** Complement deposition tests were performed as described [25] using pooled sera from rabbits (n=2 per group) immunized with mQβ-PNAG conjugates, the 5GlcNH$_2$-TT conjugate or from a sample of pooled normal human sera. Titers and 95% confidence intervals (C.I.) were

determined by linear regression using $\log_{10}$ values of the average of replicate serum dilutions to determine the X intercept and 95% C.I. when Y=0.5 (OD_{405} nm of ELISA plate reading). P values indicate the significance of the deviation of the slope of the titration curve from zero to identify sera with activity at P<0.05. mQβ-PNAG10 and mQβ-PNAG26 conjugates were more potent than the mQβ-PNAG0 and 5GlcNH$_2$-TT conjugate in inducing C1q deposition onto purified PNAG. Normal human serum had no significant C1q depositing activity in spite of having a binding titer to PNAG (see **Figure 3.8**) consistent with prior reports that naturally-acquired human antibody to PNAG is not functional due to the inability to activate the complement pathway [11, 26]. Titers were determined by simple linear regression. **b)** Pooled sera from rabbits (n =2 per group) immunized with mQβ-PNAG conjugate led to significantly higher levels of opsonic killing activities against *S. aureus* cells. Three aliquots were prepared from each pooled serum and the individual values of the three aliquots were presented. **a)** Data was collected by our collaborators in Dr. Gerald B. Pier's lab in the Harvard Medical School.
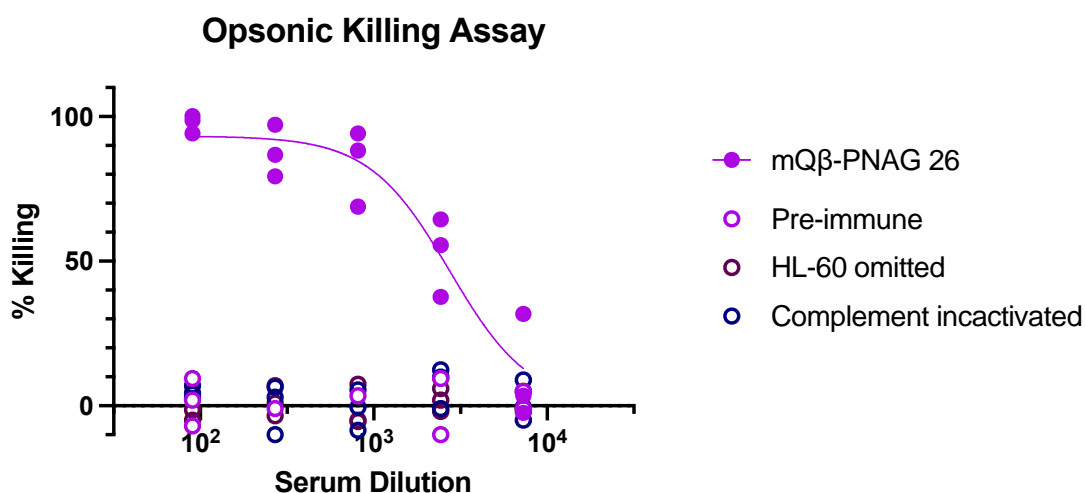
Opsonic Killing Assay

Figure 3.12 Opsonic killing is dependent on all factors including bacterial specific serum antibody, active complement source, and phagocytic cells. Here is an example showing omitting each factor completely abrogates killing activity. Complement inactivation was performed under 56 °C for 30 mins. HL-60 omitted group and complement inactivated group were carried out with mQβ-PNAG26 serum.

3.2.6 Protection against *S. aureus* induced death by immunization

The efficacy of the various vaccine constructs in protecting against bacterial infection was

tested in two mouse bacteremia challenge models. According to the CDC, bloodstream infections

by *S. aureus* are serious threats with nearly 20,000 death per year in the US [1]. For the *in vitro* study, we first compared the mQβ-PNAG0 vs TTHc-PNAG0 construct. In the active protection model, mice were immunized three times with mQβ-PNAG0 or TTHc-PNAG0 at equivalent doses (8 nmol PNAG0) (n = 20 for each group) (**Figure 3.13**). Another group of control mice received a mock injection of saline. Two weeks following the last vaccination, each mouse was challenged *via* the tail vein with 10*LD50 of the *S. aureus* strain ATCC29213. Mice that had received saline all died within 2 days of bacterial challenge. On the other hand, *95%* of the mice receiving mQβ-PNAG0 were protected against death from this pathogen. The survival rate of the mQβ vaccine group was significantly better than TTHc-PNAG0 vaccinated group ($p=0.0154$, logrank test) (**Figure 3.13a**). Bacteria were detected in the kidneys of 35% (7 out of 20) of the mice immunized with TT-PNAG0, while mQβ-PNAG0 vaccination reduced the recovered levels of *S. aureus* from the kidneys with bacteria only observed in 5% of the mice (1 out of 20) (**Figure 3.13b**). Contingency table analysis of the proportion of the 20 immunized mice in each group with or without detectable *S. aureus* by Fisher's exact test showed significantly ($p = 0.0436$) fewer infected kidneys in the mQβ-PNAG0 immunized group, with a relative risk of 0.68 (95% CI= 0.45 to 0.93). Thus, disease burden evaluated by the levels of *S. aureus* in mouse kidneys was significantly better in mQβ-PNAG0 vaccinated group compared to those receiving the TTHc-PNAG0 vaccine. These results further support the superior performance of the mQβ carrier.
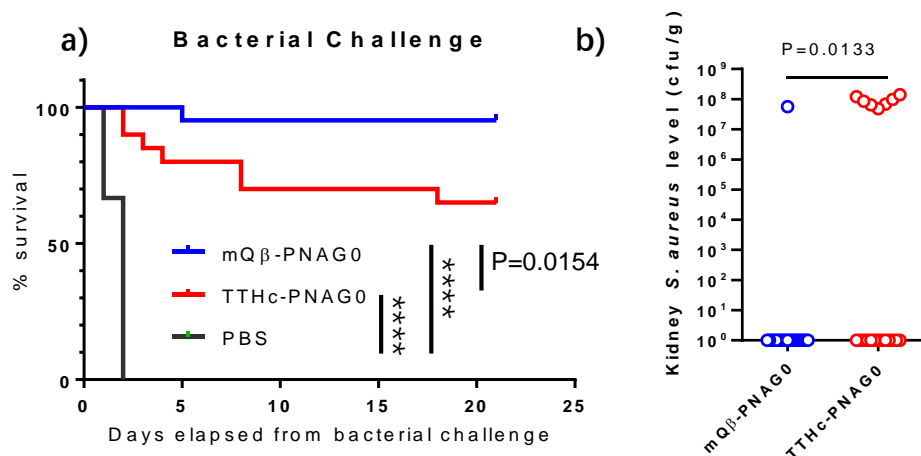
Figure 3.13 Protective effects of vaccination. Immunization with mQβ-PNAG0 effectively **a)** protected against *S. aureus* infection, and **b)** reduced bacterial count in mouse kidney. mQβ-PNAG0 was significantly better than TTHc-PNAG0 in protecting mice and reducing disease burden (n = 20 for each group). Logrank tests were performed for statistical analysis. P values were presented in the graph. **** P < 0.0001.

As the mQβ-PNAG0 immunogen gave almost complete protection in the active protection model in mice, we next established a passive protection model to differentiate the various mQβ-PNAG constructs, using rabbit sera transferred to mice. The passive model can be a more stringent test by using more dilute sera for protection. Rabbit sera were diluted 800-fold and administered intraperitoneally to mice, which were then challenged with 10*LD50 (200 million cells) of *S. aureus* ATCC29213 *via* the tail vein (**Figure 3.14**). While all control mice receiving the pre-immune sera died within 3 days of this challenge, all post-immune sera from PNAG0, PNAG10, or PNAG26 immunized rabbits bestowed significant protection.

Mice receiving sera from mQβ-PNAG26 and mQβ-PNAG10 immunized rabbits showed higher survival rates than those receiving PNAG0 sera (**Figure 3.14a**) (60% and 50% respectively

vs 30%) and lower pathogen load compared to mQβ-PNAG0 sera supporting the *in vitro* opsonic killing data (**Figure 3.14b**). We next tested the combination of two sera. Interestingly, administering the mixed PNAG26 and PNAG0 sera (1:1 ratio with each individual serum diluted 1,600 times, which is regarded equivalent in concentration to 1:800 dilution of a single serum) provided 100% protection to mice against the 10*LD50 challenges with *S. aureus* (**Figure 3.14a**). The kidneys of mice receiving the combination of PNAG26 and PNAG0 sera had no detectable bacteria (**Figure 3.14b**). The higher protective efficacy observed with the combined sera was presumably because the PNAG polysaccharide can be heterogenous in the amine/acetylation patterns. While some of the sequences such as the fully deacetylated PNAG0 may be rare within the native PNAG polysaccharide, antibodies generated by mQβ-PNAG0 can complement those by mQβ-PNAG26. Thus, the combination of two mQβ-PNAG constructs can broaden bacterial recognition and enhance protection against bacterial challenges.
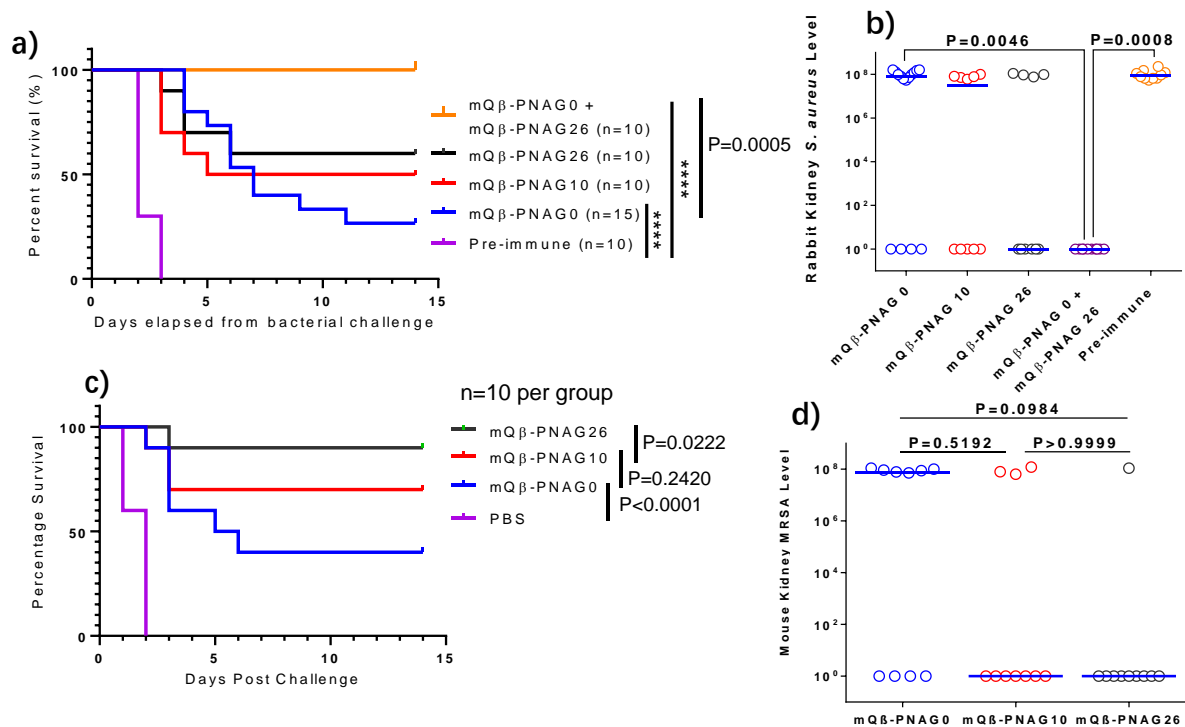
Figure 3.14 Protective effects of antisera from immunized rabbits. Transfer of antisera from mQβ-PNAG immunized rabbits to mice **a)** provided significant protection to mice (n = 10 per group) against the lethal challenges by *S. aureus* ATCC 29213. Statistical analysis was performed with the logrank test. **** P < 0.0001; and **b)** significantly reduced bacterial count in mouse kidney. The combination of sera from mQβ-PNAG0 and mQβ-PNAG26 immunized rabbits provided complete protection to mice. Statistical analysis for survival was performed using the logrank test. Analysis of *S. aureus* colony forming units (cfu)/gm was by Kruskal-Wallis nonparametric ANOVA (P<0.0001 for overall effect of serum given). P values for pairwise comparisons shown on graph by Dunn's multiple comparisons test. Transfer of antisera from mQβ-PNAG immunized rabbits to mice **c)** provided significant protection to mice against the lethal challenges by MRSA strain 1058 (n = 10 per group); Statistical analysis for survival was performed using the logrank test; and D) reduced bacterial count in mouse kidneys. Sera from mQβ-PNAG26 immunized rabbits provided the highest protection to mice. The horizontal line represents the median value of each group. Statistical analysis for survival was performed using the logrank test. Analysis of MRSA cfu/gm was by Kruskal-Wallis non-parametric ANOVA (P=0.0967). P values for pairwise comparisons shown on graph by Dunn's multiple comparisons test**.**

3.2.7 mQβ-PNAG vaccines are effective against MRSA challenges

The emergence of MRSA is a pressing public health concern.[27] Effective vaccines can provide a complementary tool to combat *S. aureus* infections and reduce the reliance on antibiotics. The post-immune rabbit sera were tested against multiple MRSA strains including six clinical strains first *via* immunofluorescent staining (**Figure 3.9** and **Table 3.1**). All three mQβ-PNAG sera recognized the seven strains tested highlighting the breadth of immune recognition. A control strain lacking PNAG expression with *icaA* gene knock out (954) showed negligible binding by the immune sera, indicating the recognition is PNAG dependent. Next, rabbit sera were diluted 800 times and administered to mice, which were then challenged with 10*LD50 (200 million cells) of the MRSA strain 1058 *via* the tail vein (**Figure 3.14c**). Sera from mQβ-PNAG26 immunized rabbits protected 90% of the mice from MRSA induced death, which was significantly higher than the 40% protection by mQβ-PNAG0 sera. Correspondingly, mice receiving mQβ-PNAG26 rabbit sera had the lowest overall bacterial load in the kidneys of challenged mice (**Figure 3.14d**).

Strain	Description	Reference
41	JE2; Laboratory derived wild type parental MRSA; USA300_LAC; CC8	28
954	icaA::Tn; NTML NE37 *bursa aurealis* transposon (Tn) mutant, Erm^R	28
Clinical isolates		
1055	MRSA abscess hand cellulitis	29
1056	MRSA abscess left arm	29
1057	MRSA left wrist/ index finger	29
1058	MSSA abscess left foot osteomyelitis	this study
1059	MSSA bone from the coccyx, chronic osteomyelitis	29
1153	MRSA hallux bone	this study

Table 3.1 Staphylococcus strains used in this study.

3.2.8 Immunization does not significantly alter gut microbiome

As PNAG is expressed on many types of bacteria, we explored the effects of immunization on gut microbiome. To analyze the composition of the gut microbiome, mice were fully immunized with mQβ-PNAG26, and feces were collected on day 0 prior to immunization and day 35 following the initial prime immunization. The microbial species present in the droppings were analyzed *via* the 16S rRNA sequencing. Despite the significant amounts of anti-PNAG IgG produced in mouse sera, there were no significant changes in the microbial community present in the mouse gut (**Figure 3.15**). Similar results were reported in a sponsored trial of the 5GlcNH$_2$-TT vaccine and shown in the study of anti-PNAG therapy in the setting of graft-versus-host disease,[30] or in human subjects in phase 1 clinical trials of both the 5GlcNH$_2$-TT vaccine or anti-PNAG mAb.[31, 32] These

observations corroborate that immunity to PNAG does not significantly alter the gut microbiome

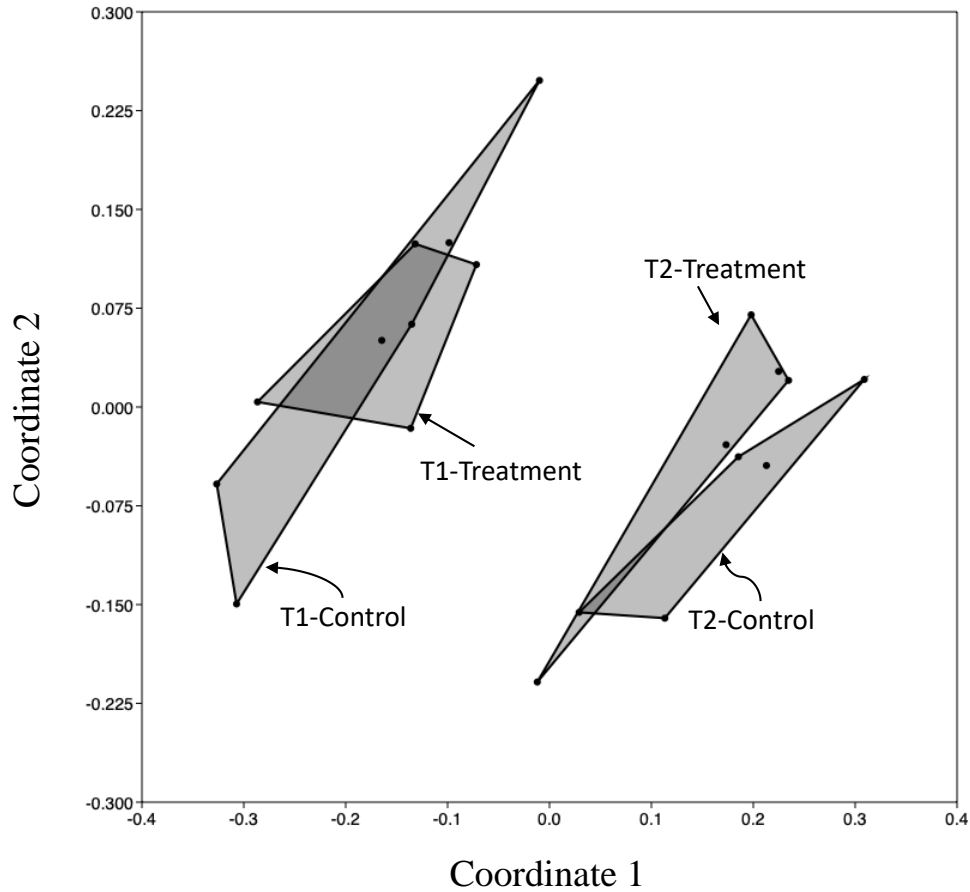in immunized animals highlighting the potential safety of the vaccine.

Figure 3.15 Non-Metric Multidimensional Scaling (NMDS) analysis of bacterial communities of controls and treatments showing no significant changes in the gut microbial community following mQβ-PNAG26 immunization. T1 and T2 refer to the two sampling times. T1 = first sampling right before immunization, T2 = control and treatment samples at 42 days after the prime immunization. Each of the four groups is delineated by a convex hull describing a minimum area. The stress test values for 2D and 3D NMDS were 0.141 and 0.109, respectively. Amplicon sequence variants (ASV) datasets revealed similar patterns of ordination. When comparing treatment versus control within a timepoint, ANalysis Of SIMilarity (ANOSIM) and Permutational multivariate analysis of variance (PERMANOVA) values of -0.04 (T1) and 1.518 (T2) indicated high similarity in the phylogenetic structure of the bacterial communities. Data was analyzed by our collaborators in Dr. Terence Marsh's lab from the Department of Microbiology and Molecular Genetics.

3.3 Conclusion

In summary, numerous pathogens produce PNAG, rendering it a highly attractive target for vaccine development with the conjugate of fully deacetylated PNAG pentasaccharide with TT carrier currently undergoing human clinical trials as an anti-microbial vaccine. In order to enhance the potential protective efficacy, several aspects of the PNAG based vaccine can be improved. As carbohydrates are typically T cell independent B cell antigens, an immunogenic carrier is critical. We have demonstrated that mQβ is a powerful carrier. The mQβ-PNAG conjugate was found to be superior in inducing higher levels of anti-PNAG IgG antibodies as compared to the corresponding PNAG conjugate with the TTHc carrier.

Besides the carrier, another important factor in vaccine design is the identification of the protective epitope(s) of the PNAG antigen, which was hampered by the lack of diverse structurally well-defined PNAG compounds. To gain a deeper understanding of the epitope specificity, a comprehensive library of PNAG pentasaccharides covering all possible combinations of free amine and NHAc has been synthesized. The synthesis is highlighted by a divergent design through the judicious choice of four amine protective groups, which can be orthogonally removed without affecting each other. The library of 32 PNAG pentasaccharides was obtained from just two strategically protected pentasaccharide intermediates, thus significantly enhancing the overall synthetic efficiency.

The availability of the comprehensive library provided an exciting opportunity to probe the epitope specificity through a glycan microarray. Screening of an anti-PNAG mAb F598 on the microarray suggests that the NHAc at unit B plays a critical role in F598 binding. NHAc at unit D could further enhance the binding. This knowledge led to the addition of two PNAG sequences (PNAG10 and PNAG26) beyond the fully deacetylated PNAG0 for vaccine studies.

The mQβ conjugates with PNAG10 and PNAG26 were found to elicit IgG antibodies capable of inducing high levels of complement deposition and opsonic killing of bacteria compared to the mQβ-PNAG0 conjugate. Vaccination with mQβ-PNAG conjugate provided effective protection to mice against lethal challenges by *S. aureus* in both active and passive immunity models. Mice were also effectively protected from MRSA-induced death by the immune sera with significantly reduced bacterial load in the kidneys. The vaccines are biocompatible with no adverse side effects and do not significantly disturb the gut microbiome of the immunized mice. PNAG based vaccine design guided by the well-defined synthetic library of PNAG is a powerful strategy to develop the next generation of vaccines and more effectively fight against pathogen infections including those by drug resistant strains.

3.4 Experimental methods

3.4.1 Synthesis of mQβ-PNAG conjugates

The mQβ particle[17] was functionalized first with the SBAP linker. To a solution of 10 mg/ml mQβ in potassium phosphate buffer (KPB) (100 mM, pH=7.0) was added 3.2 mg SBAP (15 equiv

to mQβ subunits) in 10 µl DMSO. The solution was gently mixed and nutated under RT for 1 hour.

The protein was recovered with a 15 ml Amicon filter (molecular weight cut off MWCO=100 kDa)

under 4,000 rcf and washed with KPB (100 mM, pH=8.0) for 4 times. The modified mQβ was

resuspended in KPB (100 mM, pH=8.0) to a final concentration of 10 mg/ml and used immediately.

Conjugation reactions of mQβ with PNAG0, 10 and 26 to mQβ were conducted in similar manners.

As an example, PNAG0 (5 mg) was dissolved in 1 ml of degassed KPB (100 mM, pH=8.0). Tris(2-

carboxyethyl)phosphine, immobilized on Agarose CL-4B (Sigma-Aldrich # 52486, 2 equiv) was

added and the solution was nutated under RT for 1 hour to transform the disulfide bond in PNAG0

to free sulfhydryl groups. The resin was removed by centrifugation and the supernatant was

lyophilized. To 5 mg of the reduced oligosaccharide (15 equiv to mQβ subunits) was added 5 mg

of SBAP functionalized mQβ in 0.5 ml KPB (100 mM, pH=8.0) and the vial was gently inverted

a few times to allow the oligosaccharide to dissolve. The mixture was nutated under room

temperature for another 16 hours before 5 µl 1M cysteine was added. The mixture was nutated for

another 2 hours to quench the unconsumed bromoacetamide. The final product was recovered by

a 15 ml Amicon filter (MWCO=100 kDa) under 4,000 relative centrifugal force (rcf) and washed

with sterile PBS for 4 times. The final conjugate was analyzed by MALDI-TOF MS (**Figure 3.16**).
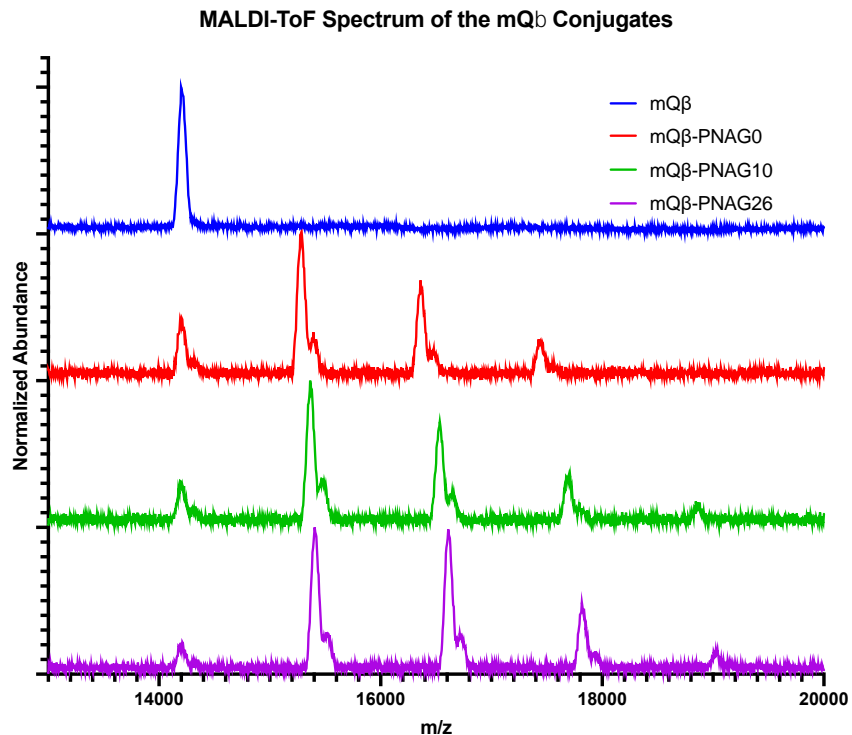
MALDI-ToF Spectrum of the mQb Conjugates

Figure 3.16 MALDI-TOF spectra of the mQβ-PNAG conjugates. The peak assignment was shown in the table below. The average glycan loading per particle was calculated by

$$L = 180 \times \frac{\sum N_i A_i}{\sum A_i}$$

where 180 is the number of subunits in each VLP, N is the number of glycan loading in a specific peak, and A is the relative abundance of the corresponding peak. The shoulder peaks showing at +113 position of the major peaks are due to +1 linker as a result of intrasubunit crosslinking. The average loading is around 250 glycans per mQβ particle based on the MS results.

3.4.2 MALDI-TOF MS protocol

mQβ-PNAG conjugates were first reduced by dithiothreitol (DTT) (100 mM) at 37°C for 30

min to break up the disulfide bonds crosslinking mQβ subunits. BSA and TTHc conjugates were

analyzed without pretreatment. Sinapinic acid (SA) was used as matrix. 0.5 mg/ml SA was

dissolved in acetonitrile : water : formic acid (50 : 50 : 0.1) mixture and 1 μl matrix solution was

added to each spot of a MALDI base plate and air dried. The protein solution (1 μl, typical concentration: 1 mg/ml) was bound to a C4 resin tip (Millipore ZTC04S008) and desalted with water. The protein was then eluted with 1 μl acetonitrile : water : formic acid (50 : 50 : 0.1) mixture directly to the MALDI base plate to avoid protein loss on hydrophobic surfaces. The mixture was air dried and analyzed with MALDI-TOF MS.

3.4.3 BSA conjugation

All BSA-PNAG conjugates were synthesized in the same manner. BSA powder (Sigma) was dissolved in potassium phosphate buffer (100 mM, pH=7.0) to a concentration of 10.0 mg/ml. To 1 ml of BSA solution, 2.0 mg (42 equiv) of the SBAP linker (Fisher) was added in 10 μl DMSO. The solution was mixed gently on a nutator at RT for 2 hours before passing through a 10 ml hand packed G25 column. The protein-containing fractions were recovered using Milli-Q water, aliquoted and lyophilized. PNAG glycan (1 mg) was dissolved in a rubber stopper sealed vial with 0.5 ml degassed KPB (100 mM, pH=8.5). 0.15 mg (1.0 equiv) of TCEP (sigma) was dissolved in 0.1 ml degassed KPB and injected into the vial with an HPLC syringe. The mixture in the vial was stirred under continuous N_2 flush for 30 mins. The solution was injected into another sealed and N_2 flushed vial containing 1 mg lyophilized modified BSA. The vial was stirred for another 2 hours. 1 μl 1M cysteine was injected into the vial and the reaction was allowed to carry on for another 1 h to quench the unconsumed bromoacetamide. The protein was recovered by a G25 column and lyophilized. The saccharide loading was quantified by MALDI-TOF MS (**Figure 3.2**).

3.4.4 Synthesis of TTHc-PNAG0

The buffer for recombinant TTHc (Fina Biosolutions) was first exchanged to KPB (100 mM, pH=7.0) via a 15 ml Amicon filter (MWCO=30 kDa) with repeated concentration and resuspension. The protein was then modified with SBAP. To 1 ml KPB solution of 5 mg/ml TTHc was added 1.5 mg SBAP (50 equiv) in 10 µl DMSO. The solution was gently mixed and nutated under RT for 1 hour. The protein was recovered with a 15 ml Amicon filter (MWCO=30 kDa) under 4,000 rcf and washed with KPB (100 mM, pH=8.0) for 4 times. The modified TTHc was resuspended in KPB (100 mM, pH=8.0) to a final concentration of 5 mg/ml and used immediately. To 4.6 mg of reduced oligosaccharide (50 equiv) was added 5 mg modified TTHc in 1 ml KPB (100 mM, pH=8.0) and the vial was inverted gently to allow the oligosaccharide to dissolve. The mixture was nutated under RT for another 16 hours before 10 µl 1M cysteine was added. The mixture was nutated for another 2 hours to quench the unconsumed bromoacetamide. The final product was recovered by a 15 ml Amicon filter (MWCO=30 kDa) under 4,000 rcf and washed with sterile PBS 4 times. The final conjugate was analyzed by MALDI-TOF MS (**Figure 3.4**).

3.4.5 Glycan Microarray

Glycan microarray slides were produced as previously described[33, 34] on SuperEpoxy 2 slides (SME2; ArrayIt Corp, Sunnyvale, CA) and stored vacuum sealed at −20°C. Prior to use, slides were warmed to RT and then scanned to identify any missing spots or defects (the print buffer contains a soluble dye). Slides were printed with 8 replicate array blocks. An 8-well slide module

(ProPlate® Multi-Well Chambers, Grace Bio-Labs) was affixed to each slide to separate the 8

blocks. Each of the 8 wells was then blocked overnight at 4°C with 400µL/well of 3% w/v BSA

(Sigma-Aldrich, A3059, Lot SLBW6770) in PBS. Next, slides were washed twice with

400µL/well of PBST followed by incubation with mouse or rabbit serum. Serum samples were

diluted into 1% BSA/PBS (1:100 for mouse sera; various dilutions for rabbit sera) and then

incubated at 37°C with gentle shaking for 2.5h. Diluted sera was removed from each well using a

multichannel pipettor, followed by three quick washes with 400µL/well of PBST and three 2 min

washes with PBST. Wells were next incubated with fluorophore labeled secondary reagents

[*mouse*: Cy3 anti-mouse IgG (Cy3 anti-mouse IgG; Jackson 115-165-071) and AlexaFluor 647

Anti-mouse IgM (Alexa Fluor® 647 AffiniPure Goat Anti-Mouse IgM, µ chain specific; Jackson

115-605-075), each diluted 1:500 in 1%BSA/PBS; *rabbit*: Cy3 anti-rabbit IgG (Cy™3 AffiniPure

Goat Anti-Rabbit IgG, Fc fragment specific; Jackson 111-165-046) and AlexaFluor 647 Anti-

rabbit IgM (Alexa Fluor® 647labeled Goat Anti-Rabbit IgM mu chain; Abcam 150095), each

diluted 1:500 in 1%BSA/PBS] for 45min at 37°C with gentle shaking. Secondary reagent solutions

were removed, followed by four quick washes with 400µL/well of PBST and one 2 min wash with

PBST. The well module was removed and the slide was submerged in PBST for 5 min as a final

wash. Slides were dried by centrifugation at $1000 \times g$ for 4 minutes and then scanned on a an

InnoScan 1100 AL fluorescence scanner (Innopsys; Chicago, IL) at 5 µm resolution. Analysis was

performed using GenePix Pro 7 software (Molecular Devices Corporation; Sunnyvale, CA).

Background fluorescence was subtracted from the median spot fluorescence and values were averaged for each duplicate component spot. Additional details on array fabrication, processing, and analysis can be found in the protocol by Temme and Gildersleeve.[35] Full microarray data can be found in the Supporting Excel File.

3.4.6 Animal study ethics statement

All animal care procedures and experimental protocols have been approved by the Institutional Animal Care and Use Committee of Michigan State University (**protocol number:** 202200444).

3.4.7 Immunization protocol

Vaccination constructs were prepared by mixing the conjugates in sterile PBS and MPLA. The dosing of the constructs was determined by average antigen loading on the carrier to allow 8 nmol glycan dose for each mouse. In a typical protocol, 100 µg mQβ-PNAG0 in 180 µl PBS was mixed with 20 µg MPLA in 20 µl DMSO to produce one dose of the vaccine.

Pathogen-free C57BL/6 or CD1 female mice aged 6 weeks were obtained from the Charles River and maintained in the University Laboratory Animal Resources facility of Michigan State University. Groups of five mice were injected subcutaneously under the scruff with the MPLA adjuvanted vaccine constructs. Immunization procedures were performed on day 0, 14 and 28. Blood samples were collected *via* the hind limb vein on days 0, 7, 21 and 35.

Rabbit immunization was performed by ProSci. Each dose of the construct contains an equivalent glycan amount of 8 nmol. The prime vaccination was adjuvanted with the Complete

Freund's Adjuvant (CFA) and the booster doses were adjuvanted with the incomplete Freund's Adjuvant (IFA). For each dose, 100 µl vaccine conjugate solution was mixed with 100 µl CFA or IFA and votexed vigorously to form a homogeneous emulsion. The immunization procedures were performed on day 0, 14, 28 and 42. Blood samples were collected on days 0, 7, 21 and 35. The terminal bleeding was performed on day 56.

3.4.8 ELISA

Immulon 4 HBX 384 well plates (ThermoFisher 8755) were coated with 0.5 µg BSA-PNAG conjugates in 50 µl PBS at 4 °C overnight. The liquid was discarded, and the wells were blocked by 100 µl PBS containing 1% BSA for 1 h. The liquid was discarded, and the plates were washed by PBST for 4 times. Mouse or rabbit immune sera were serial diluted in PBS containing 0.1% BSA. 50 µl diluted serum was added to each well and incubated for 2 h. The liquid was discarded, and the plates were washed with PBST for 4 times. 1: 2,000 HRP-goat anti mouse IgG antibody (JacksonImmunoResearch 115-035-003) in 50 µl PBS containing 0.1% BSA was added and incubated for 1 h. For rabbit serum, the HRP-goat anti rabbit IgG antibody was used (JacksonImmunoResearch 111-005-003). The liquid was discarded, and the plates were washed with PBST for 4 times. 75 µl TMB substrate solution was added to each well and the reaction was allowed to proceed for 15 mins before 25 µl 0.5 M sulfuric acid was added. OD450 was immediately recorded and fitted into the 4PL nonlinear logistic model *via* GraphPad Prism 6 with least squares algorism. Maximum OD values reached ~3.0 for all groups. Unmodified BSA coated

wells showed negligible signal (<0.1 AU) and were subtracted as plate blank. EC50 titers were

calculated to present the dilution folds where binding signal is 50% of the maximum: the average

value (OD ~1.5) between the maximum and baseline was used as intercept to calculate EC50 titers.

All dilutions were run as triplicates. All steps were run under ambient temperature unless specified.

3.4.9 Molecular Docking

Docking was performed via AutoDock Vina 1.13 following the standard protocol provided by

the software developers. The receptor structure was adapted from published F598 crystal structure

(6be4). Water molecules and the ligand were removed from the protein. For simplicity, CH1 and

CL of the Fab were removed. 32 ligands were docked to the receptor individually. The top 10

results based on docking score were saved. The conformation with the best score for each ligand

was used for analysis. The docking for each ligand was repeated 10 times and similar results was

observed for each attempt.

3.4.10 Serologic assays

ELISA was used to determine antibody titers against PNAG producing bacterial cells. *S.

aureus* ATCC29213 were grown in LB medium to OD of 0.7, washed and resuspended in PBS to

a final OD of 0.5. 0.1 ml bacterial cells were added to each well of a 4 HBX 384-well plate. The

plate was placed in 4 °C overnight to allow the cells to attach. The cells were then fixed in ice cold

methanol for 2 mins. Methanol was removed and the wells were washed with Milli-Q water once

and then PBST for 4 times. The wells were then blocked by 100 µl PBS containing 1% BSA for 1

h. Rabbit immune sera were serial diluted in PBS containing 0.1% BSA. 50 µl diluted serum was added to each well and incubated for 2 h. The liquid was discarded, and the plates were washed with PBST for 4 times. 1: 2,000 HRP-goat anti rabbit IgG antibody (JacksonImmunoResearch 111-005-003) in 50 µl PBS containing 0.1% BSA was added and incubated for 1 h. The liquid was discarded, and the plates were washed with PBST for 4 times. 75 µl TMB substrate solution was added to each well and the reaction was allowed to proceed for 15 mins before 25 µl 0.5 M sulfuric acid was added. OD450 was immediately recorded and fitted into the 4PL nonlinear logistic model *via* GraphPad Prism 6 with least squares algorism. Maximum OD values reached ~3.0 for all groups. Unmodified BSA coated wells showed negligible signal (<0.1 AU) and were subtracted as plate blank. EC50 titers were calculated to present the dilution folds where binding signal is 50% of the maximum: the average value (OD ~1.5) between the maximum and baseline was used as intercept to calculate EC50 titers. All dilutions were run as triplicates. All steps were run under ambient temperature unless specified.

ELISA to determine antibody titers to PNAG and analysis of the deposition of complement component C1q were performed as described[25] except that mouse or rabbit antisera were used in place of equine serum and secondary antibodies used for PNAG titer determinations used secondary antibodies specific to either mouse or rabbit IgG. Titers were calculated using simple linear regression wherein the dilution curve crossed the X axis at an OD value equal to approximately 3X the standard deviation of the mean upper OD limits in control, negative sera.

3.4.11 Reagents

Antisera to the conjugate of 5GlcNH$_2$ to TT (5GlcNH$_2$-TT) were prepared in rabbits as previously described.[6, 12]   Native PNAG was purified from *A. baumannii* as described.[23]

3.4.12 OPK killing assay

OPK killing assay was adapted from previously published work.[36] HL-60 (ATCC) cells were maintained in RPMI-1640 with L-glutamine and 10% FBS (growth medium), under at 37 °C and 5% CO$_2$ in sterile filter-capped 75 cm^2 flasks. Upon use, the cells were induced to differentiate with 0.6% (V/V) DMF added to growth medium. The induction was performed for 5 days. Bacterial strain *S. aureus* ATCC 29213 was grown in LB medium to an OD of 0.7. Aliquots of the bacteria stock were kept in -80 °C in 1:1 (V:V) glycerol and LB. Bacterial titers were determined by serial dilution and overnight growth on TSB agar plate under 37 °C. The numbers of colonies were used to calculate cell density in the stock. Heat treated (56 °C, 30 min) immune sera were serial diluted in growth medium and mixed with bacterial cells suspended in the same medium in a 96-well plate. For each dilution, duplicated wells were used. Each well consists of 2000 cfu bacterial cells in 3 µl medium and 7 µl diluted immune serum. The mixture was incubated under 37 °C for 30 mins. Induced HL-60 cells were harvested and resuspended to a density of $1.25*10^7$ /ml in growth medium. To each well of bacteria-serum mixture was added 40 µl HL-60 cells and 10 µl baby rabbit complement (Cedarlane CL3442-R). The mixture was incubated under 37 °C with 5% CO$_2$ for 1 hour, when 100 µl growth medium was added to each well. 10 µl of the mixture

was spread on TSB agar plates and the remaining live bacteria cells were counted by colonies formed after overnight incubation. HL-60 omitted groups, complement deactivated groups (56 °C, 30 min), pre-immune serum groups and free bacteria groups were each performed as controls. Free bacteria groups were used as standard for 0% killing. Bacterial omitted group was used as standard for 100% killing. The killing% of experimental groups were plotted against final serum dilution and fitted to 4PX non-linear logistic model with least squares algorism (GraphPad Prism 6). The dilution that gave 50% killing for each serum was calculated and used as EC50 titer.

3.4.13 Immunofluorescent staining

S. aureus strain ATCC29213 or hospital isolated MRSA strains were cultured in LB medium to an OD of 0.7. Cells were then spread to a glass slide. The slides were air dried and fixed in ice-cold methanol for 2 mins. The methanol was allowed to air dry, and the slides were washed in PBST for 3 times. *S. aureus* endogenous antibody binding proteins such as protein G were then blocked with 20 µg/ml recombinant human Fc (Invitrogen A42561) in PBS with 1% BSA for 1 hour under ambient temperature in a moisturized environment. The blocking solution was discarded, and the immune serum diluted in PBS with 1% BSA (1: 1600) was added to the cells. The slides were kept under ambient temperature for 1 hour in a moisturized environment and washed with PBST 3 times. Alexa Fluor 594 labeled goat anti rabbit IgG Fc 2nd antibody (ThermoFisher A11012) was diluted to a concentration of 5 µg/ml and added to the cells. The staining was performed overnight under 4 °C in a dark and moisturized environment. The slides

were then washed in PBST 3 times and sealed with curing anti-fade mountant for 24 hours under ambient temperature. The slides were visualized under a Nikon A1 CLSM.

3.4.14 Mouse challenge study protocol

For active immunization and challenge studies, female CD-1 mice aged 5-6 weeks were grouped (n=20) allowing a similar body weight average and distribution across the groups. Mice were immunized by TT-PNAG0 or mQβ-PNAG0 constructs each containing 8 nmol of oligosaccharides, adjuvanted with 20 μg MPLA. 21 and 42 days post priming, mice were boosted with the same constructs. Another group of mice received PBS as control. 56 days post priming, $2*10^8$ cfu *S. aureus* ATCC29213 cells in 200 μl PBS were intravenously administrated for each mouse. Mouse condition was monitored 3 times a day for the following 2 weeks. Mice losing more than 20% body weight or becoming moribund were euthanized. The kidneys were collected, homogenized and bacteria loading were determined *via* serial dilution and growing on TSB agar plates. On 14 days post challenge, all surviving mice were euthanized, and kidney bacteria levels were determined.

For passive immunization and challenge studies, female CD-1 mice aged 12-13 weeks were grouped (n=10) allowing a similar body weight average and distribution across the groups. Pooled (n=2) rabbit sera collected on 56 days post priming from mQβ-PNAG 0, 10 or 26 groups were heat inactivated (56 °C, 30 min) and diluted 1:800 folds. Mice were intraperitoneally administered with 200 μl diluted sera and challenged with $2*10^8$ cfu *S. aureus* ATCC29213 cells in 200 μl PBS via

the tail vein. Survival and disease burden of the challenged mice were monitored following the same protocol as described for active immunization and challenge studies.

3.4.15 DNA extraction for microbiome analysis

For the microbiome sequencing experiments, pathogen-free CD-1 female mice were obtained from the Charles River and housed in the University Laboratory Animal Resources facility of Michigan State University. The study was approved by the Institutional Animal Care and Use Committee (IACUC) of Michigan State University (protocol number: 202200444). Eight-week-old mice were injected subcutaneously under the stuff. The treatment group was injected with 0.1 ml MPLA adjuvanted vaccine constructs on days 0, 14 and 28. The control treatment was injected with 0.1 ml of 0.01M DPBS instead. Stools were collected from vaccine-, and control- treated animals at pre and 42-day post-vaccination. DNA was extracted from feces using the QIAamp® PowerFaecal® Pro DNA kit (QIAgen®). The quality and purity of the isolated genomic DNA were confirmed by gel electrophoresis and quantitated with a Qubit2.0 fluorometer using the Qubit® dsDNA HS Assay Kits (Thermo Fisher Scientific). The DNA samples were stored at -20°C.

3.4.16 PCR amplification procedure

Amplification of the16S rRNA gene (V3-V4) was performed using V3 (5′-(CCT TACGGGAGGCAGCAG-3′), V4 (5′-GGA CTACHV GGG TWTCTAAT-3′) primers (W: A or T; V: G or C or A; H: A or C or T). The PCR mixture for every reaction tube was composed of 12.5 µl DreamTaq™ Hot Start PCR Master Mix (Thermo Fisher Scientific) at a 2x concentration,

along with 11.5 µl nuclease-free water and 0.5 µl of each primer (V3 Forward primer and V4 Reverse primer). 1 µl (10 ng/µl) template DNA was added to the 25 µl mastermix. Thermocycling conditions included an initial denaturation step (3 minutes at 94°C), followed by 30 cycles of denaturation (30 seconds at 94°C), annealing (30 seconds at 56°C), extension (5 min at 72°C), and a final extension step of 1 minutes at 72°C. PCR products were separated using gel electrophoresis on 1.5% agarose gel.

3.4.17 Library preparation and sequencing.

The V3-V4 region of the 16S rRNA gene was amplified using indexed primers (341f/806r) suitable for the Illumina platform (Caporaso 2011). Libraries were normalized using Invitrogen SequalPrep DNA normalization plates and pooled products were cleaned and concentrated with Amicon DNA Concentrator and quantified with Qubit dsDNA HS, Agilent 4200 TapeStation HS DNA1000 and Kapa Illumina Library Quantification qPCR assays. The pooled libraries were run on a MiSeq platform using Illumina MiSeq v2 500 cycle chemistry in a standard V2 flow cell. Base calling was performed by Illumina Real Time Analysis (v1.18.54).

3.4.18 Bioinformatics and statistics.

The output MiSeq FastQ files were taken directly into Mothur v1.44.1[37] for phylogenetic analysis using the Silva database (V.132) for alignment and Training Set 18 from the Ribosomal Database Project for taxonomic identification. The command sequence of The Mothur MiSeq SOP (https://mothur.org/wiki/miseq_sop/) was used for the analysis with the exception that all samples

were subsampled down to 30,000 sequences before the alignment step. As recommended in the MiSeq SOP, we allowed 1 base difference per 100 bp in the pre.cluster command. In addition, prior to the final analytical steps in Mothur, all samples were rarefied to 21,900 sequences. Both OTU (97%) and ASV datasets were generated in Mothur. The statistical analyses were conducted in PAST 4.0 (Paleontological Statistics Software Package) and based on 5,507 OTUs after the removal of all singletons. A Bray-Curtis dissimilarity matrix was used to compute an NMDS plot displaying the community-level differences amongst samples as well as computing pairwise comparisons using ANOSIM and PERMANOVER, all as implemented in PAST. To identify populations that contributed to community differences, SIMPER as implemented in PAST and LefSe through the Huttenhower LefSe website (https://huttenhower.sph.harvard.edu/lefse) were used.

The sequencing data has been submitted to Genbank/SRA (Bioproject ID PRJNA997319).

REFERENCES

1. 2019 AR Threats Report. https://www.cdc.gov/drugresistance/biggest-threats.html (accessed May 22nd, 2023).

2. Uddin, T. M.; Chakraborty, A. J.; Khusro, A.; Zidan, B. R. M.; Mitra, S.; Emran, T. B.; Dhama, K.; Ripon, M. K. H.; Gajdacs, M.; Sahibzada, M. U. K.; Hossain, M. J.; Koirala, N., Antibiotic resistance in microbes: History, mechanisms, therapeutic strategies and future prospects. *J Infect Public Health* **2021,** *14* (12), 1750-1766.

3. Micoli, F.; Bagnoli, F.; Rappuoli, R.; Serruto, D., The role of vaccines in combatting antimicrobial resistance. *Nat Rev Microbiol* **2021,** *19* (5), 287-302.

4. Moellering, R. C., Jr., MRSA: the first half century. *J Antimicrob Chemother* **2012,** *67* (1), 4-11.

5. Maira-Litran, T.; Kropec, A.; Abeygunawardana, C.; Joyce, J.; Mark, G., 3rd; Goldmann, D. A.; Pier, G. B., Immunochemical properties of the staphylococcal poly-N-acetylglucosamine surface polysaccharide. *Infect Immun* **2002,** *70* (8), 4433-4440.

6. Cywes-Bentley, C.; Skurnik, D.; Zaidi, T.; Roux, D.; Deoliveira, R. B.; Garrett, W. S.; Lu, X.; O'Malley, J.; Kinzel, K.; Zaidi, T.; Rey, A.; Perrin, C.; Fichorova, R. N.; Kayatani, A. K.; Maira-Litran, T.; Gening, M. L.; Tsvetkov, Y. E.; Nifantiev, N. E.; Bakaletz, L. O.; Pelton, S. I.; Golenbock, D. T.; Pier, G. B., Antibody to a conserved antigenic target is protective against diverse prokaryotic and eukaryotic pathogens. *Proc Natl Acad Sci U S A* **2013,** *110* (24), 2209-2218.

7. Nicholson, T. L.; Brockmeier, S. L.; Sukumar, N.; Paharik, A. E.; Lister, J. L.; Horswill, A. R.; Kehrli, M. E., Jr.; Loving, C. L.; Shore, S. M.; Deora, R., The Bordetella Bps Polysaccharide Is Required for Biofilm Formation and Enhances Survival in the Lower Respiratory Tract of Swine. *Infect Immun* **2017,** *85* (8), e00261-17. DOI: 10.1128/IAI.00261-17.

8. Low, K. E.; Howell, P. L., Gram-negative synthase-dependent exopolysaccharide biosynthetic machines. *Curr Opin Struct Biol* **2018,** *53*, 32-44.

9. Joyce, J. G.; Abeygunawardana, C.; Xu, Q.; Cook, J. C.; Hepler, R.; Przysiecki, C. T.; Grimm, K. M.; Roper, K.; Ip, C. C.; Cope, L.; Montgomery, D.; Chang, M.; Campie, S.; Brown, M.; McNeely, T. B.; Zorman, J.; Maira-Litran, T.; Pier, G. B.; Keller, P. M.; Jansen, K. U.; Mark, G. E., Isolation, structural characterization, and

immunological evaluation of a high-molecular-weight exopolysaccharide from *Staphylococcus aureus*. *Carbohydr Res* **2003,** *338* (9), 903-922.

10. Skurnik, D.;   Cywes-Bentley, C.; Pier, G. B., The exceptionally broad-based potential of active and passive vaccination targeting the conserved microbial surface polysaccharide PNAG. *Expert Rev Vaccines* **2016,** *15* (8), 1041-1053.

11. Maira-Litran, T.;   Kropec, A.;   Goldmann, D. A.; Pier, G. B., Comparative opsonic and protective activities of *Staphylococcus aureus* conjugate vaccines containing native or deacetylated Staphylococcal Poly-N-acetyl-beta-(1-6)-glucosamine. *Infect Immun* **2005,** *73* (10), 6752-6762.

12. Gening, M. L.;   Maira-Litran, T.;   Kropec, A.;   Skurnik, D.;   Grout, M.;   Tsvetkov, Y. E.;   Nifantiev, N. E.; Pier, G. B., Synthetic beta-(1->6)-linked N-acetylated and nonacetylated oligoglucosamines used to produce conjugate vaccines for bacterial pathogens. *Infect Immun* **2010,** *78* (2), 764-772.

13. Lu, X.;   Skurnik, D.;   Pozzi, C.;   Roux, D.;   Cywes-Bentley, C.;   Ritchie, J. M.;   Munera, D.;   Gening, M. L.;   Tsvetkov, Y. E.;   Nifantiev, N. E.;   Waldor, M. K.; Pier, G. B., A Poly-N-acetylglucosamine-Shiga toxin broad-spectrum conjugate vaccine for Shiga toxin-producing Escherichia coli. *mBio* **2014,** *5* (2), e00974-14. DOI: 10.1128/mBio.00974-14.

14. Gening, M. L.;   Pier, G. B.; Nifantiev, N. E., Broadly protective semi-synthetic glycoconjugate vaccine against pathogens capable of producing poly-beta-(1-->6)-N-acetyl-d-glucosamine exopolysaccharide. *Drug Discov Today Technol* **2020,** *35-36*, 13-21.

15. Goldsby, R. A.;   Kindt, T. J.; Osborne, B. A., Kuby Immunology. In *Kuby immunology*, Freeman: New York, 2000; 275-285.

16. Coutinho, A.;   Moller, G.; Richter, W., Molecular basis of B-cell activation. I. Mitogenicity of native and substituted dextrans. *Scand J Immunol* **1974,** *3* (3), 321-328.

17. Sungsuwan, S.;   Wu, X.;   Shaw, V.;   Kavunja, H.;   McFall-Boegeman, H.;   Rashidijahanabad, Z.;   Tan, Z.;   Lang, S.;   Tahmasebi Nick, S.;   Lin, P. H.;   Yin, Z.;   Ramadan, S.;   Jin, X.; Huang, X., Structure Guided Design of Bacteriophage Qbeta Mutants as Next Generation Carriers for Conjugate Vaccines. *ACS Chem Biol* **2022,** *17* (11), 3047-3058.

18. Wu, X.;   Ye, J.;   DeLaitsch, A. T.;   Rashidijahanabad, Z.;   Lang, S.;   Kakeshpour, T.;   Zhao, Y.;   Ramadan, S.;   Saavedra, P. V.;   Yuzbasiyan-Gurkan, V.;   Kavunja, H.;   Cao, H.;

Gildersleeve, J. C.; Huang, X., Chemoenzymatic Synthesis of 9NHAc-GD2 Antigen to Overcome the Hydrolytic Instability of O-Acetylated-GD2 for Anticancer Conjugate Vaccine Development. *Angew Chem Int Ed Engl* **2021,** *60* (45), 24179-24188.

19. Wang, P.; Huo, C. x.; Lang, S.; Caution, K.; Nick, S. T.; Dubey, P.; Deora, R.; Huang, X., Chemical Synthesis and Immunological Evaluation of a Pentasaccharide Bearing Multiple Rare Sugars as a Potential Anti-pertussis Vaccine. *Angew. Chem. Int. Ed.* **2020,** *59* (16), 6451-6458.

20. Yin, Z.; Comellas-Aragones, M.; Chowdhury, S.; Bentley, P.; Kaczanowska, K.; Benmohamed, L.; Gildersleeve, J. C.; Finn, M. G.; Huang, X., Boosting immunity to small tumor-associated carbohydrates with bacteriophage qbeta capsids. *ACS Chem Biol* **2013,** *8* (6), 1253-1262.

21. Yin, Z.; Wu, X.; Kaczanowska, K.; Sungsuwan, S.; Comellas Aragones, M.; Pett, C.; Yu, J.; Baniel, C.; Westerlind, U.; Finn, M. G.; Huang, X., Antitumor Humoral and T Cell Responses by Mucin-1 Conjugates of Bacteriophage Qbeta in Wild-type Mice. *ACS Chem Biol* **2018,** *13* (6), 1668-1676.

22. Bachmann, M. F.; Rohrer, U. H.; Kundig, T. M.; Burki, K.; Hengartner, H.; Zinkernagel, R. M., The influence of antigen organization on B cell responsiveness. *Science* **1993,** *262* (5138), 1448-1451.

23. Bentancor, L. V.; O'Malley, J. M.; Bozkurt-Guzel, C.; Pier, G. B.; Maira-Litran, T., Poly-N-acetyl-beta-(1-6)-glucosamine is a target for protective immunity against *Acinetobacter baumannii* infections. *Infect Immun* **2012,** *80* (2), 651-656.

24. Choi, A. H.; Slamti, L.; Avci, F. Y.; Pier, G. B.; Maira-Litran, T., The pgaABCD locus of Acinetobacter baumannii encodes the production of poly-beta-1-6-N-acetylglucosamine, which is critical for biofilm formation. *J Bacteriol* **2009,** *191* (19), 5953-5963.

25. Cywes-Bentley, C.; Rocha, J. N.; Bordin, A. I.; Vinacur, M.; Rehman, S.; Zaidi, T. S.; Meyer, M.; Anthony, S.; Lambert, M.; Vlock, D. R.; Giguere, S.; Cohen, N. D.; Pier, G. B., Antibody to Poly-N-acetyl glucosamine provides protection against intracellular pathogens: Mechanism of action and validation in horse foals challenged with Rhodococcus equi. *PLoS Pathog* **2018,** *14* (7), e1007160. DOI: 10.1371/journal.ppat.1007160.

26. Kelly-Quintos, C.; Cavacini, L. A.; Posner, M. R.; Goldmann, D.; Pier, G. B., Characterization of the opsonic and protective activity against *Staphylococcus aureus* of fully

human monoclonal antibodies specific for the bacterial surface polysaccharide poly-*N*-acetylglucosamine. *Infect Immun* **2006,** *74* (5), 2742-2750.

27. Turner, N. A.;   Sharma-Kuinkel, B. K.;   Maskarinec, S. A.;   Eichenberger, E. M.;   Shah, P. P.;   Carugati, M.;   Holland, T. L.; Fowler, V. G., Jr., Methicillin-resistant Staphylococcus aureus: an overview of basic and clinical research. *Nat Rev Microbiol* **2019,** *17* (4), 203-218.

28. Fey, P. D.;   Endres, J. L.;   Yajjala, V. K.;   Widhelm, T. J.;   Boissy, R. J.;   Bose, J. L.;   Bayles, K. W., A genetic resource for rapid and comprehensive phenotype screening of nonessential Staphylococcus aureus genes. *mBio* **2013,** *4* (1), e00537-12. DOI: 10.1128/mBio.00537-12.

29. Lensmire, J. M.;   Wischer, M. R.;   Kraemer-Zimpel, C.;   Kies, P. J.;   Sosinski, L.;   Ensink, E.;   Dodson, J. P.;   Shook, J. C.;   Delekta, P. C.;   Cooper, C. C.;   Havlichek, D. H., Jr.;   Mulks, M. H.;   Lunt, S. Y.;   Ravi, J.; Hammer, N. D., The glutathione import system satisfies the Staphylococcus aureus nutrient sulfur requirement and promotes interspecies competition. *PLoS Genet* **2023,** *19* (7), e1010834. DOI: 10.1371/journal.pgen.1010834.

30. Hulsdunker, J.;   Thomas, O. S.;   Haring, E.;   Unger, S.;   Gonzalo Nunez, N.;   Tugues, S.;   Gao, Z.;   Duquesne, S.;   Cywes-Bentley, C.;   Oyardi, O.;   Kirschnek, S.;   Schmitt-Graeff, A.;   Pabst, O.;   Koenecke, C.;   Duyster, J.;   Apostolova, P.;   Blaser, M. J.;   Becher, B.;   Pier, G. B.;   Hacker, G.; Zeiser, R., Immunization against poly-*N*-acetylglucosamine reduces neutrophil activation and GVHD while sparing microbial diversity. *Proc Natl Acad Sci U S A* **2019,** *116* (41), 20700-20706.

31. Cywes-Bentley, C.;   Vinacur, M.;   Roberts, C.;   Lee, F.;   Landy, H.;   Ramsdell, D.;   Burton, C.;   Fitzpatrick, C.;   Nelken, M.;   Vlock, D.; Pier, G. B. In *AV0328-A Synthetic oligosaccharide-tetanus toxoid conjugate targeting the broadly expressed microbial surface polysaccharide PNAG is safe and immunogenic in humans, eliciting high titers of functional antibody to multiple pathogens*, ASM Microbe, Atlanta, GA, ASM Press: Atlanta, GA, 2018.

32. Vlock, D.;   Lee, J. C.;   Kropec-Huebner, A.; Pier, G. B. In *Pre-clinical and initial phase i evaluations of a fully human monoclonal antibody directed against the PNAG surface polysaccharide on Staphylococcus aureus*, Abstracts of the 50th ICAAC 2010; Abstract G1-1654/329., 2010.

33. Xia, L.; Gildersleeve, J. C., The Glycan Array Platform as a Tool to Identify Carbohydrate Antigens. *Methods Mol Biol* **2015,** *1331*, 27-40.

34. Campbell, C. T.;   Zhang, Y.; Gildersleeve, J. C., Construction and use of glycan microarrays. *Curr Protoc Chem Biol* **2010,** *2* (1), 37-53.

35. Temme, J. S.;   Crainic, J. A.;   Walker, L. M.;   Yang, W.;   Tan, Z.;   Huang, X.; Gildersleeve, J. C., Microarray-guided evaluation of the frequency, B-cell origins, and selectivity of human glycan-binding antibodies reveals new insights and novel antibodies. *J Biol Chem* **2022,** *298* (10), 102468.

36. Paschall, A. V.;   Middleton, D. R.; Avci, F. Y., Opsonophagocytic Killing Assay to Assess Immunological Responses Against Bacterial Pathogens. *J Vis Exp* **2019,** *Apr 5* (146), 59400. DOI: 10.3791/59400.

37. Schloss, P. D.;   Westcott, S. L.;   Ryabin, T.;   Hall, J. R.;   Hartmann, M.;   Hollister, E. B.;   Lesniewski, R. A.;   Oakley, B. B.;   Parks, D. H.;   Robinson, C. J.;   Sahl, J. W.;   Stres, B.;   Thallinger, G. G.;   Van Horn, D. J.; Weber, C. F., Introducing mothur: open-source, platform-independent, community-supported software for describing and comparing microbial communities. *Appl Environ Microbiol* **2009,** *75* (23), 7537-7541.

APPENDIX

Synthesis of PNAG pentasaccharide library (performed by Dr. Weizhun Yang)

While several PNAG structures have been synthesized before,[1-5] a general method for the expeditious construction of a comprehensive PNAG pentasaccharide library is lacking. To accelerate the library synthesis, rather than starting from monosaccharide building blocks for each targeted pentasaccharide, we envisioned the overall efficiency can be significantly enhanced with a divergent strategy. In our synthetic design, the amine groups of strategically protected pentasaccharides are differentiated by orthogonal protective groups for selective deprotection and acetylation. After screening multiple synthetic intermediates, we developed two key linchpin pentasaccharide intermediates (**1** and **2**), which bear four protective groups, i.e., *tert*-butyloxycarbonyl (Boc), allyloxycarbonyl (Alloc), 2,2,2-trichloroethoxycarbonyl (Troc), and fluorenylmethoxycarbonyl (Fmoc), on glucosamine units A, B, C and D. The reducing end glucosamine unit E is *N*-acetylated (for compound **1**) or *N*-trifluoroacetylated (for compound **2**) (**Scheme 3.1**).
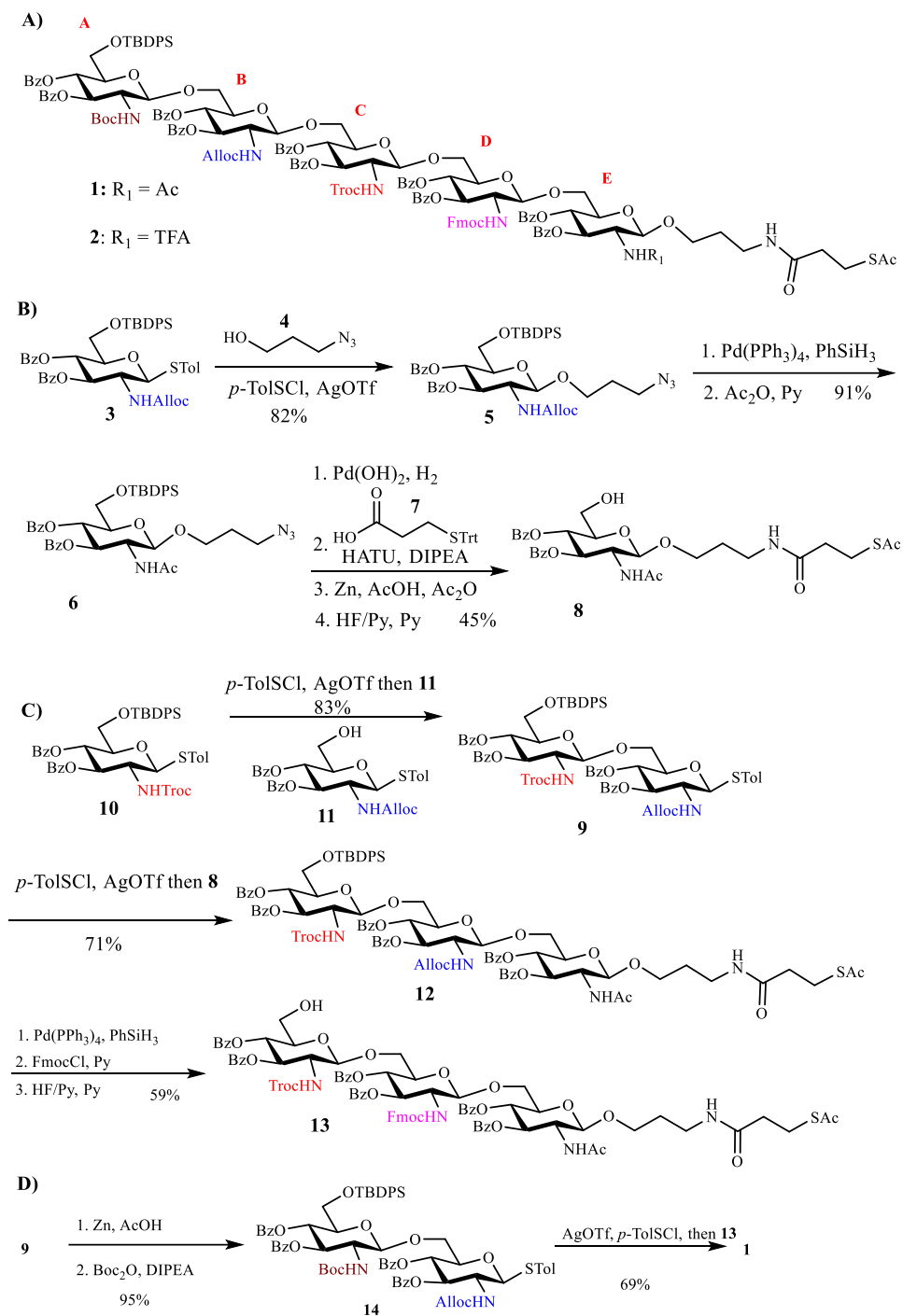
Scheme 3.1 Structures and syntheses of key intermediates. **a)** Structures of two key linchpin pentasaccharide intermediates (1 and 2). **b)** Synthesis of the reducing end glucosamine building block 8. **c)** Syntheses of compound 13; **d)** Syntheses of compound 1. Abbreviations: acetyl (Ac), allyloxycarbonyl (Alloc), benzoyl (Bz), tert-butyldiphenylsilyl (TBDPS), tert-butyloxycarbonyl (Boc), diisopropylethyl amine (DIPEA), fluorenylmethoxycarbonyl (Fmoc), hexafluorophosphate azabenzotriazole tetramethyl uronium (HATU), and 2,2,2-trichloroethoxycarbonyl (Troc).

Based on the above design, our synthesis commenced from thioglycoside **3**, which glycosylated 3-azido-1-propanol **4** to provide compound **5** in 82% yield (**Scheme 3.1b**). Upon removal of the Alloc group from **5** and *N*-acetylation, the resulting compound **6** was subjected to azide reduction, amidation of the free amine with carboxylic acid **7**, and protective group adjustments leading to compound **8** in 45% yield for the four steps.

Oligosaccharide assembly started from the CD disaccharide **9** containing *N*-Troc and *N*-Alloc groups (**Scheme 3.1c**). Thioglycoside donor **10** was preactivated with the *p*-TolSCl/AgOTf promoter system[6] at -78°C. Upon complete activation, the thioglycosyl acceptor **11** was added to the reaction mixture leading to disaccharide **9** in 83% yield (**Scheme 3.1c**). In order to extend the glycan chain, the glycosylation of acceptor **8** with disaccharide **9** was performed. When the reaction was first carried out under the pre-mix condition, i.e., **9** and **8** were mixed together followed by the addition of promoter (*p*-TolSCl/AgOTf or NIS/TfOH[7, 8]), little desired trisaccharide **12** was obtained, which was likely due to the activation of the thioester (SAc) moiety by the thiophilic promoter. Next, the reaction was explored under the pre-activation condition by activating **9** with the promoter *p*-TolSCl/AgOTf first, followed by the subsequent addition of acceptor **8**. This change of the reaction protocol successfully produced trisaccharide **12** in 71% yield. Replacement of Alloc with Fmoc and removal of TBDPS group from **12** resulted in the trisaccharide **13**. To extend **13** to a pentasaccharide, the Troc moiety of disaccharide **9** was replaced with Boc (disaccharide **14**, Figure 2D). Pre-activation based glycosylation of **14** and **13** produced

pentasaccharide **1**, which contains four different *N*-protective groups on units A, B, C and D. Analogously, pentasaccharide **2** was synthesized with four different *N*-protective groups on units A, B, C and D, and the *N*-TFA group on unit E (**Figure 3.16**).

With the two key pentasaccharides in hand, we explored orthogonal deprotection of pentasaccharides **1** and **2**. As an example, the Boc and Alloc groups of compound **2** could be removed by 90% aqueous TFA and Pd(PPh$_3$)$_4$/PhSiH$_3$, while deprotections of Troc and Fmoc were accomplished using Zn/AcOH and 20% piperidine in DMF respectively without affecting any other amine protective groups (**Scheme 3.2**). These results suggest that the four amine protective groups could be independently removed specifically.
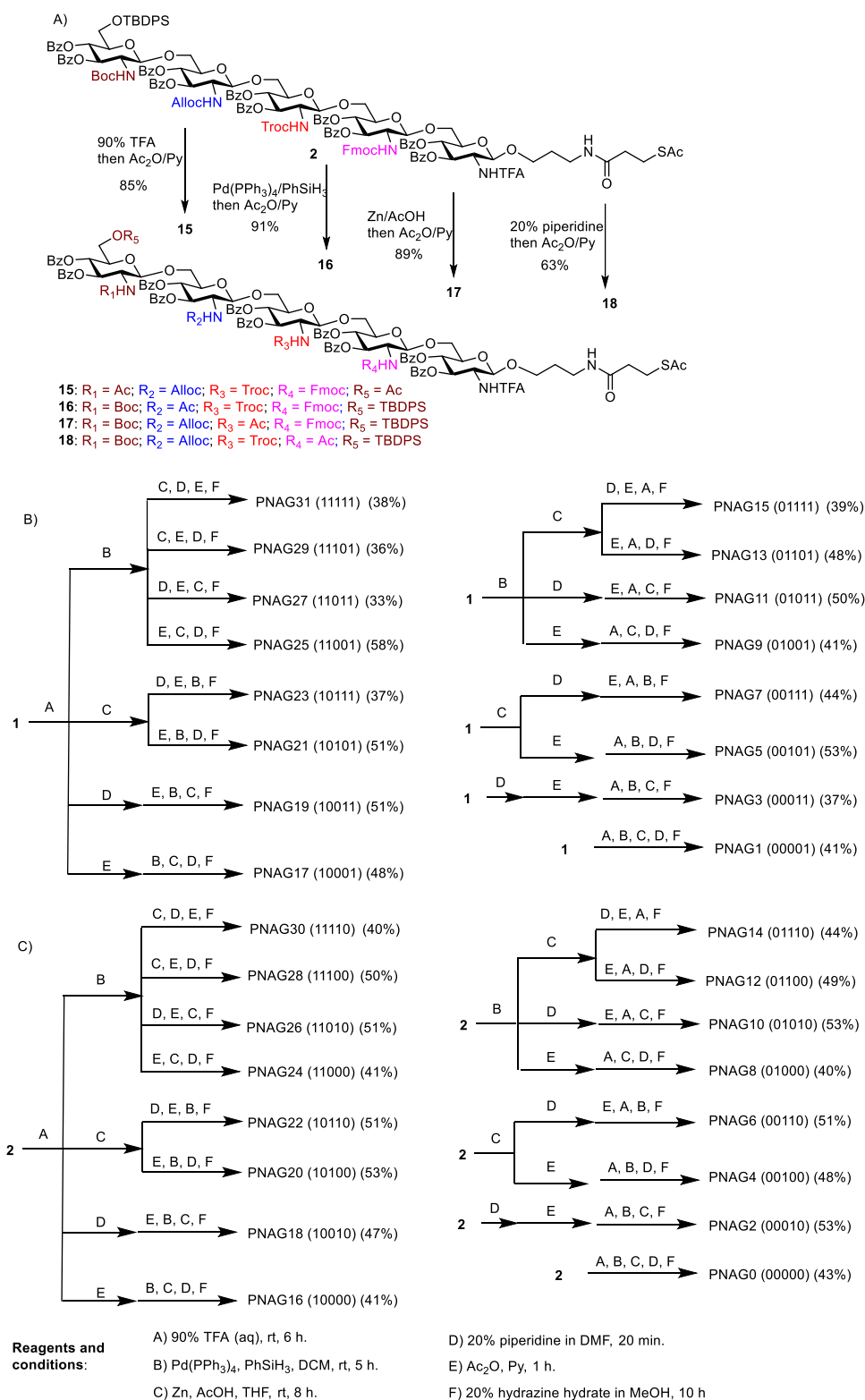
Scheme 3.2 Synthesis of the 32 membered comprehensive PNAG pentasaccharide library. **a)** Orthogonal deprotection of pentasaccharide **2**. **b)** Divergent syntheses of 16 PNAG

Scheme 3.2 (cont'd)
pentasaccharides from the strategically protected pentasaccharide **1**. **c)** Divergent syntheses of 16 PNAG pentasaccharides from the strategically protected pentasaccharide **2**. Abbreviations: acetyl (Ac), allyloxycarbonyl (Alloc), benzoyl (Bz), *tert*-butyldiphenylsilyl (TBDPS), *tert*-butyloxycarbonyl (Boc), diisopropylethyl amine (DIPEA), dimethylformamide (DMF), fluorenylmethoxycarbonyl (Fmoc), hexafluorophosphate azabenzotriazole tetramethyl uronium (HATU), 2,2,2-trichloroethoxycarbonyl (Troc), and trifluoroacetic acid (TFA).

With the orthogonal deprotection conditions established, divergent modifications of the key pentasaccharide intermediates were carried out. Treatment of pentasaccharide **1** with 90% TFA cleaved both Boc and TBDPS groups (**Scheme 3.2**). Upon acetylation of the newly liberated hydroxyl and amine moieties, the Alloc, Troc, and Fmoc groups were subsequently removed followed by full *O*- and *S*-deacylation with 20% hydrazine hydrate in MeOH, affording PNAG17 pentasaccharide in 48% overall yield bearing the *N*-acetylglucosamine (GlcNAc)-glucosamine (GlcN)-GlcN-GlcN-GlcNAc (10001) sequence. Alternatively, following TFA treatment of **1**, the Fmoc group was cleaved, which was then acetylated with subsequent removal of Troc, Alloc and Bz moieties to produce pentasaccharide PNAG19 with the GlcNAc-GlcN-GlcN-GlcNAc-GlcNAc sequence (10011) in 51% overall yield. Similar divergent modification processes on the two key pentasaccharides **1** and **2** produced the full library of thirty-two PNAG pentasaccharides with all possible combinations of free amines in each glucosamine unit of the pentasaccharides (**Scheme 3.2c**).

REFERENCES

1. Yang, F.; Du, Y., A practical synthesis of a (1-->6)-linked beta-D-glucosamine nonasaccharide. *Carbohydr Res* **2003,** *338* (6), 495-502.

2. Leung, C.; Chibba, A.; Gomez-Biagi, R. F.; Nitz, M., Efficient synthesis and protein conjugation of beta-(1-->6)-D-N-acetylglucosamine oligosaccharides from the polysaccharide intercellular adhesin. *Carbohydr Res* **2009,** *344* (5), 570-575.

3. Gening, M. L.; Tsvetkov, Y. E.; Pier, G. B.; Nifantiev, N. E., Synthesis of beta-(1-->6)-linked glucosamine oligosaccharides corresponding to fragments of the bacterial surface polysaccharide poly-N-acetylglucosamine. *Carbohydr Res* **2007,** *342* (3-4), 567-575.

4. Wang, S.; Breslawec, A. P.; Alvarez, E.; Tyrlik, M.; Li, C.; Poulin, M. B., Differential Recognition of Deacetylated PNAG Oligosaccharides by a Biofilm Degrading Glycosidase. *ACS Chem Biol* **2019,** *14* (9), 1998-2005.

5. Li, D.; Wang, J.; Wang, X.; Qiao, Z.; Wang, L.; Wang, P.; Song, N.; Li, M., beta-Glycosylations with 2-Deoxy-2-(2,4-dinitrobenzenesulfonyl)-amino-glucosyl/galactosyl Selenoglycosides: Assembly of Partially N-Acetylated beta-(1 --> 6)-Oligoglucosaminosides. *J Org Chem* **2023,** *88* (13), 9004-9025.

6. Huang, X.; Huang, L.; Wang, H.; Ye, X.-S., Iterative one-pot oligosaccharide synthesis. *Angew. Chem. Int. Ed.* **2004,** *43*, 5221-5224.

7. Konradsson, P.; Udodong, U. E.; Fraser-Reid, B., Iodonium promoted reactions of disarmed thioglycosides. *Tetrahedron Letters* **1990,** *31* (30), 4313-4316.

8. Veeneman, G. H.; van Leeuwen, S. H.; van Boom, J. H., Iodonium ion promoted reactions at the anomeric centre. II An efficient thioglycoside mediated approach toward the formation of 1,2-trans linked glycosides and glycosidic esters. *Tetrahedron Letters* **1990,** *31* (9), 1331-1334.